U-Pb zircon provenance of metamorphosed clastic sediments in a developing rift (Dom Feliciano Belt, Uruguay and Kaoko Belt, Namibia)

Master of Science thesis

Harald Nedrebø

Department of Earth Science
University of Bergen
November 2014

Acknowledgements

First of all I would very much like to thank my supervisors Jiri Konopásek and Jiri Sláma for excellent feedback, and the learning of zircon analysis during my time as a master student.
I especially want to thank Jiri Konopásek for sharing his expertise and detailed techniques regarding detrital zircon analysis, making the master project even more interesting. Jiri Sláma has been very supportive and helpful, especially regarding detrital zircon methodology and the application of zircon reference materials. I also very much would like to thank my first co-supervisor Jan Košler for excellent guidance for the LA-ICPMS analysis, and it is very sad that he passed away this spring.

A substantial amount of time during this thesis has been in different laboratories, and I would like to thank Tereza Konopásek and Irina Maria Dumitru for great guidance during the mineral separation and mount preparation procedures. I would also like to thank Egil Erichsen for excellent guidance with cathodoluminescence imaging and Siv Hjort Dundas for important assistance in the data processing part of the LA-ICPMS analysis. Nicola McLoughlin is being thanked for teaching me how to apply petrographic microscopy for my results part.

Also, I would like to thank my fellow geology student through the five excellent years at the University of Bergen, in particular Anders Bjerga, Anders Friestad, Hallgeir Sirevaag, Kristian Agasøster Haaga and Steinar Polden Sæverud for support and constructive feedback during these years.

Bergen, 9th of November 2014

Harald Nedrebø

Abstract

Geochronological studies of the westernmost part of the Kaoko Belt in Namibia, the Coastal Terrane, revealed zircons with distinct Neoproterozoic ages, that are no known from other parts of this orogen and an exotic origin was thus proposed for this tectonic unit. The same temporal evolution is known for the Punta del Este Terrane, the easternmost part of the Dom Feliciano Belt in Uruguay and these units are presently considered as one tectonic domain split by the Atlantic Ocean. In this study, dating of detrital zircons from metamorphosed clastic sedimentary rocks has been done to evaluate the relationship of the Coastal Terrane – Punta del Este to the neighboring cratonic domains. In addition, two metagranitoid rocks have been dated in order to better constrain the pre-metamorphic history of the studied unit.

Two quartzite samples from the metasedimentary sequence of the Punta del Este Terrane show dominance of Paleoproterozoic ages compatible with the Rio de la Plata Craton as a source region. Zircons in one of these samples also revealed ages of c. 610 Ma, which are interpreted as grains recrystallized during granulite-facies metamorphism. Two samples of metamorphosed granitoid rocks revealed magmatic events at c. 770-800 Ma and at c. 656 Ma.

Sample of quartzite from tectonically lowermost Coastal Terrane shows mostly Paleo- and Mesoproterozoic ages of detrital zircons indicating the Congo Craton as a source region. One sample of metasedimentary migmatitic gneisses collected from the tectonically upper part of the Coastal Terrane shows dominance of c. 760 Ma old detrital zircons, which suggests erosion and redeposition of rifting-related magmatic rocks. Two other samples have shown almost exclusively c. 650 Ma and c. 620 Ma old zircons. As these ages are known as the age of high-grade metamorphism in the Coastal Terrane, zircons of this age are interpreted as originating from dissolution and neocrystallization, or recrystallization of older detrital zircons.

The detrital zircon age groups in the studied samples are compatible with the ages known from the basement rocks of the neighboring cratonic domains. This suggests that the Coastal Terrane – Punta del Este is not an exotic unit, but probably originated in close proximity of the Congo and Rio de la Plata Cratons during Neoproterozoic rifting of the Rodinia supercontinent.

Contents

1 Introduction

The crustal fragmentation of Rodinia supercontinent started early in the Neoproterozoic Era, due to a development of episodic mantle plume between c. 825-750 Ma (Li et al., 2008).
In the area of the present day Southern Africa and Eastern South America, the result of the rifting was the formation of the passive margins of the Congo, Kalahari and Rio de la Plata cratons that subsequently amalgamated into western Gondwana through the formation of the Dom Feliciano, Kaoko, Gariep and Damara orogenic belts (see overview by Frimmel et al., 2010). However, these Neoproterozoic orogenic belts contain tectonic units that are still enigmatic in terms of their pre-collisional position and evolution.
The two key areas of this study are the Punta del Este Terrane in eastern Uruguay, which represents the southeastern part of the Neoproterozoic Dom Feliciano Belt (See Study area: Fig. 10), and the Coastal Terrane in northwestern Namibia representing the westernmost part of the Kaoko Belt (See Study area: Fig. 12). Due to the presence of magmatic rocks of the same age (c. 800–760 Ma) metamorphosed in both units at c. 650–630 Ma, these two tectonic units are interpreted as one Neoproterozoic crustal block that is now split due to opening of the Atlantic Ocean (Gross et al., 2009; Oyhantcabal et al., 2009a; Lenz et al., 2011).
The reported ages and isotopic signatures differ from other geological units of the Kaoko and Dom Feilicano Belt. Goscombe and Gray (2007) suggested that the Coastal Terrane is an arc/back-arc terrane with an independent tectonic evolution with respect to the Congo Craton passive margin. Konopásek et al. (2014a) proposed that the Coastal Terrane developed on the edge of the Congo Craton margin prior to their mutual collision. However, the nature and pre-orogenic position of these two tectonic units is still not well understood.

This work presents a study of detrital zircons from the metasedimentary samples collected in the Coastal and Punta del Este terranes with the aim to compare the age populations with the ages of magmatic and metamorphic rocks from the neighboring cratonic domains (the Congo and Rio de la Plata cratons, respectively). Such comparison should confirm or disprove the possibility that the exposed respective cratonic basement units have served as a source of detrital material for the sedimentation in the Coastal and Punta del Este terranes. This in turn might provide additional data for the distinction between the exotic and the in-situ nature of the studied units with respect to the neighboring cratonic domains.

1.1 Previous work

The first indication of rifting in the area of the Damara and Kaoko belts was a study by Martin (1965) describing rifting-related clastic sediments overlying the Congo Craton basement. This observation was later confirmed by e.g. Hedberg (1979) or Miller (1983). Hoffman et al. (1996) determined that the initial rifting along the southern margin of the Congo Craton occurred at c. 756-746 Ma by dating granitoids and rhyolitic lava flows intruding the basalt sedimentary sequence in the Damara Belt. Similar ages (c. 740-710 Ma) from metamorphosed volcanic rocks occurring within the Neoproterozoic cover of the Congo Craton in the Kaoko Belt have been reported recently by Konopásek et al. (2014a). A reconnaissance detrital zircon data from metasediments of the Coastal Terrane have recently been provided showing age peaks at 1.05 Ga and 1.75 Ga (Konopásek et al., 2014a). Goscombe & Gray (2008) have described the convergent evolution of the Kaoko Belt as a series of tectonic events causing magmatic arc/back arc development associated with migmatitization at 660-610 Ma in the Coastal Terrane unit, with a subsequent metamorphism due to transpressional orgoenesis at 585-560 Ma in more external parts of the orogen.
Kröner et al. (2004) have reported protolith ages at c. 730 Ma and c. 703 Ma from porphyritic meta-granitoids in the Coastal Terrane, while Konopásek et al. (2008) have reported metagranitoids with ages c. 800 Ma associated with amphibolites and interpreted them as metamorphosed synsedimentry volcanic rocks (See Study area: Fig. 12).
Recently, Lenz et al. (2011) have published a geochronological study of mafic to felsic granulites from the Punta del Este Terrane in the Dom Feliciano Belt. The studied zircon grains provided ages of 802-767 Ma for the magmatic protolith of the samples, and zircon overgrowths at c. 650 Ma indicating the high grade metamorphism. Similarly, Oyhantcabal et al. (2009a) dated protolith of a felsic meta-igneous rock from the Punta del Este Terrane at 770 Ma, and its high grade metamorphism at c. 650 Ma.

1.2 Research objective

The main research objective in this study is to investigate detrital zircon populations from metasediments of the Coastal and Punta del Este terranes, and to link their ages to protolith ages reported from the Congo and Rio de la Plata cratons.

2 Regional geology

2.1 The assembly and initial breakup of Rodinia at 1100-780 Ma

The formation of the core of Rodinia involved initial oblique collisions between Laurentia, North China, Siberia, South China and Rio de la Plata at c. 1100 Ma (Fig. 1a), although the continents still were separated by oceans (Greentree et al., 2006).

The Kalahari Craton joined Laurentia at c. 1050 (Fig 1b) and its movement was followed by transpressional displacement along the margins between the Australia-East Antarctica and India cratons (Fig. 1c), as indicated by metamorphic ages from the Pinjarra Belt at c. 1100-1000 Ma (Fitzsimons, 2003). Also, the evolution of the Rayner Province in East Antarctica is correlated with the Ghats Belt in India through the high grade metamorphic events at 990-900 Ma (Fig. 1d).
By c. 900 Ma the Indian and East Antarctica-Australia cratons were assembled in the Rodinia supercontinent through the development of the eastern Sibao Orogen in China starting at c. 920 Ma (Li et al., 2005).

The geochronological record from c. 900 to 830 Ma is poorly preserved, except the intrusions from South China and Africa at c. 870-850 Ma (Li et al. 2003b) and from the Caledonides (Paulsson and Andreasson, 2002; Fig. 1d.)
Felsic and mafic dykes and intrusions have been reported at c. 825 Ma (Fig. 1e) from Australia (Wingate et al., 1998), South China (Li et al., 1999), India (Radhakrishna and Mathew, 1996) and Kalahari craton (Frimmel et al., 2001). A superplume has been proposed at this stage by Ernst et al., (2008). D' Agrella et al. (2004) and Weil et al. (1998) proposed a spread in paleo-magnetic poles at c. 780 Ma (Fig. 1f).

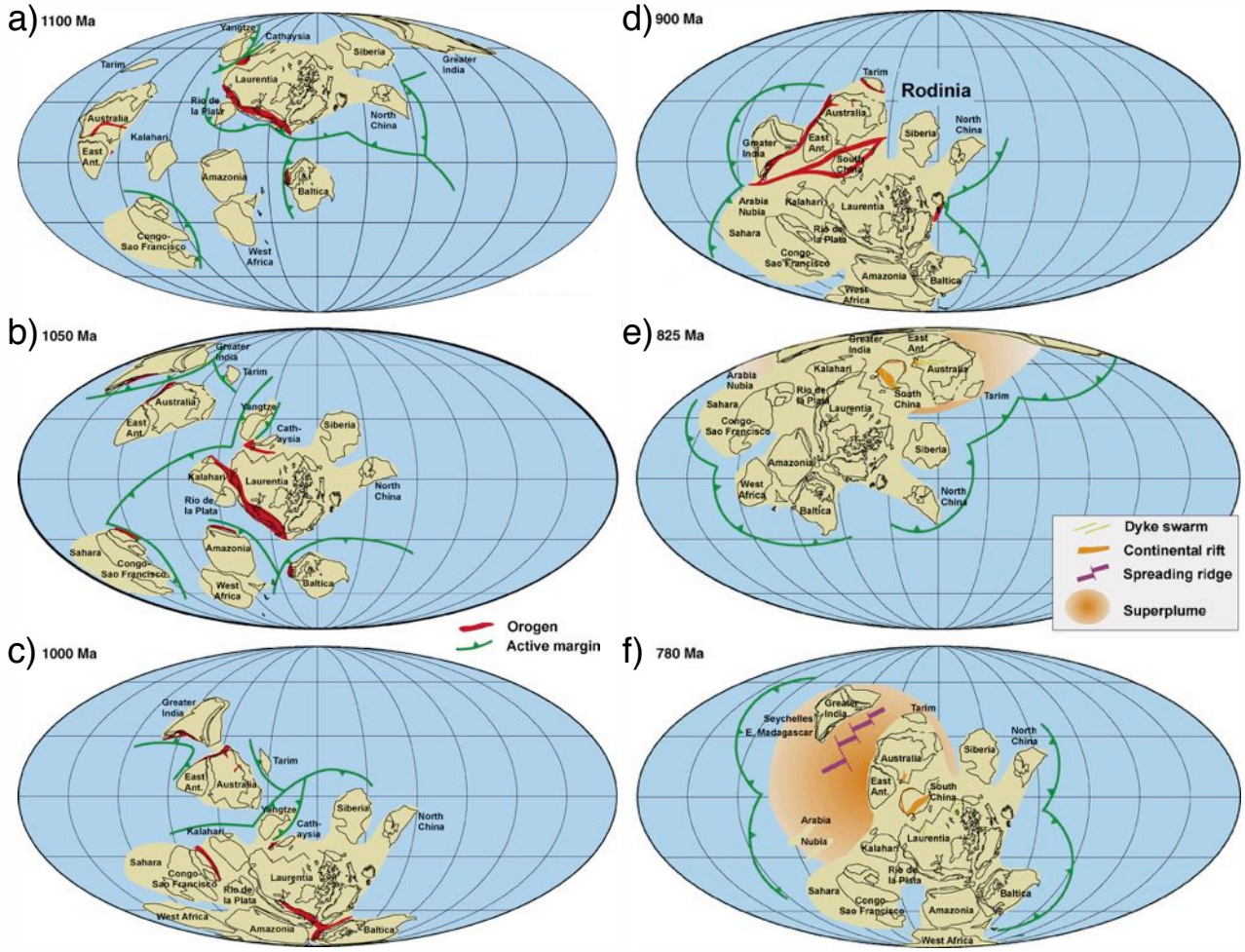

Fig 1: Reconstruction of the assembly and rifting of Rodinia with time slices at: a) 1100 Ma indicating the convergence of Yangtze, Rio de la Plata and Laurentia continent and the South Tasman Rise orogen. b) 1050 Ma for the collision between the Kalahari and Laurentia continents. c) At 1000 Ma all continents except Tarim, East-Antarctica-Australia and Greater India had assembled into Rodinia. d) Orogenesis at 900 Ma forms Ghats Belt in India and the Sibao Orogen in Southern China. e) The initial rifting stage of Rodinia due to the formation of a superplume at 825 Ma.
f) Continuation of rifting at 780 Ma. The compilation is based on the determination of paleomagnetic poles from cratons and orogens. After Li et al. (2008).

2.2 The fragmentation of Rodinia and the assembly of Gondwana at 750-500 Ma

The paleomagnetic data from Hoffman (1991) indicate that at c. 755 Ma the poles for the Laurentia and Congo-Sao Francisco cratons are widely spread (Fig. 2), which indicates disintegration of Rodinia at this time. The position of the Rio de la Plata terrane is placed in between Congo and Laurentia based on poles from D' Agrella et al. (2004) and Weil et al. (1998).

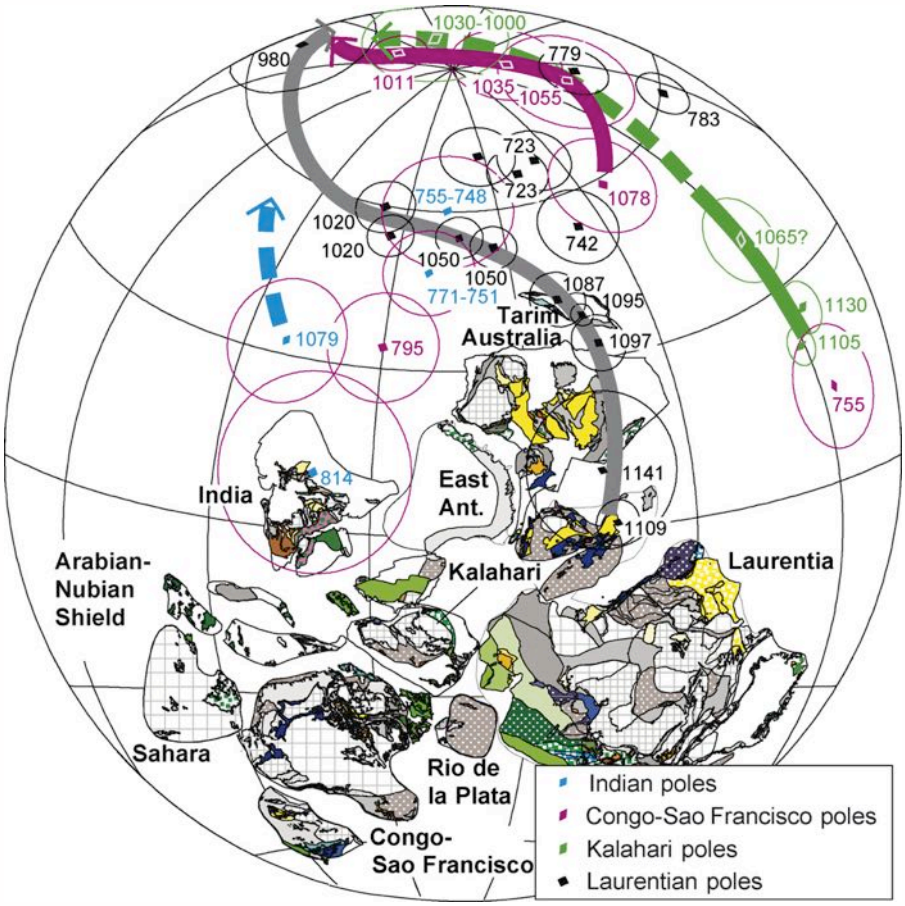

Fig. 2: Simplified map of Rodinia including the positions and the paleomagnetic poles of the Indian, Congo-Sao Francisco, Kalaharian and Laurentian cratons. After Li et al. (2008).

According to Su et al. (1994) and Aleinikoff et al. (1995), the rifting of the southern margins of Laurentia started at 750 Ma (Fig. 3a). The same ages have been reported by Meert et al. (1995) as indication of rifting of the Congo-Sao Francisco, Rio de la Plata and the Kalahari cratons from western Laurentia (Fig 3a). By 720 Ma Australia-East Antarctica, South China, Kalahari and Siberia started to break apart from Laurentia (Fig 3b). The collision between the Congo-Sao Francisco, Rio de la Plata, Amazonia and West Africa started around 630 Ma (Fig. 3c), and the orogenesis of the Kaoko, Damara, Gariep and Dom Feliciano belts at 600 Ma (Fig. 3d).

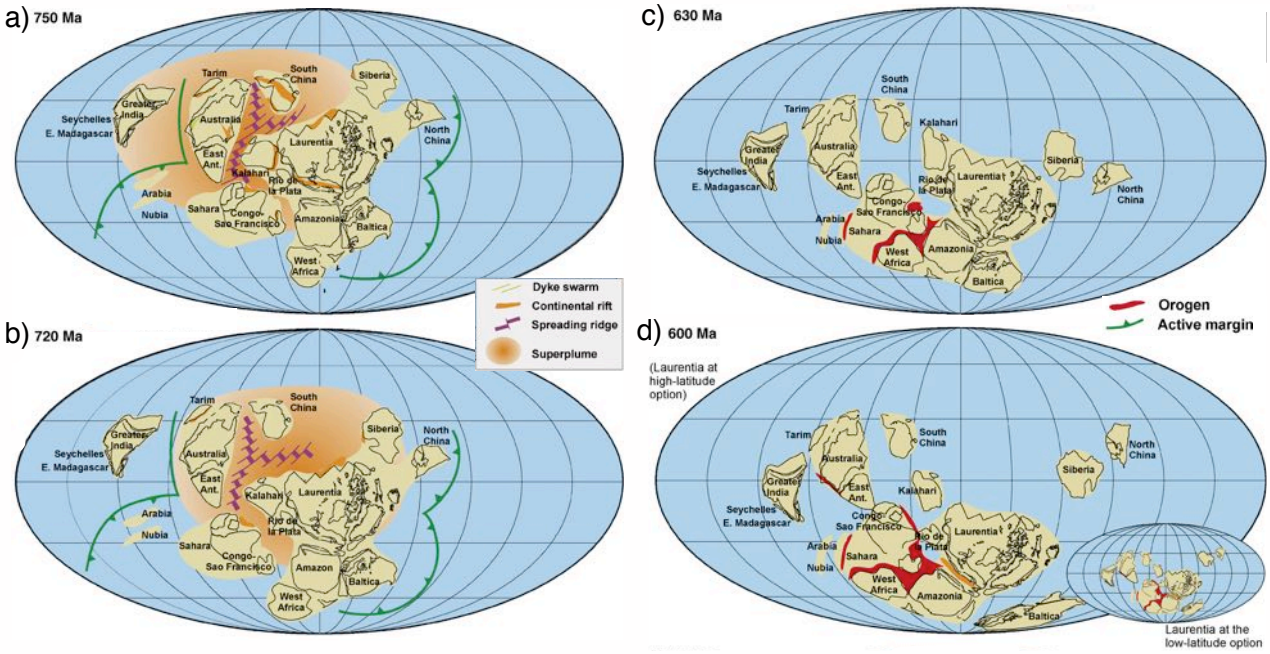

Fig 3: Global reconstruction of the dispersal of Rodinia, and the initial assembly of Gondwana with time slices at: a) 750 Ma indicating the initial rifting between the Congo-Sao Francisco, Kalahari, Eastern Antarctica, South China and Laurentia. b) At 720 Ma the rifting continues in the opening of the Adamastor Ocean. c) The initial assemblage of Gondwana at 630 Ma involving orogenesis due to the collisions of the Congo-Sao Francisco, Amazonia, West-Africa and Sahara. d) The development of the Damara, Graiep, Kaoko and Dom Feliciano Belt due to the collision of the Rio de la Plata and Congo-Sao Francisco Cratons at 600 Ma. The map is based on a compilation of paleomagnetic poles from cratons and orogens, after Li et al. (2008).

2.2.1 Rifting related volcanism in the Kalahari, Rio de la Plata and Congo cratons

Rifting related volcanism of the mid-Neoproterozic age along the margins of the Kalahari, Rio de la Plata and Congo cratons has been confirmed by authors studying syn-sedimentary volcanics and early plutonic rocks intruding the Neoproterozic sediments. Frimmel et al. (1996) reported rifting related volcanism from the western margin of the Kalahari Craton at c. 740 Ma, while the age of rifting along the southern margin of the Congo Craton has been determined by Hoffman et al. (1996) at c. 756 and 746 Ma. Konopásek et al. (2014a) reported rifting-related volcanism along the south-western margin of the Congo Craton at c. 740-710 Ma (Fig. 4).

The reports of the magmatic activity with similar age along the eastern margin of the Rio de la Plata craton are from Lenz et al. (2013), who have dated the felsic and mafic granitoids from this region at c. 800-760 Ma. However, the granitoids were interpreted as a result of a magmatic arc volcanism.

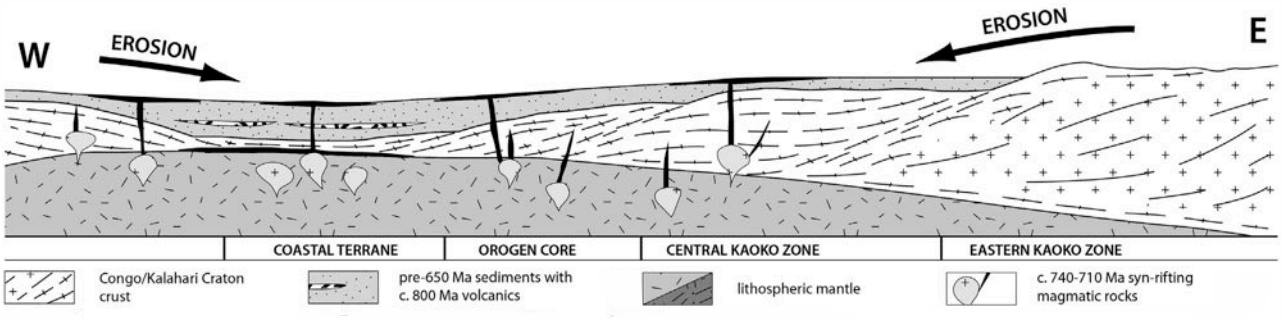

Fig 4: Model of the syn-rifting volcanism in the Kaoko Belt at c. 740-710 Ma. After Konopásek et al. (2014a).

2.2.2 The orogenic stages in the Dom Feliciano and Kaoko Belts at 650-500 Ma

The convergence of the Congo, Rio de la Plata and Kalahari cratons led to the formation of the Dom Feliciano, Kaoko, Gariep and Damara belts (Fig. 5). The tectonic evolution of the first two belts can be described by three main metamorphic events.

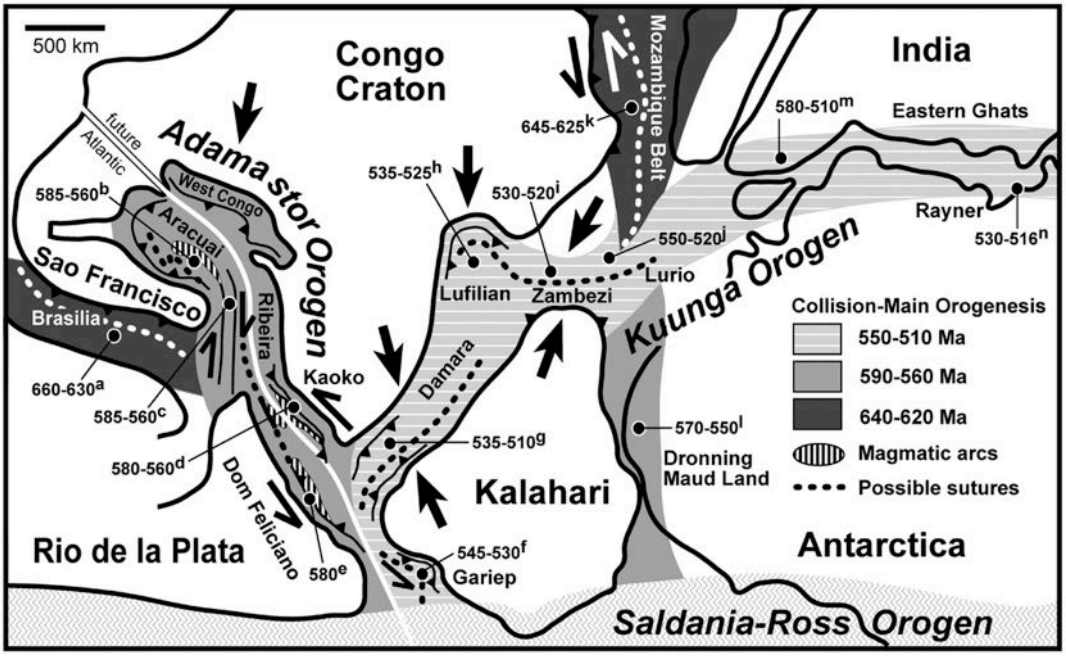

Fig 5: Structural and geochronological map of the amalgamation of western Gondwana. Three main events have been proposed: 650-620 Ma - Brasilia and Mozambique Belts, 590-560 Ma - Adamastor Orogen and Dronning Maud Land and 535-510 - Graiep Belt and Kuunga Orogen. After Goscombe and Gray (2008).

2.2.3 Metamorphic period in the Dom Feliciano and Kaoko Belts at 650 - 630 Ma

Low-pressure high-temperature granulite- to amphibolite-facies rocks in the Coastal Terrane of the Kaoko Belt indicates a metamorphic event (M1) at c. 650-645 Ma (Goscombe and Gray, 2007). The metamorphism with similar age is also present in the Punta del Este Terrane of the Dom Feliciano Belt. Here, an age of c. 641 Ma was obtained by dating metamorphic rims of zircons from orthogneisses by Oyhantcabal et al. (2009a). The presence of the I-type granitoids in both regions synchronous with M1 metamorphic peak suggest subduction-related arc development (Oyhantcabal et al., 2009a).

A simplified model of Oyhantcabal et al. (2011) suggests the presence of an exotic 655-645 Ma old Coastal-Punta del Este Terrane as a separate geological unit (Fig. 6b) prior its 580-550 Ma collision with the Congo Craton. Recently Konopásek et al. (2014a) reported the presence of c. 650 Ma detrital zircons within the upper sedimentary cover of the Congo craton (Fig. 7) indicating a close proximity of the Congo craton and the Coastal Terrane - Punta del Este already before the c. 580-550 Ma collisional stage, which apparently contradicts the interpretation of the Coastal-Punta del Este Terrane as an exotic crustal block.

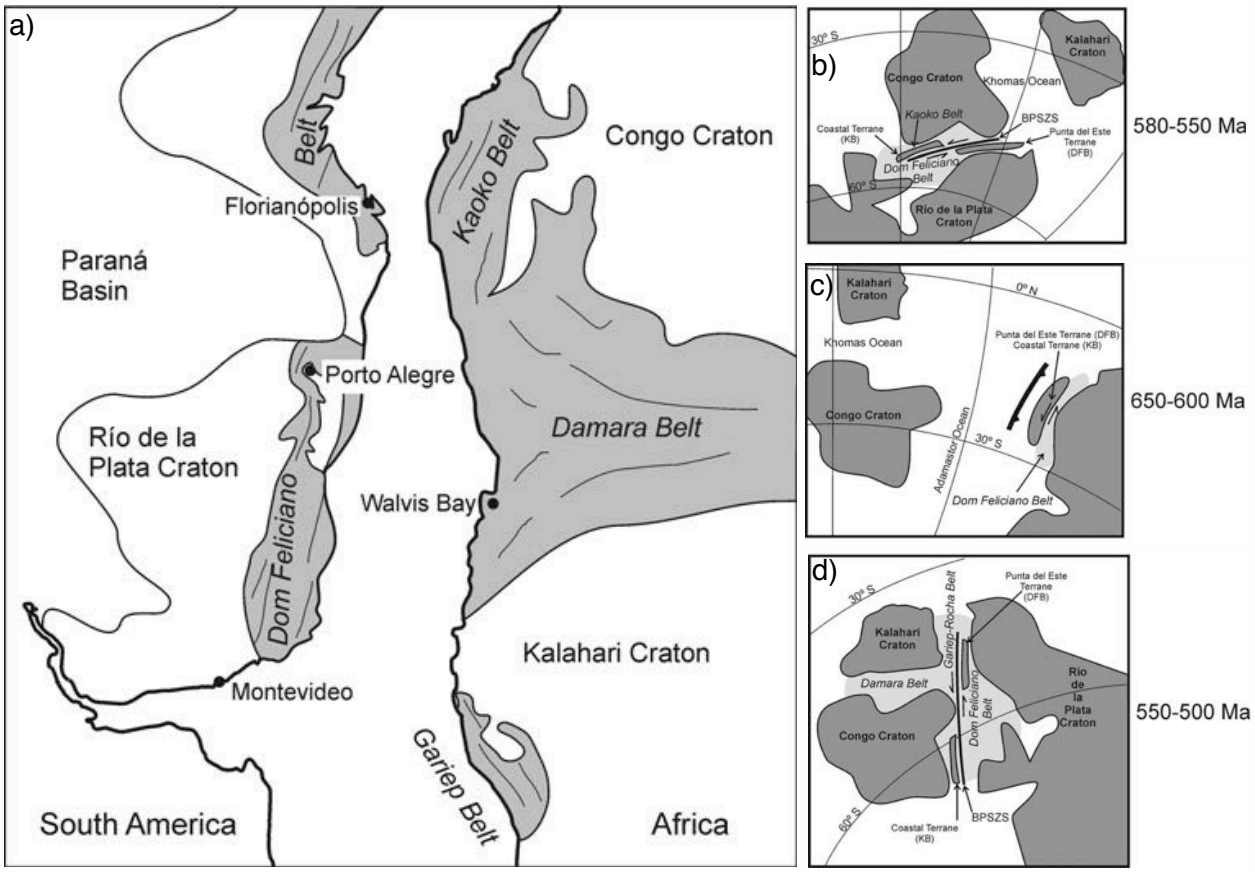

Fig. 6: a) Schematic figure showing the relative positions of the cratons and orogenic belts along the southern Atlantic coasts. b) Sinistral movement of the Coastal Terrane - Punta del Este at c. 650-600 Ma. c) The transpressional collision at c. 580-550 Ma. d) Final stage subsequent to the collision, here involving the Kalahari Craton creating the Damara Belt. Figures after Gray et al. (2008), Oyhantcabal et al. (2011).

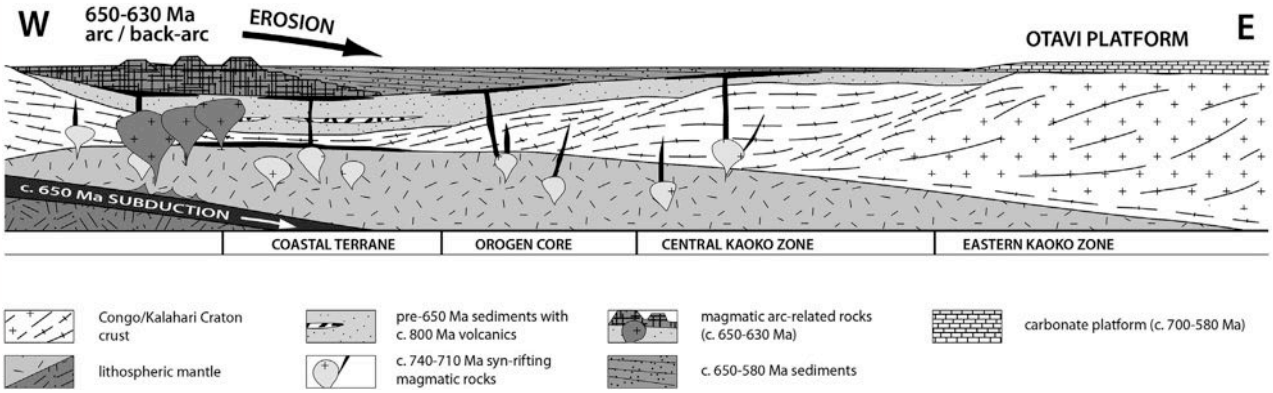

Fig. 7: Model for arc development in the Kaoko Belt due to eastward subduction. Erosion of the magmatic arc and the Congo Craton provide the detrital material for the upper sedimentary cover of the cratonic basement. After Konopásek et al. (2014a).

2.2.4 Metamorphic event in western Gondwana at 580-550 Ma

The collision of the Congo and Rio de la Plata cratons took place at c. 580-550 Ma (Goscombe and Gray, 2007; Oyhantcabal et al. 2011). The structural coherence between the Dom Feliciano Belt and the Kaoko Belt is inferred due to similar sinistral transpressional deformation (Fig. 6c) and common presence of large-scale transcurrent sinistral shear zones suggesting overall oblique convergence of the Congo and Rio de la Plata cratons. (Fernandes and Koester., 1999; Goscombe & Gray., 2007; Oyhantcabal et al., 2009a).

2.2.5 Post collisional stage in western Gondwana at 550-500 Ma

The post-collisional 550 - 500 Ma sinistral transpression marked the final movements in western Gondwana, separating the Coastal Terrane and Punta del Este Terrane, while the Graiep- and Damara belts were created (Fig. 6d).

The Ballena-Purros shear zone system indicates the final displacement of over 100 km between the Coastal Terrane and the Punta del Este Terrane (Oyhantcabal et al., 2011).

Foster et al. (2009) have presented indications of differential exhumation at c. 530-520 Ma in the Kaoko Belt, and associated it with the final closure of the Damara Belt. Contradictory to that model is the idea of oblique extension of the orogen core during ongoing transpression (Goscombe and Gray, 2008).

2.2.6 Correlations between the Dom Feliciano and Kaoko Belts

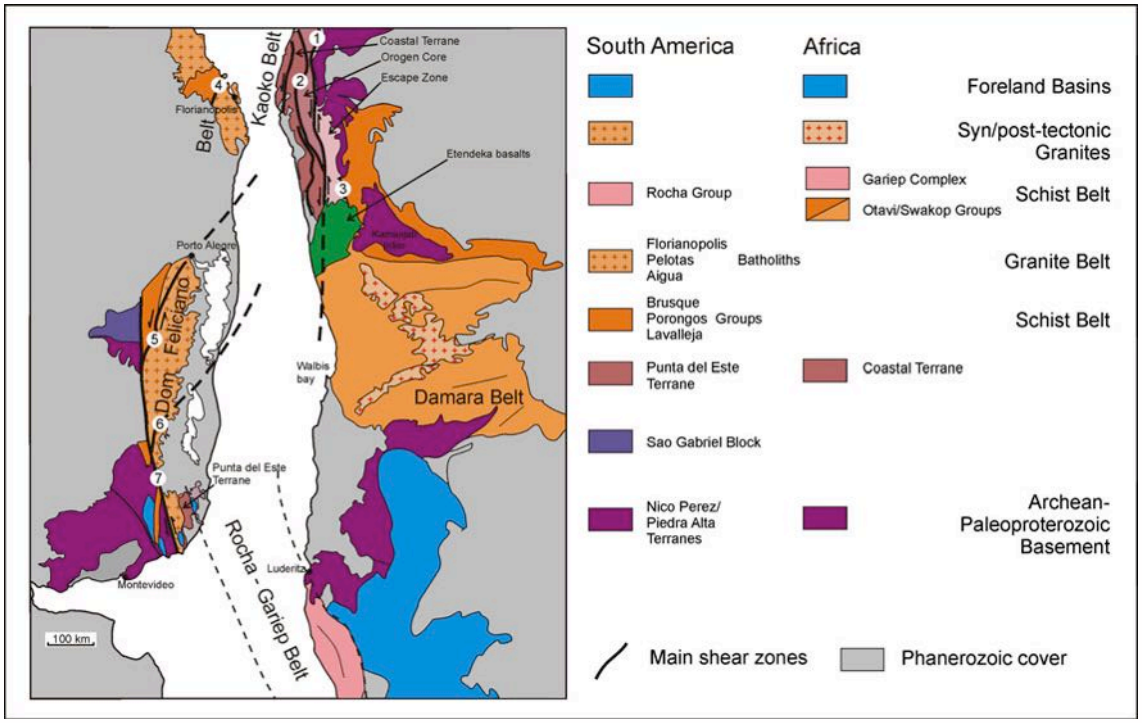

Fig 8: Structural map comparing the geological units of the Kaoko, Damara, Gariep and Dom Feliciano belts. Shear zones are labelled with numbers: 1) Purros, 2) Three Palms, 3) Sesfontein thrust, 4) Major Gercino,) Dorsal de Cangucu, 6) Cerro Amaro, 7) Sierra Ballena. After Oyhantcabal et al. (2011)

Due to similarities in lithological, isotopic and structural data the Dom Feliciano Belt has been correlated with the Kaoko Belt (Fig. 8) by several authors (Passchier et al., 2002; Goscombe and Gray, 2007; Konopásek et al., 2008; 2014a; Oyhantcabal et al., 2011).

Fig. 8 presents similarities in various tectonic units involving the foreland basins, schist belts, granite belts, terranes and basement rocks in the Kaoko, Damara, Gariep and Dom Feliciano belts. The figure represents a compilation of data from the South American side (Basei et al., 2000, 2005; Hartman et al., 2001, 2002; Philipp & Machado, 2005; da Silva et al., 2005; Oyhantcabal et al., 2007, 2009a), and from the South African side (Gray et al., 2006; Goscombe and Gray, 2008; Gray et al., 2008) of the Kaoko-Gariep-Dom Feliciano orogenic belt system.

3 Study area

The samples were collected from high-grade migmatitic metasediments and quartzites of the Punta del Este Terrane in the Dom Feliciano Belt in Uruguay and from the Coastal Terrane of the Kaoko Belt in Namibia. The fieldwork was not included in this master project and the samples have been collected by Jiri Konopásek between the years 2008 and 2013.

3.1 The Dom Feliciano Belt

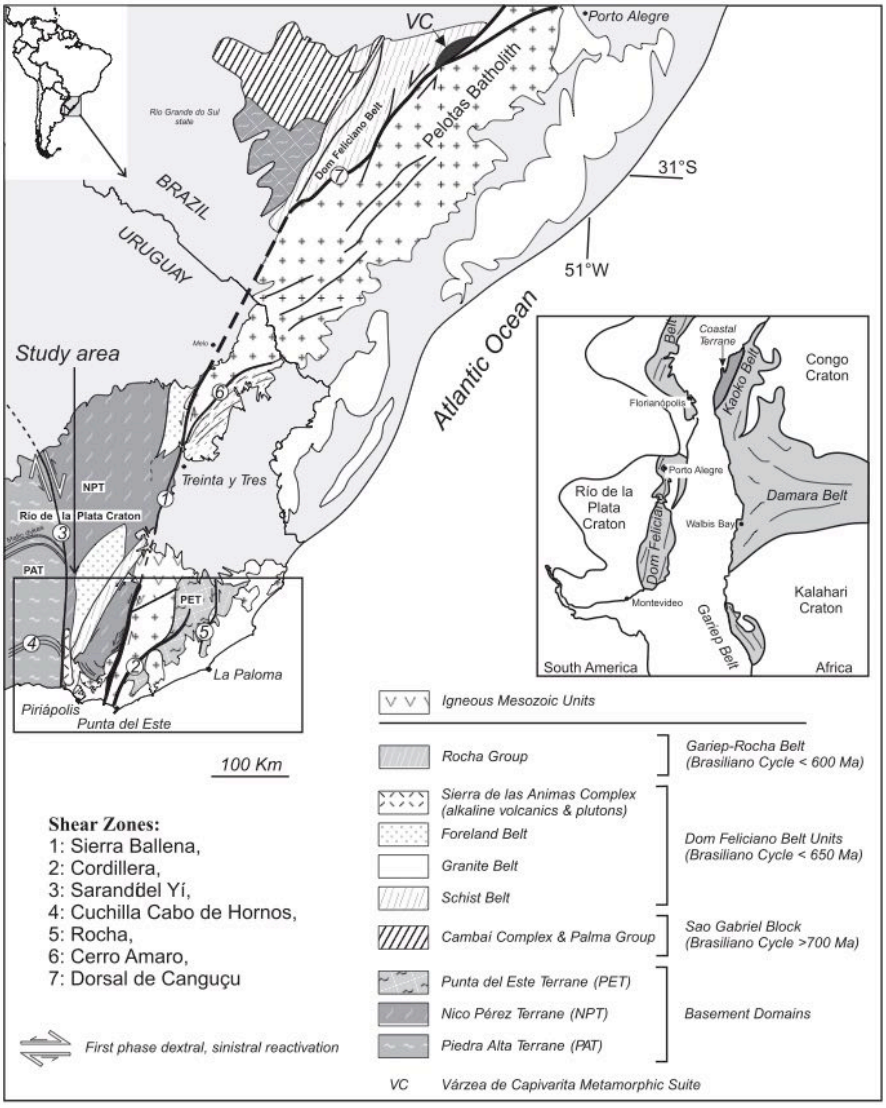

Fig. 9: Geological map showing the main tectonic units of the Dom Feliciano Belt and their age relations.
The area of study is shown in the box to the left and presented in detail in Fig. 10. The assumed spatial relationship to the Neoproterozoic orogenic belts in southwestern Africa is shown on the right. The map is from Oyhantcabal et al. (2009a), and was compiled based on data from Basei et al. (2000, 2005), Hartmann et al. (2001, 2002), da Silva et al. (2005), Philipp & Machado (2005) and Oyhantcabal et al. (2007).

The exposed part of the Dom Feliciano Belt has a length of c. 1200 km and width of c. 150 km. It is stretched in SW-NE direction, parallel to the Atlantic Coast in southeastern Brazil and Uruguay (Fig. 9). Basei et al. (2000) has divided the Dom Feliciano Belt into three tectonic units: the Granite Belt, the Schist Belt and the Foreland Belt. The Granite Belt is subdivided into Aiguá Batholith (southernmost part in Uruguay), Pelotas Batholith and Florianopolis Batholith (southeastern Brazil). These batholiths are interpreted to represent the post-collisional magmatism related to the amalgamation of western Gondwana by Oyhantcabal (2007), while Basei et al. (2000) proposed the batholiths as being roots of a subduction-related magmatic arc. The Rio de la Plata Craton makes up the western cratonic foreland of the Dom Feliciano Belt (Fig. 9) and is divided by the Sarandí del Yí Shear Zone into the Piedra Alta Terrane and the Nico Pérez Terrane (Fig. 10). The Schist Belt is made up by Neoproterozoic metavolcanics and metasedimentary sequences, characterized by greenschist- to amphiblite-faceies rocks (Oyhantcabal et al., 2009a), with ages of c. 783 Ma obtained from the Porongos Group in southeastern Brazil (Porcher et al., 1999). The Neoproterozoic age of the Schist Belt was confirmed by the detrital zircon study of Basei et al. (2008a).

3.1.1 The Punta del Este Terrane

The Punta del Este Terrane represents the southern- and easternmost part of the Dom Feliciano Belt in Uruguay and it is exposed along the coast of the Atlantic Ocean (Figs 9 & 10). The Punta del Este Terrane is characterized by the presence of granulites, paragneisses, high-grade orthogneisses and augen gneisses (Oyhantcabal et al., 2009a; Gross et al., 2009; Lenz et al., 2011). Geochronological studies of orthogneiss and granulite samples from this region indicate a magmatic event at c. 800-760 Ma, followed by a high grade metamorphic event and granitoid emplacement at c. 650-620 Ma (Oyhantcabal et al., 2009a; Lenz et al., 2011).

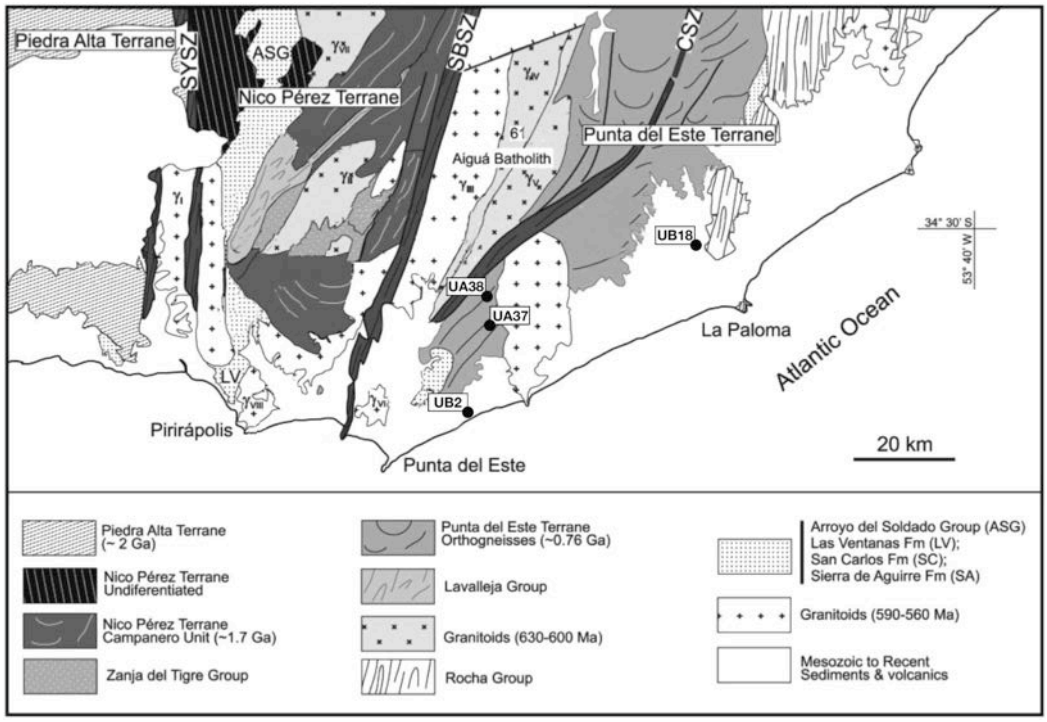

Fig. 10: Simplified geological map of the Punta del Este Terrane, Uruguay showing the localization of the samples UA37, UA38, UB2 and UB18. CSZ - Cordillera Shear Zone, SYSZ - Sarandí del Yí Shear Zone, SBSZ - Sierra Ballena Shear Zone. Modified after Oyhantcabal et al. (2009a)

Samples of orthogneisses and metasediments of the Punta del Este Terrane in Uruguay were collected by Jiri Konopásek in 2012 and 2013. Two samples (UA37 & UB18) of quartzites from the high-grade metasediments were collected for the detrital zircon analysis and two samples (UA38 & UB2) of metagranitoids were collected for the study of protolith zircons. The samples are marked in Fig. 10 and their coordinates given in Table 1.

Sample	Locality	Lithology	Coordinates	Type of analysis
UA37	Punta del Este Terrane	Quartzite	S34.68.178, W54.72.519	Detrital zircons
UA38	Punta del Este Terrane	Orthogneiss	S34.64.826, W54.73.200	Magmatic zircons
UB18	Punta del Este Terrane	Quartzite	S34.49.338, W54.35.990	Detrital zircons
UB2	Punta del Este Terrane	Quartz-feldspatic gneiss	S34.90.799, W54.82.564	Magmatic zircons

Table 1: Names, localities, lithologies and GPS coordinates of the samples collected in the Punta del Este Terrane, Uruguay.

3.2 The Kaoko Belt

The Kaoko Belt is a transpressional orogenic system that stretches by a length of 800 km and width of 180 km along the Atlantic coast of northern Namibia (Goscombe and Gray, 2007). Miller (1983) proposed the division of the Kaoko Belt into three tectonic zones;
The Eastern Kaoko Zone is a c. 2 km thick Neoproterozoic sedimentary sequence deposited on top of the cratonic basement (Epupa and Kamanjab inliners; Fig. 11). The sedimentary succession has the rifting-related Nosib Group quartzites at the bottom and carbonates of the Otavi Group on the top (Fig. 11). No absolute ages were obtained from the Eastern Kaoko Zone. The Central Kaoko Zone is thrust over the Eastern Kaoko Zone, along the Sesfontein thrust. The Central Zone is a unit of metasediments with the metamorphic grade from greenschist to granulite facies underlined by the Congo Craton basement (Franz et al., 1999, Goscombe et al., 2003b). The Western Kaoko Zone is built of granulite-facies rocks. It has been further subdivided by Goscombe et al. (2005b) into the easterly Orogen Core and the Coastal Terrane towards the west (Fig. 12).

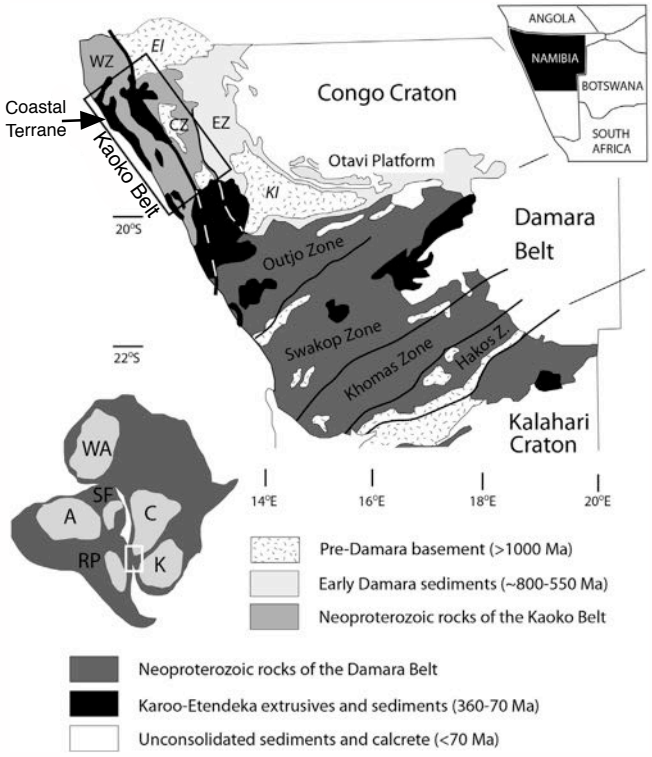

Fig 11: Simplified geological map showing the main tectonic units of the Kaoko Belt.
(WZ - Western Kaoko Zone, CZ - Central Kaoko Zone, EZ - Eastern Kaoko Zone, KI: Kamanjab Inlier, EI: Epupa Inlier).. The rectangle shows the extent of the geological map in Fig. 12. The cratons in the lower left inset are: A - Amazon, C - Congo, K - Kalahari, RP - Rio de la Plata, SF - Sao Francisco, WA - West African. After Konopásek et al., (2014a).

3.2.1 The Coastal Terrane

The Coastal Terrane represents the westernmost part of the Kaoko Belt in Namibia (Figs 11 & 12) and it is characterized by amphibolite to granulite facies metasedimentary and metaigneous rocks (Goscombe and Gray, 2007) metamorphosed at c. 650-630 Ma (Franz et al., 1999; Konopásek et al., 2008). Large volumes of granitoid rocks with ages between c. 800 and 550 Ma indicate several periods of magmatic activity in this unit (Seth et al., 1998; Kröner et al., 2004; Konopásek et al., 2008). No pre-Neoproterozoic rocks, i.e. no exposed basement rocks have been recorded in the Coastal Terrane. The whole unit has been interpreted as a volcanic arc/back arc terrane by Goscombe et al. 2005b. Due to unique geochemical signature, and the Neoproterozoic ages only found in the Coastal Terrane, Goscombe and Gray (2007) interpreted the Coastal Terrane-Punta del Este as an exotic block, with a different pre-collisional history than the Congo Craton passive margin.

In contradiction to the model of Goscombe and Gray (2007), Konopásek et al., (2014a) suggested that the Coastal Terrane developed in close proximity to the Congo Craton passive margin, due to the presence of detrital zircons with ages of c. 740-710 Ma and c. 650 Ma (i.e. derived from the Coastal Terrane) in the upper Neoproterozic strata overlying the Congo Craton margin.

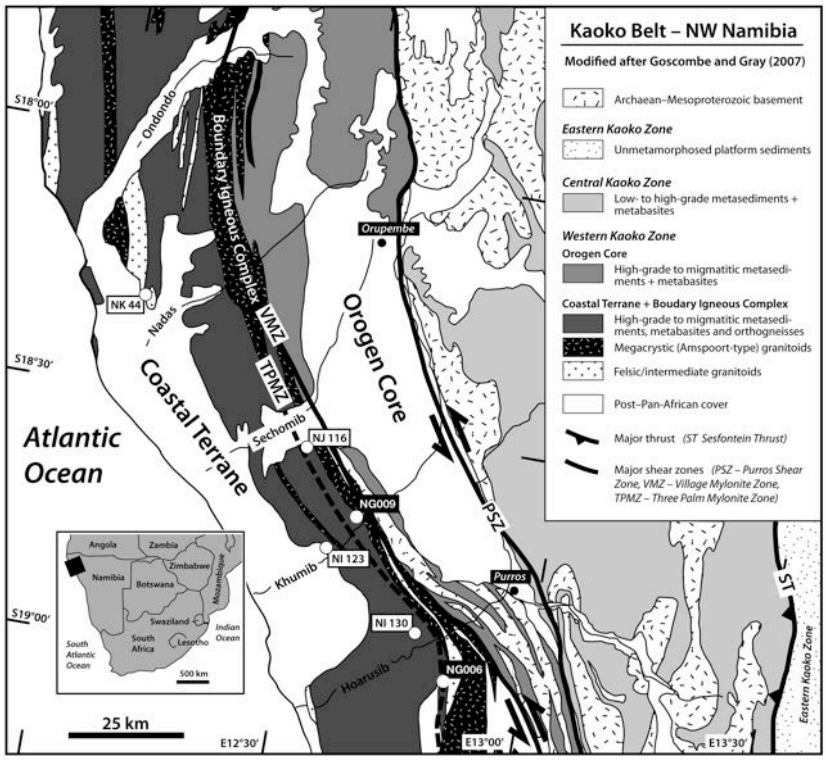

Fig. 12: Simplified geological map of the Kaoko Belt showing the locations of the samples NI123, NI130, NK44 and NJ116. Samples NG006 and NG009 (inverse markings) are the quartzite samples presented in Konopásek et al. (2014a). After Goscombe & Gray (2007) and Janoušek et al. (2010).

Three samples of migmatitic gneisses (NI123, NI130 and NK44) and one sample of quartzite (NJ116) from the Coastal Terrane were collected by Jiri Konopásek in years 2008 to 2011 (Fig 12 & Table 2). All of the samples were collected for the detrital zircon analysis.

Sample	Locality	Lithology	Coordinates	Type of analysis
NI123	Coastal Terrane, Sechomib river	Migmatitic gneiss	S18.74.843 E12.58.937	Detrital zircons
NI130	Coastal Terrane, Hoarusib river	Migmatitic gneiss	S18.87.008 E12.77.237	Detrital zircons
NJ116	Coastal Terrane, Sechicomb	Quartzite	S18.55.130 E12.47.343	Detrital zircons
NK44	Coastal Terrane, Nadas river	Migmatitic gneiss	S18.31.677 E12.08.798	Detrital zircons

Table 2: Names, localities, lithologies and GPS coordinates of the samples collected in the Coastal Terrane, Namibia.

4 Methods

The methods used in this study included mineral separation, sample mount preparation, cathodoluminescence imaging, LA-ICPMS analysis and data processing.

4.1 Mineral separation

Preparation of the samples was done in the crushing rooms and mineral separation labs at Realfagbygget, University of Bergen.

The cobble sized rock samples were first crushed with a hammer into sizes of 5-30 mm (Fig. 13a). The samples were further milled in the Firsh Diskmill and sieved manually into fractions with grain size smaller and larger than 315 μm (Fig. 13b).
The < 315 μm fraction was brought on to the Holman Wilfey shaking table (Fig. 13c) to separate the heavy minerals ($\rho \geq 2.80$ g/cm^3) from the lighter minerals. Three fractions were set up, where the heavy fraction was kept for further separation, the second for backup and the third fraction of the light minerals was discarded.

The first fraction of the heavy minerals was brought into the separation lab where strongly ferromagnetic minerals like magnetite were removed manually by a handheld magnet, while the rest of the fraction was introduced into the Franz Ferromagnetic Separator (Fig. 13d) to remove weakly ferromagnetic minerals like hematite e.g. The magnetic separator was set to an angle of about 14° and current to 0,6A in order to separate weakly ferromagnetic minerals into one container and apatite and zircon into the other (Fig. 13d).
The fraction was then brought into heavy liquid Sodium Polytungstate (SPT) with a density of 2.80 g/cm^3 (Fig. 13e), in order to make remaining quartz (ρ = 2.65-2.66 g/cm^3) and feldspar (ρ = 2.66 g/cm^3) in the fraction float on top, and apatite (ρ = 3.10-3.20 g/cm^3) and zircon (ρ = 4,60-4.70 g/cm^3) sink to the bottom of the solution. The fraction was washed with deionized water.

The magnetic separator was once again used with the same angle and 1,2A in order to separate weakly magnetic heavy minerals like monazite and titanite into one container, and the heavy minerals apatite and zircon into the other. The fraction was cleaned with acetone before bringing it into the heavy liquid (ρ = 3.10-3.20 g/cm^3) diiodmethane (DIM) displayed in Fig. 13f. DIM was applied to make apatites float on top, and the zircons to sink to the bottom of the solution. The fraction was once again cleaned with acetone, filtered and put into a heat locker for drying.

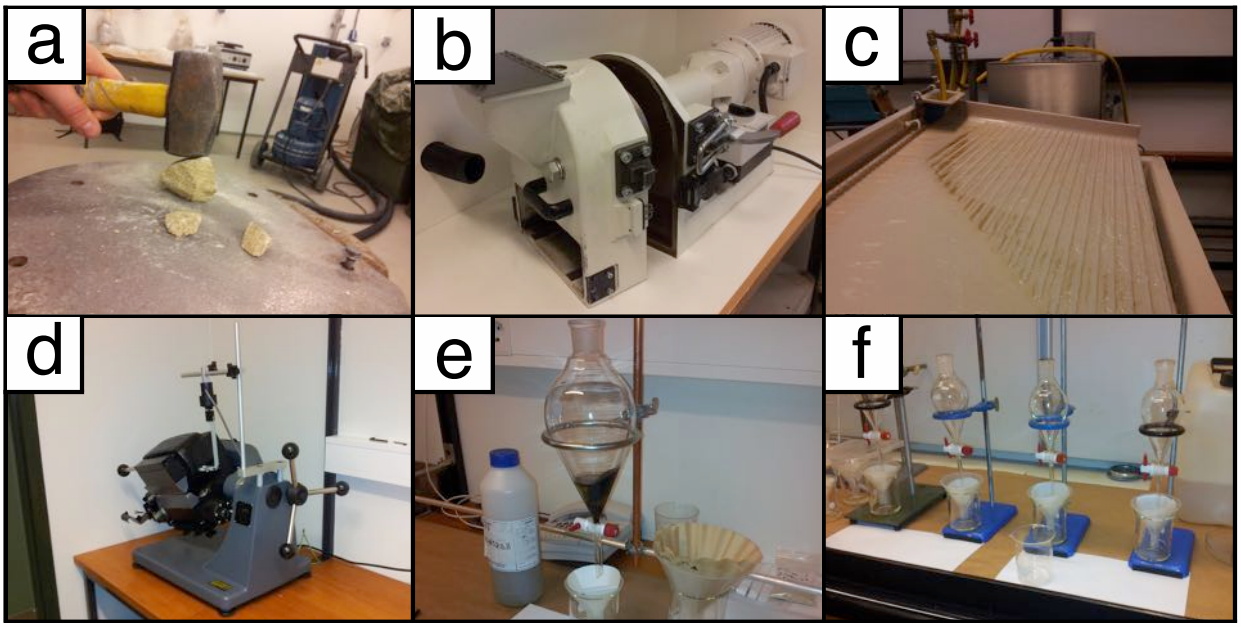

Fig. 13 a) Crushing samples with a hammer in the coarse crushing room. **b)** Frish Pulverisette Diskmill. **c)** Holman Wilfey shaking table **d)** Franz Ferromagnetic Separator, for separation of ferromagnetic and non-ferromagnetic minerals. **e)** SPT heavy liquid separation to separate the heavy minerals from the lighter minerals. **f)** DIM heavy liquid separation for separation of zircons (ρ = 4.60 g/cm^3) from apatite (ρ = 3.16-3.22 g/cm^3) e.g.

4.2 Mount preparation

After the samples dried in the heat locker, the zircon concentrate was brought on to a beaker and put under an optical microscope (Fig. 14a). The clearest zircon grains were picked out with a pin and put in a square pattern onto a glued glass surface (Fig. 14b, c). The number of zircons picked from each samples was between 120 and 300 (Fig. 14d).

The zircons were then mounted with epoxy resin in a circular mount (Fig. 14e, f), polished down manually with aluminum oxide powder at 800 *µm* and 1200 *µm* (Fig. 14g), further polished with diamond and lubricant blue on DP-02 for 2 minutes at 6 *µm* and aluminum oxide powder on DP-02 for 1 minute at 0.5 *µm* (Fig. 14h).

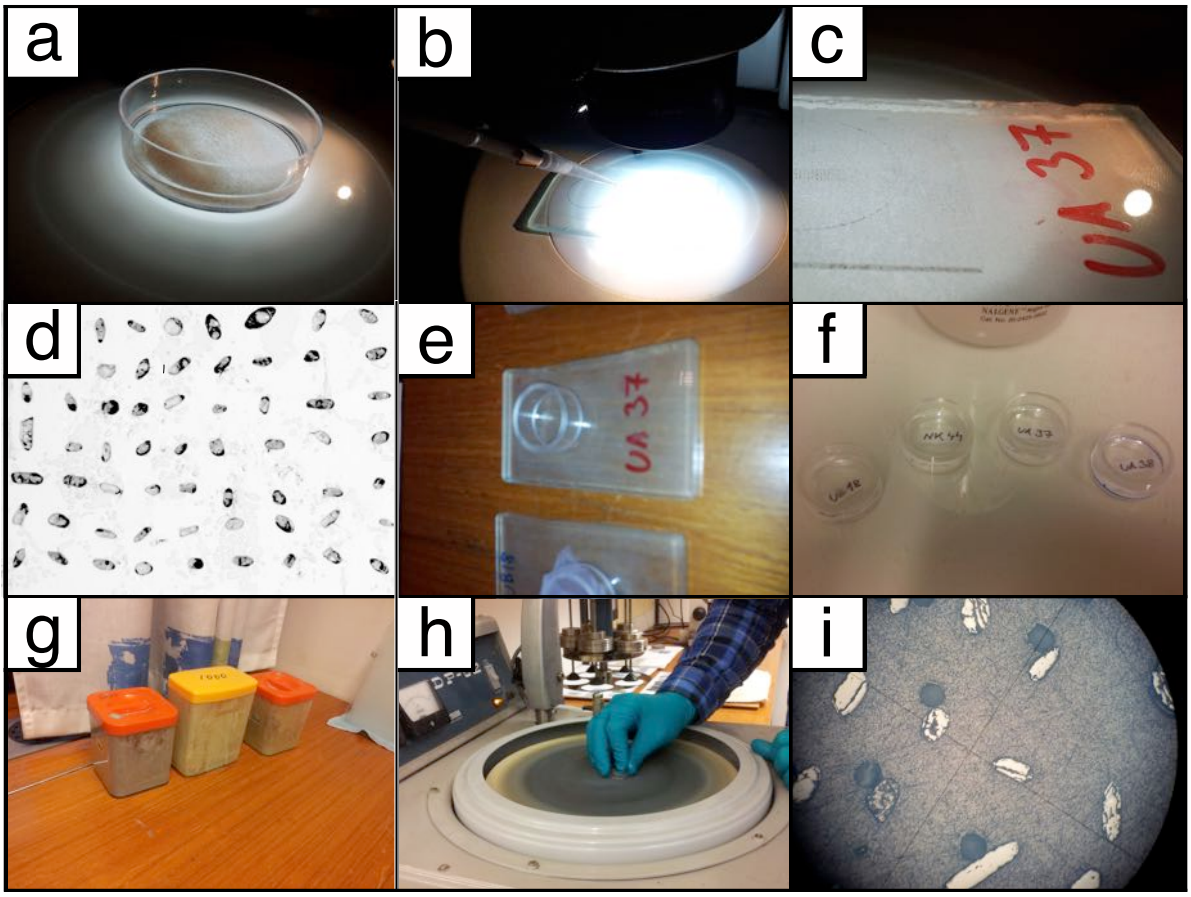

Fig. 14 a) Zircons are mixed with ethanol in a beaker under a Leica optical microscope. **b)** The zircons are transported from the beaker to the glass plate. **c)** The grains are sticked onto a double sided tape on the plate. **d)** Leica microscope picture, the grains are ordered in a matrix pattern. Size 80-120 *µm* in the B-axis. **e)** A circular mount is set onto of the zircons, and filled with glue. **f)** After one day the samples are ready for polishing. **g)** Aluminum powder is applied in the first manual stage of polishing. **h)** Polishing on the DP-02 machine at 6 *µm* and 0.5 *µm*. **i)** View of almost exposed zircon in a polished mount under a light microscope.

4.3 Cathodoluminescence imaging

Cathodoluminescence (CL) images were taken by a Zeiss Supra 55VP Scanning Electron Microscope at the scanning electron microscope (SEM) laboratory at Realfagbygget, University of Bergen. The circular mounts with zircons were first carbon coated, then the mounts were taped onto a stage (Fig. 15a) and then set into the SEM sample cell for imaging. The zircon imaging was made by a Zeiss Supra 55VP SEM with a Thermo electron source and MAXray ion detector (Fig. 15b).

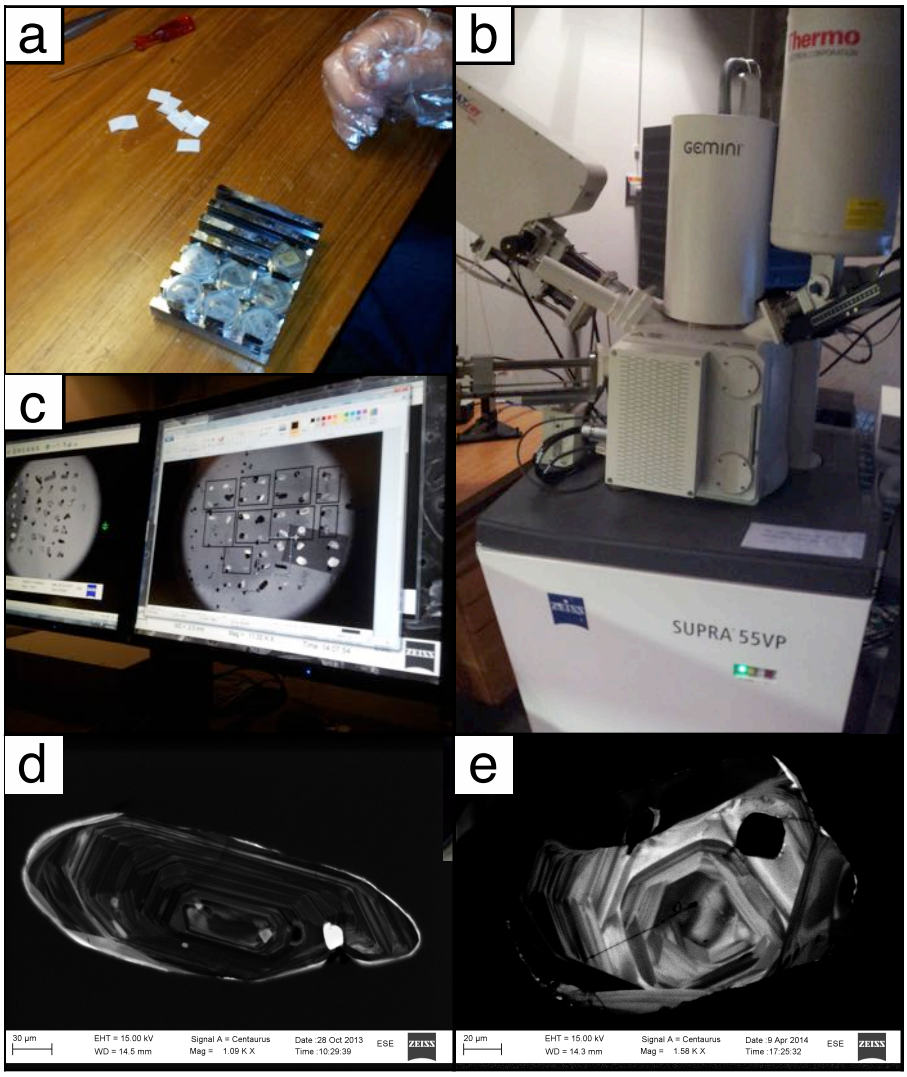

Fig. 15 a) Zircon mounts gets taped on the stage for the SEM sample cell. **b)** Zeiss Supra 55VP, Thermo electron source and MAXray ion detector. **c)** Live view of the cathodoluminescence imaging, here for mapping of the zircons. **d)** Zircon example from UA38 showing oscillatory zoning and inclusions. **e)** Zircon example from UB18 showing a complex core, partly oscillatory zoning, fractures, inclusions and metamorphic overgrowths.

4.4 Laser Ablation Inductively Coupled Plasma Mass Spectrometry Intrumentation

Heavy mineral (density over 2.80 g/cm^3) analysis is a key tool for determination of sediment provenance (Zuffa, 1985), as due to their refractory properties they are present in most sedimentary rocks (Fedo et al., 2003). Dating of other heavy and U-bearing accessory minerals (e.g. apatite, titanite or rutile) may be compromised by the presence of common Pb, that can result in calculation of erroneous isotopic U-Pb ages (Chew et al., 2014).
Zircon has the formulae $ZrSiO_4$, and can contain rare earth elements (REE), radioactive isotopes of thorium (Th) and uranium (U) at concentrations of 1-1000 ppm, making this mineral ideal for radiometric dating (Davis et al., 2003). The decay of ^{238}U to ^{206}Pb has a half life ($t_l/_2$) of 4.468 Ga, ^{235}U decays to ^{207}Pb with a $t_{1/2}$ = 704 Ma and ^{232}Th to ^{208}Pb with a $t_{1/2}$ = 14.1 Ga (Davis et al., 2003). Dating of detrital zircons is a useful tool for interpretations of possible source regions, for stratigraphic correlations, and transport and depositional history (Morton et al., 1996; Košler et al., 2002).

The Laser Ablation-Inductively Coupled Plasma Mass Spectrometry (LA-ICPMS) is the most available, cheapest and fastest way of U-Pb dating (Jackson et al., 2004) and for the dating of large number of zircons in detrital samples it is the most efficient method to use (Košler et al., 2002).
The LA-ICPMS is made up by a laser ablation cell (Fig. 16a), an ICP-torch and a mass spectrometer (Fig. 16b). The ICPMS mainly consists of the following four parts: an ion source, a mass filter, a vacuum system and a detector.

Within the ablation cell the laser hits parts the zircons and turns it into an aerosol that is carried into the ICPMS. Before the introduction into the ICPMS the sample is mixed with an Argon/Helium gas. The aerosol is then transported into plasma at 8000-1000 K that dissolves the atoms and ions carried in the sample gas (Košler & Sylvester, 2003). The ions are carried through cones into the mass spectrometer. The beam is then focused through a series of lenses and the ions are discriminated through a magnetic separator due to their mass/charge proportions. Finally, the signal is recorded by the detection system (Košler & Sylvester, 2003).

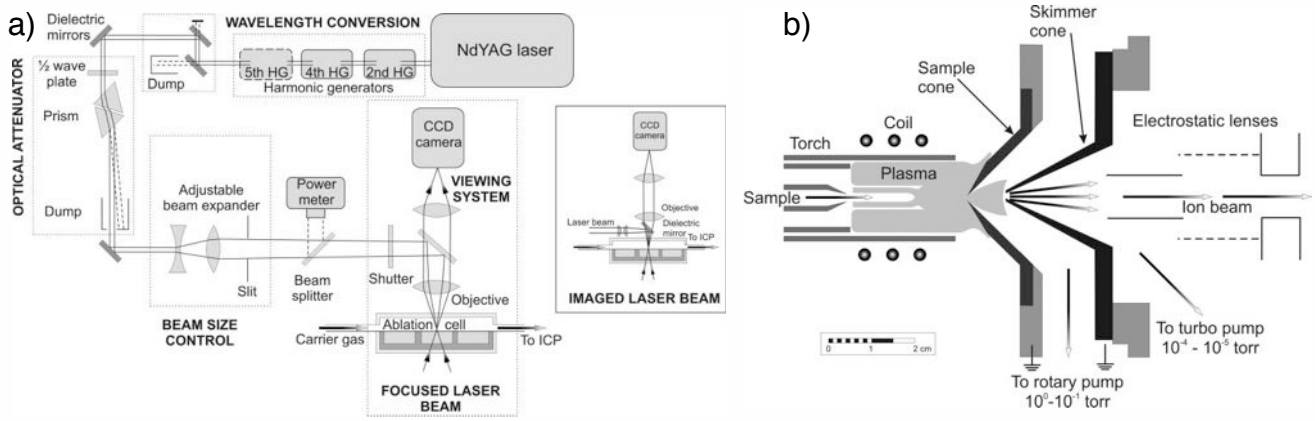

Fig 16: a) Schematic figure of a typical laser ablation setup. After Košler & Sylvester (2003). b) Schematic cross section of a plasma source and sample introduction system. After Košler & Sylvester (2003).

4.5 LA-ICPMS Analysis

The LA-ICPMS analysis of detrital and magmatic zircons was done in the ICPMS lab at Realfagbygget at the University of Bergen. After the CL imaging, the mounts were re-polished with aluminum powder at 0.05 *μm* to remove the carbon coating. The mounts were rinsed with diluted HNO_3, brought in a deionized water into an ultrasonic bath, scanned for mapping and set into the Laurin sample cell (Fig. 17b) of the Resonetics RESOlution M-50 LR (Fig. 17a) 193 nm ArF excimer laser. The laser was fired with an energy of 80 mJ, frequency of 5 Hz and a beam diameter of 19 *μm*. An acquisition measures a blank for 25 seconds and subsequently measures the U and Pb signal from the ablated zircons for 30 seconds (Further described in Sláma et al., 2008). The acquired data were analyzed in pulse counting mode, with one measured point for each mass peak for ^{204}Pb, ^{206}Pb, ^{207}Pb, ^{208}Pb, ^{232}Th, ^{235}U and ^{238}U. Further details on data reduction are described in Paton et al. (2010).

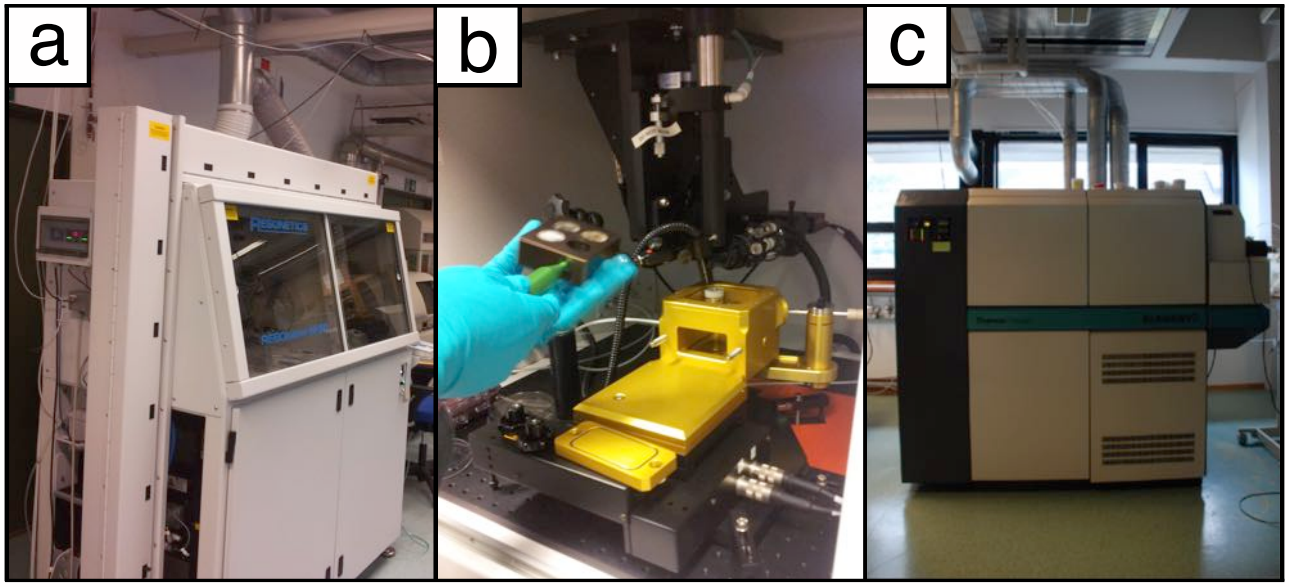

Fig. 17: Instrumentation for LA-ICPMS analysis. **a)** Resonetics RESOlution M-50, 193 *nm* laser. **b)** Laurin sample cell, sample mount to the left. **c)** Thermo-Finnigan Element 2 for ICPMS analysis, (picture by Hallgeir Sirevaag).

4.6 Data processing

Data reduction was carried out in Iolite for Igor Pro 6, involving correction for gas blanks, elemental fractionation (laser-induced fractionation of Pb and U) and instrument bias.

The correction for blank intensities and instrumental bias was corrected for through interpolation of the signal in an automatic spline function, while the elemental fractionation was corrected for in an exponential down-hole correction. The instrument bias and residual elemental fractionation was corrected for by normalizing to the standard reference material GJ-1 (609 Ma; Jackson et al., 2004). The reference material 91500, with a reference value of 1065 Ma (Wiedenbeck et al., 1995) was applied for quality control, and the Plešovice standard (337 Ma) was used for matrix-matched calibration (Sláma et al., 2008).

Signal noise from the data is reduced by selecting time interval for subtraction of the baseline for all of the data, followed by giving name, setting time interval and distinguishing the 91500, GJ1 and Plešovice standards from the sample data. The data were then processed and exported.

The data were exported from Igor Pro 6 and imported to Microsoft Excel. Discordance between the $^{238}U/^{206}Pb$ and $^{235}U/^{207}Pb$ ratios was calculated with a percentage filter set to 5% and 10% in excel. The data that were < ± 10% discordant were used for the detrital zircon populations evaluation, and those < ± 5% discordant were considered in case of the zircon from metamorphosed magmatic rocks. Additionally a < ± 10% filter was set in Excel for the individual isotopic $^{238}U/^{206}Pb$ and $^{235}U/^{207}Pb$ ages to their respective 2σ errors. Isoplot 4.15 (Ludwig, 2003) software was used to present concordia diagrams from $^{238}U/^{206}Pb$ and $^{235}U/^{207}Pb$ ratios and to calculate the concordia ages for the meta-igneous samples.

DensityPlotter 5.0 (Vermeesch, 2012) was used to plot Kernel Density curves to visualize the distribution of ages from the detrital zircon data. Due to the accuracy of the isotopic age calculations, $^{238}U/^{206}Pb$ ages were chosen for the <1 Ga ages, and $^{207}Pb/^{206}Pb$ ages for the >1 Ga ages.

Morton et al. (1996) suggested a minimum of 50 detrital zircons as statistically significant in provenance studies, while Košler et al. (2002) suggested a minimum number of 80 zircons. Table 3 shows the numbers of analyzed and accepted grains in the eight samples from this study.

Sample	Study area	Lithology	Analyzed zircon grains	Accepted zircon grains
UA37	Punta del Este	Quartzite	272	93
UA38	Punta del Este	Orthogneiss	38	24
UB2	Punta del Este	Quartz-feldspatic gneiss	67	50
UB18	Punta del Este	Quartzite	75	38
NI123	Coastal Terrane	Migmatitic Gneiss	98	88
NI130	Coastal Terrane	Migmatitic Gneiss	95	83
NJ116	Coastal Terrane	Quartzite	98	75
NK44	Coastal Terrane	Migmatitic Gneiss	111	99

Table 3: Overview of the analyzed and accepted zircons in this study. Sample UA37, UB18, NI123, NI130, NJ116 and NK44, the detrital zircon samples of the Punta del Este and Coastal Terrane are marked in black. The magmatic samples UA38 and UB18 from the Punta del Este Terrane are labeled in red.

5 Results

5.1 Samples from the Punta del Este Terrane, Dom Feliciano Belt, Uruguay

Three rock types from the Punta del Este Terrane have been studied. Samples UA37 and UB18 represent quartzites, sample UA38 is an orthogneiss and sample UB18 is a quartz-feldspathic gneiss.

Abbreviation:	**Ap**	**Bt**	**Chl**	**Grt**	**K-feld**	**Plag**	**Qtz**	**Rut**	**Sil**	**Zir**	**Zoi**
Mineral:	Apatite	Biotite	Chlorite	Garnet	Alkali feldspar	Plagioclase	Quartz	Rutile	Sillimanite	Zircon	Zoisite

Table 4: List for minerals abbreviated in the thin section figures.

UA37 - Quartzite

The UA37 quartzite consists of quartz, altered biotite and zoisite (Fig. 18b). The zoisite probably replaces calcium-bearing plagioclase and only little feldspar is left. The accessory minerals observed are zircon, apatite and opaque mineral, estimated to c. 5%.
The UA37 can be classified as a quartzite due to the high (>80%) quartz content, and is interpreted as metamorphosed sandstone.

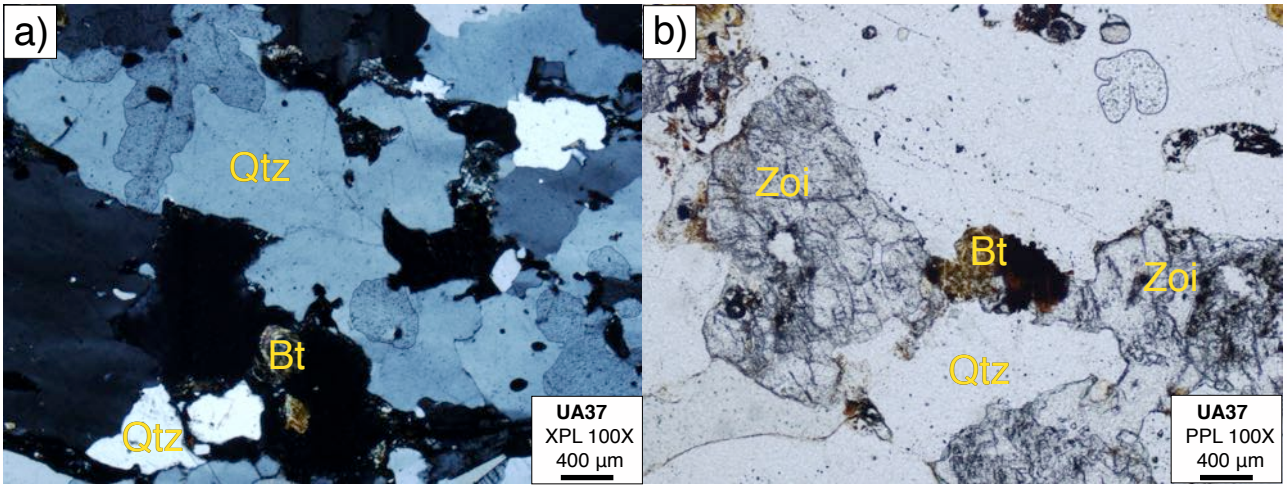

Fig. 18: a) Thin section UA37 at 100x magnification in crossed-polarized light showing quartz and altered biotite. b) Thin section UA37 at 100x magnification in plane polarized light showing zoisite, quartz and altered biotite.

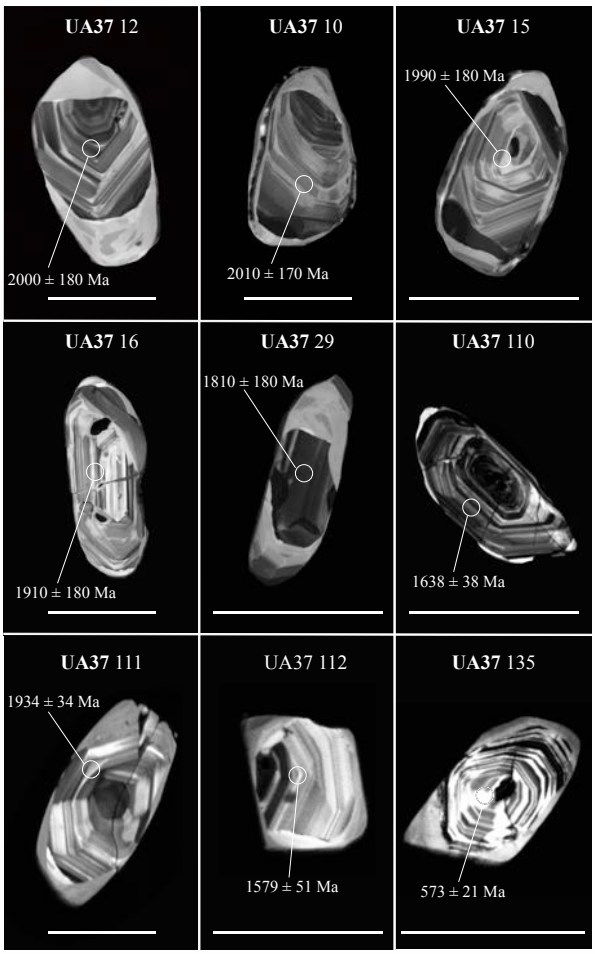

Fig. 19: CL images of typical zircons in UA37 quartzite. The circles marks the laser ablation points, and the scale bars represent 100 μm.

The zircons from UA37 range from 60 to 110 μm in width and 80 to 180 μm in length. The grains are slightly elongated with a mean aspect ratio of 1.6. A substantial number of zircon grains are subhedral and rounded. 50% of the zircon grains show fractures (UA37: 16, 110, 111 and 135 in Fig. 19) and 15% of the grains show inclusions (see UA37: 16 in Fig. 19). The majority of the zircon grains show oscillatory zoning with a darker, poorly defined cores and overgrowths towards the edges. Some show non-concentric zoning or no visible internal texture. The complex zircon textures with sharp boundaries between cores and rims indicate multi-stage zircon growth or recrystallization.

Of the 272 analyzed grains in UA37, only 93 were less than 10% discordant. The $^{206}Pb/^{238}U$ or $^{207}Pb/^{206}Pb$ ages are distributed between 540 Ma and 2.15 Ga. One $^{207}Pb/^{206}Pb$ age is recorded at 2.85 Ga. Kernel density plot and histogram of the data are presented in Fig. 20 showing age peaks at c. 610 Ma and c. 2.0 Ga, and individual data between 1.15 Ga and 2.0 Ga.

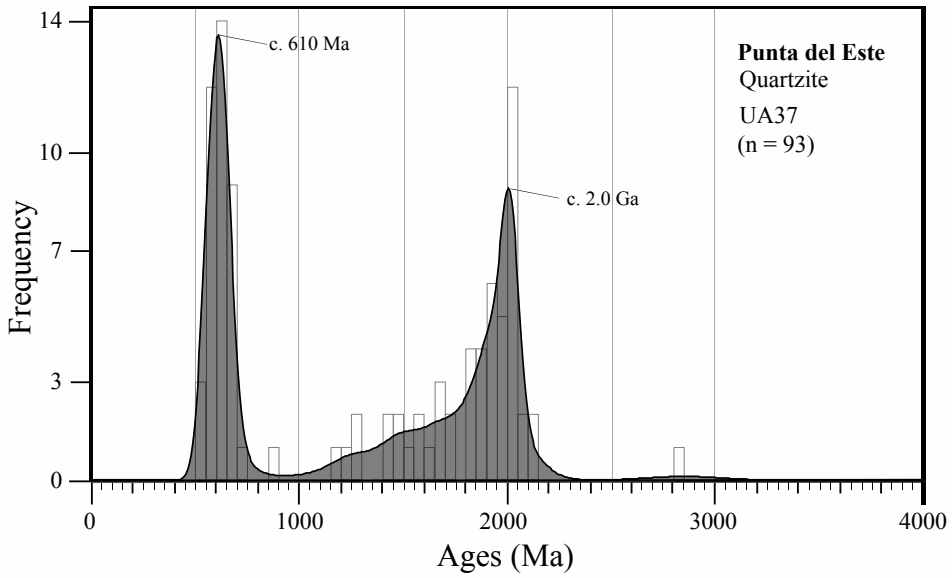

Fig 20: Kernel density plot and histogram for the ages of detrital zircons in UA37 quartzite. Significant peaks are recorded at c. 610 Ma and c. 2.0 Ga.

UB18 - Quartzite

UB18 is mainly composed of quartz, K-felspar, plagioclase, sillimanite, zoisite (Fig. 21a) and chlorite. The zoisite is interpreted to be derived from calcium-bearing plagioclase, while the chlorite is replacing biotite. The accessory minerals are zircon, rutile, apatite (Fig. 21b) and opaque minerals, representing c. 4% of the rock. The sample is interpreted as a metamorphosed sandstone.

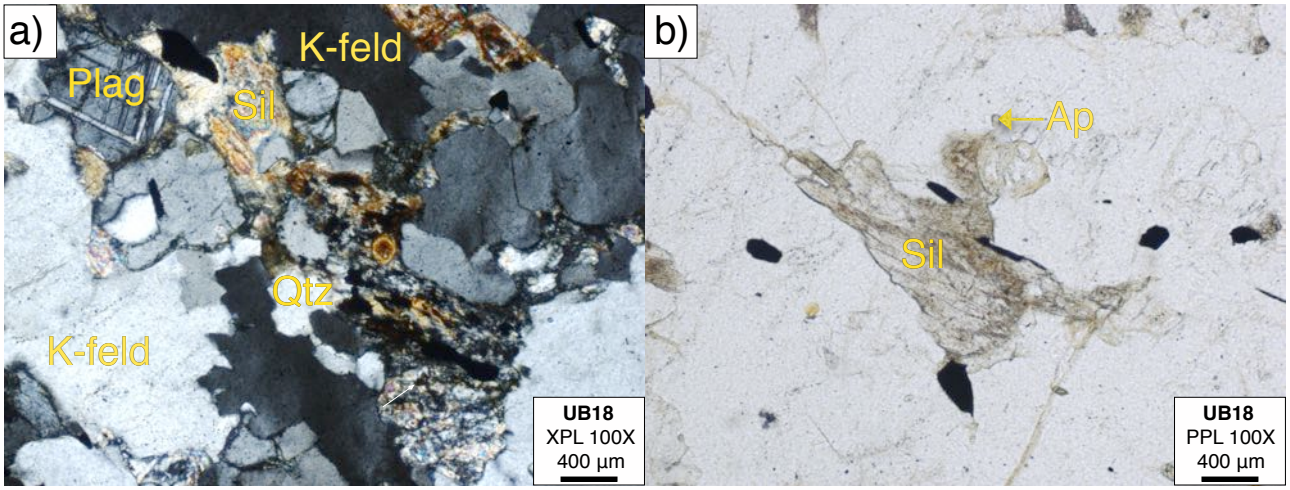

Fig. 21: a) Thin section UB18 at 100x magnification in crossed polarized light showing quartz, K-feldspar, plagioclase and sillimanite. b) UB18 at 100x magnification in plane polarized light showing sillimanite, apatite and opaque minerals.

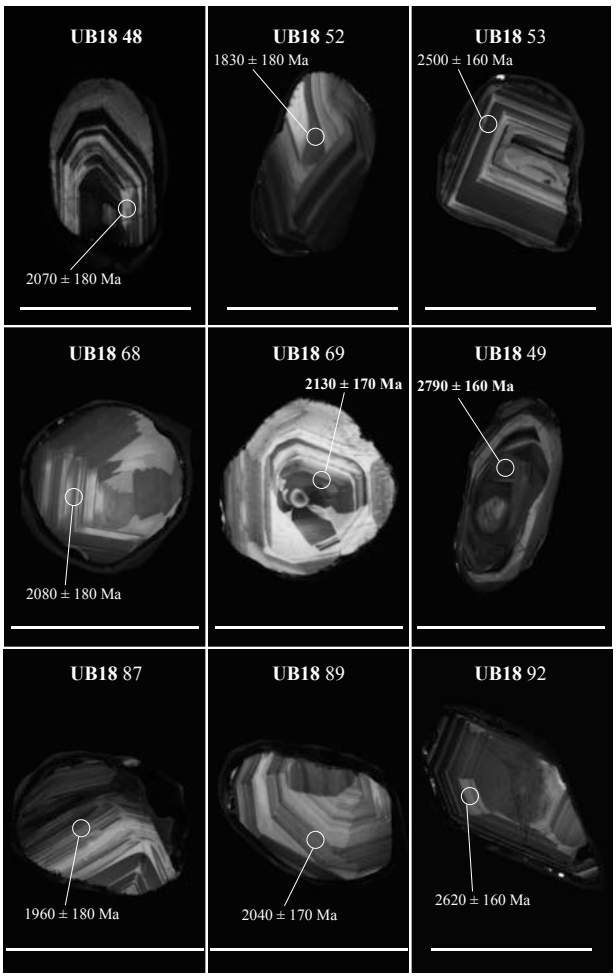

Fig. 22: CL images of typical zircons in UB18 quartzite. The circle marks the location of laser ablation spots in the zircon grains, scale bars are set to 100 *μm*.

The zircons in UB18 measure 50 to 100 *μm* in width, and 100 to 190 *μm* in length. The zircon grains are elongated with a mean aspect ratio of 1.9. A substantial number of the grains are subhedral, while some are rounded (UB18: 68 in Fig. 22). A small number of the zircon grains show fractures or inclusions. The majority of the zircon grains show oscillatory zoning. Some grains show a darker, less defined core and overgrowths towards the edges (UB18 69 in Fig. 22). In several grains, the complex zircon textures indicate multi-stage zircon growths or recrystallization.

Of the 150 analyzed grains in UB18, only 38 were less than ± 10% discordant. The $^{206}Pb/^{238}U$ or $^{207}Pb/^{206}Pb$ ages are distributed between 540 Ma and 2.15 Ga. One $^{207}Pb/^{206}Pb$ age is recorded at 2.85 Ga. Kernel density plot and histogram of the data is presented in Fig. 23 showing peaks at 1.92 Ga and 2.22 Ga, and two minor peaks at 1.35 Ga, and 2.65 Ga.

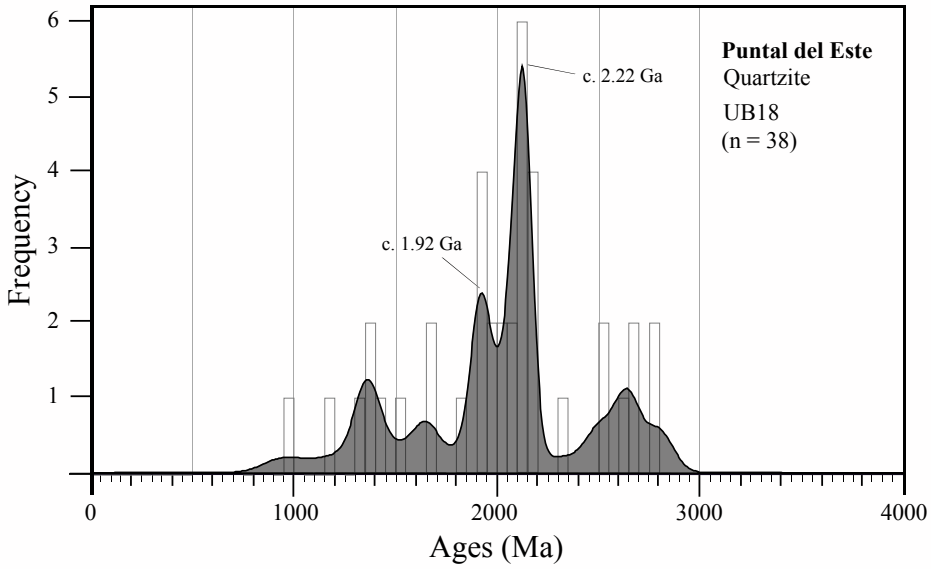

Fig 23: Kernel density plot and histogram of ages measured in the detrital zircons from UB18 quartzite. Main peaks are recorded at c. 1.92 Ga, and c. 2.22 Ga.

UA38 - Orthogneiss

The UA38 consists of K-feldspar and plagioclase, quartz, biotite and chlorite (Fig 24a, b). The accessory minerals observed in sample UA38 are zircon, apatite and opaque mineral, all estimated to c. 9%. The UA38 is classified as medium grained orthogneiss derived from a felsic plutonic protolith.

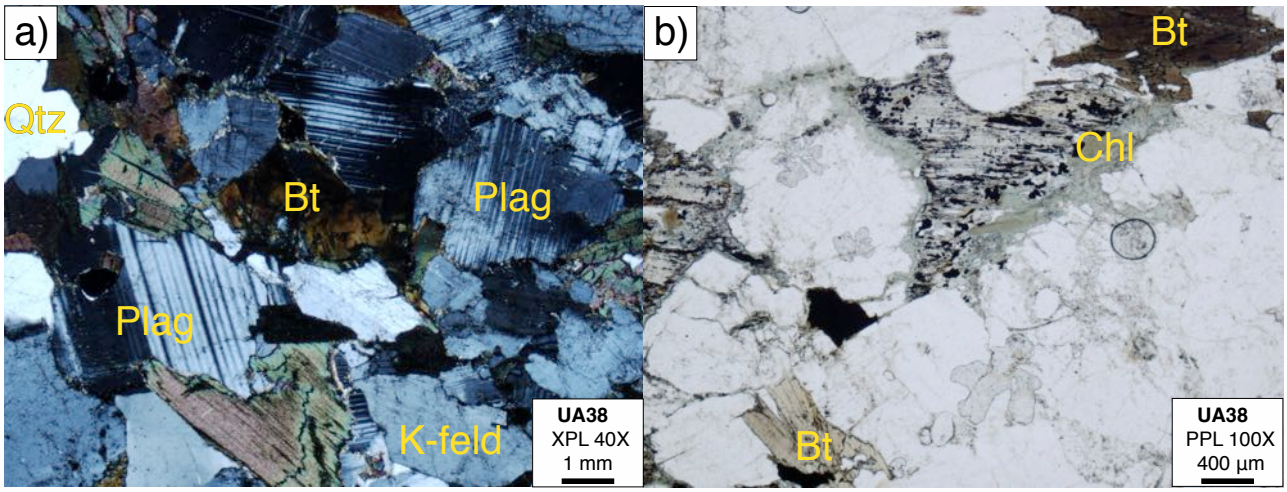

Fig. 24: a) Thin section UA38 at 40x magnification with crossed polarizers showing plagioclase, K-feldspar, biotite and quartz. b) Thin section UA38 at 100x magnification in plane polarized light showing chlorite and biotite.

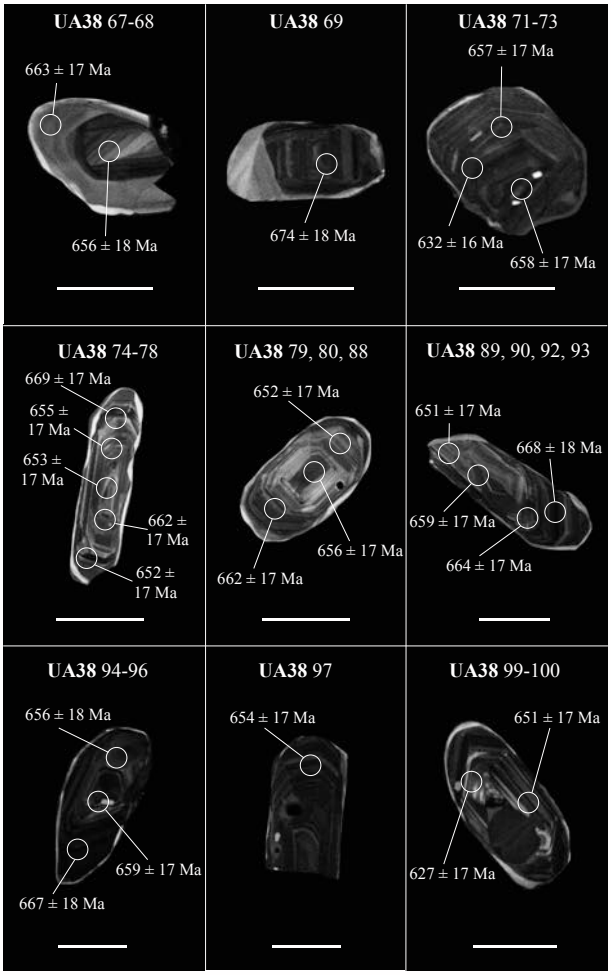

Fig. 25: CL images of typical zircons in the UA38 orthogneiss. The circles indicate the points of ablation at the zircons, and the scale bars show 100 *µm*.

The zircons from UA38 are 50 to 90 *µm* in width, and from 100 to 180 *µm* in length giving a mean aspect ratio of around 1.9. Most of the grains have rounded edges, and few of the grains show fractures or inclusions. Zircon UA38: 67-68 and 69 in Fig. 25 show thick bright CL rims around a darker oscillatory core, while most of the other grains show CL-bright and thin overgrowths around oscillatory zoned cores (see UA38: 99-100 in Fig. 25).

Of the 24 analyzes in UA38, 24 were less than ± 5% discordant. The data form one cluster in the concordia diagram centered at c. 656 Ma (Fig. 26).

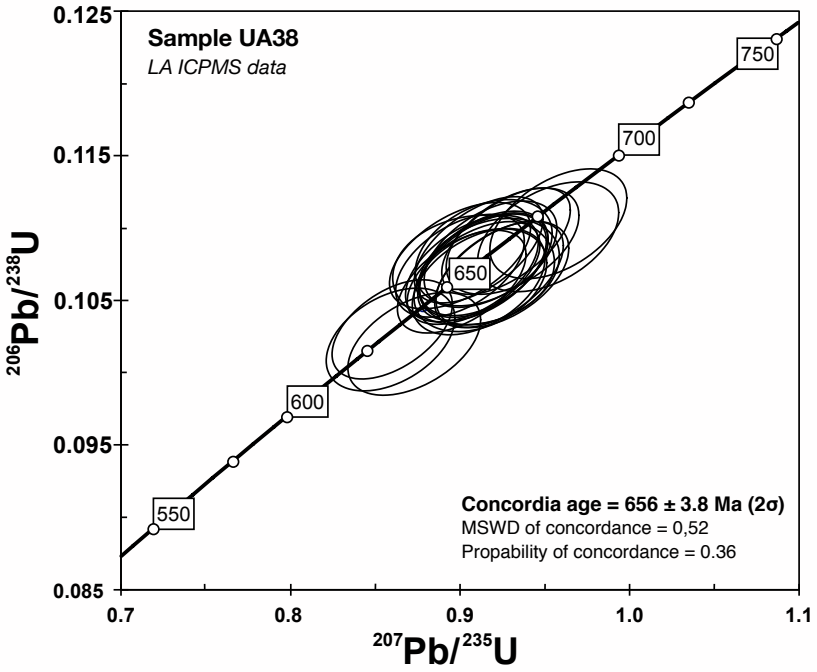

Fig 26: Concordia diagram for the data from zircons in UA38 orthogneiss clustering at c. 656 Ma.

UB2 – quartz-feldspathic gneiss

The sample UB2 is composed of K-feldspar, quartz, garnet, biotite, plagioclase and prismatic sillimanite. The accessory minerals are represented by zircon, rutile, apatite (Fig. 27b) and opaque mineral, together estimated to c. 4% in volume.

The rock is classified as quartz-feldspathic gneiss derived from a felsic magmatic protolith.

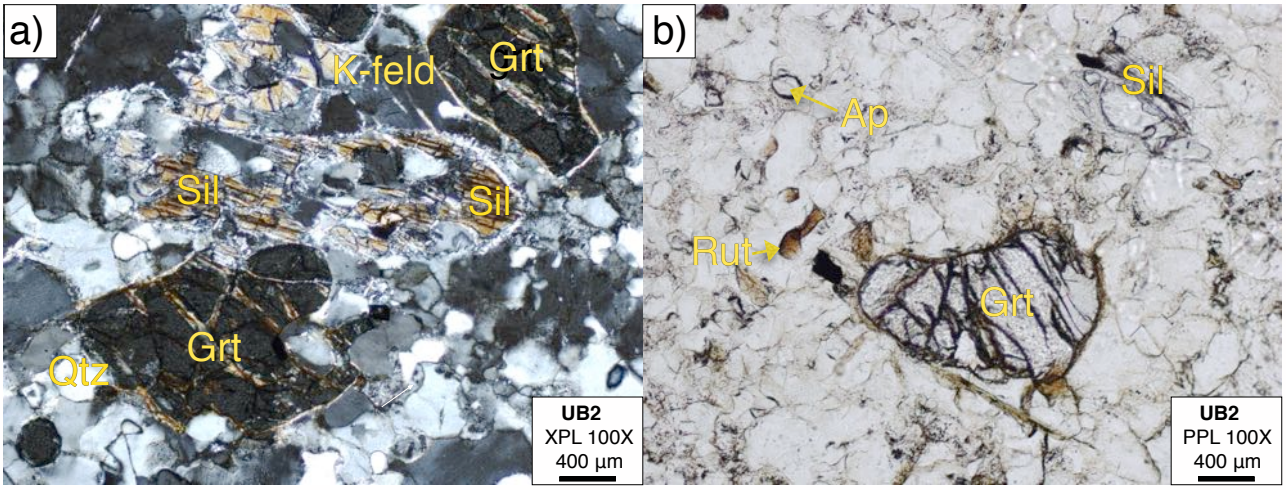

Fig. 27: a) Thin section UB2 at 100x magnification with crossed polarizers showing quartz, K-feldspar, garnet and sillimanite. b) UB2 at 100x magnification in plane polarized light showing garnet, sillimanite, apatite and rutile.

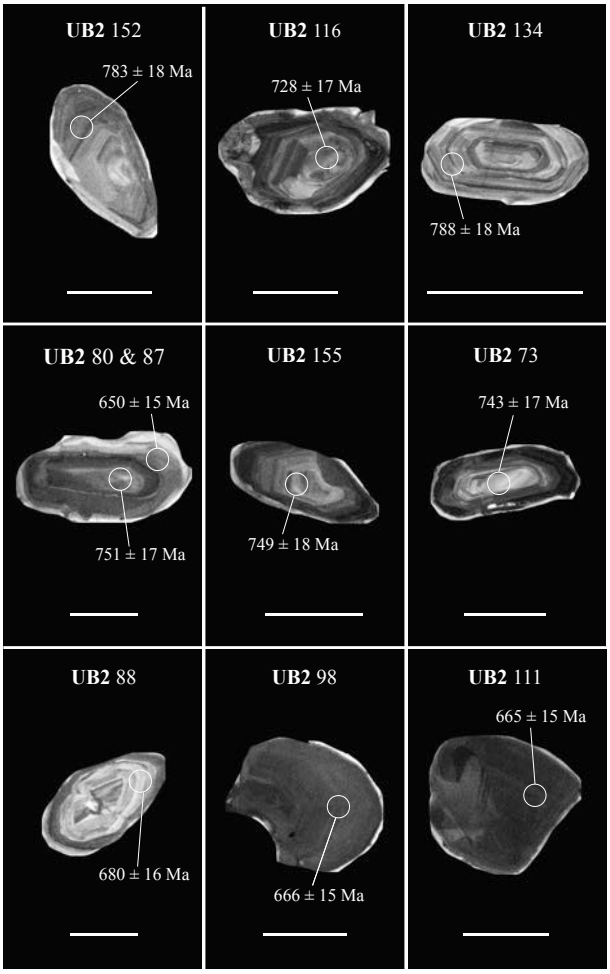

Fig. 28: CL images of zircons in the UB2 quartz-feldspatic gneiss. The scales bars show 100 μm and the circles display the laser ablation points.

The zircons in UB2 are c. 50 to 100 μm wide, and 100 to 150 μm long. The zircon grains are slightly elongated having a mean aspect ratio of 1.7. Most of the grains are subhedral or rounded. There is only small amount of inclusions and fractures in zircons from this sample.
In Fig. 28 the upper six zircon grains show oscillatory zoning, like most zircons in this sample, while in the last two grains the zoning is less pronounced and some parts show convoluted zoning. The complex zircon textures suggest partial or complete recrystallization of originally magmatic zircons with well-developed oscillatory zoning.

Of the 67 analyzed grains in UB2, 50 were less than ± 5% discordant. The main cluster of data lies between c. 650 Ma and 800 Ma (Fig. 29a) and ten ages are recoded between 1.0 Ga and 2.82 Ga (Fig. 29b).

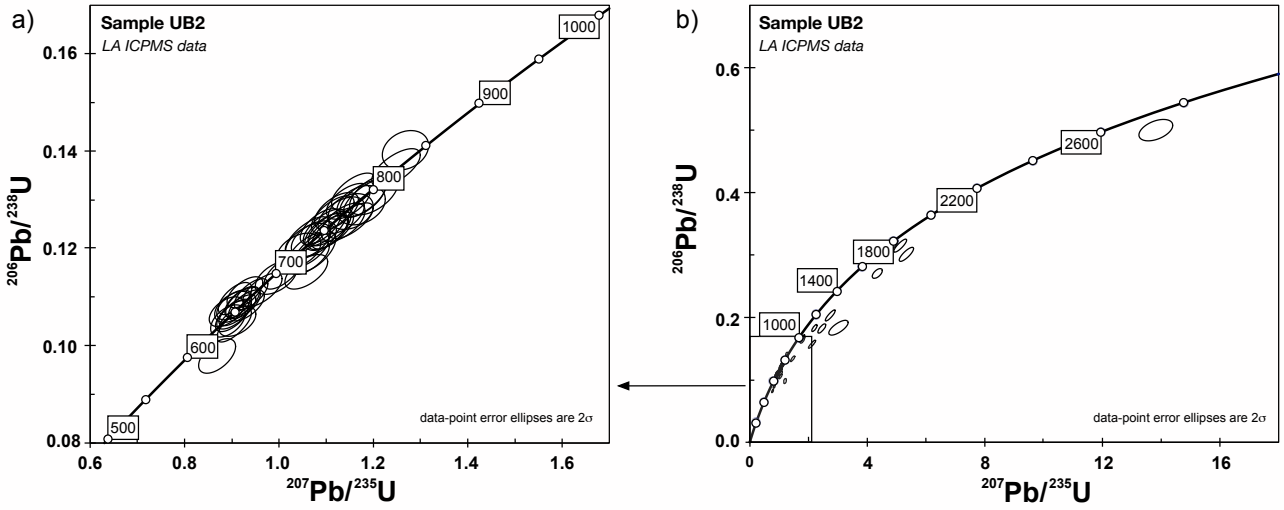

Fig 29: a) Concordia diagram for the zircons data in UB2 gneiss showing two main clusters of ages at c. 670 Ma and 770 Ma. **b)** All age data (< ± 5% discordant) obtained from the sample UB 2.

5.2 Samples from the Coastal Terrane, Kaoko Belt, Namibia

Two distinct lithologies from the Coastal Terrane have been studied. Samples NI123, NI130 and NK44 represent migmatitic gneisses, whereas sample NJ116 is a quartzite.
Thin section description, detrital zircon ages and zircon descriptions from these samples are presented in this part.

NI123 - Migmatitic gneiss

Medium grained migmatitic gneiss NI123 I consists of quartz, K-feldspar, elongated plagioclase crystals with visible polysynthetic twinning (Fig. 30a), moderately aligned biotite (also present as inclusions), small amount of muscovite, zircon and opaque mineral. Similar minerals are observed in sample NI123 II. This sample shows also the presence of garnet. Biotite intergrown with muscovite shows somehow stronger alignment (Fig. 30b) indicating well-developed foliation. The macroscopic appearance of the sample, as well as the K-feldspar-bearing mineral assemblage with high proportion of biotite suggest a high temperature metamorphism of a metasedimentary protolith.

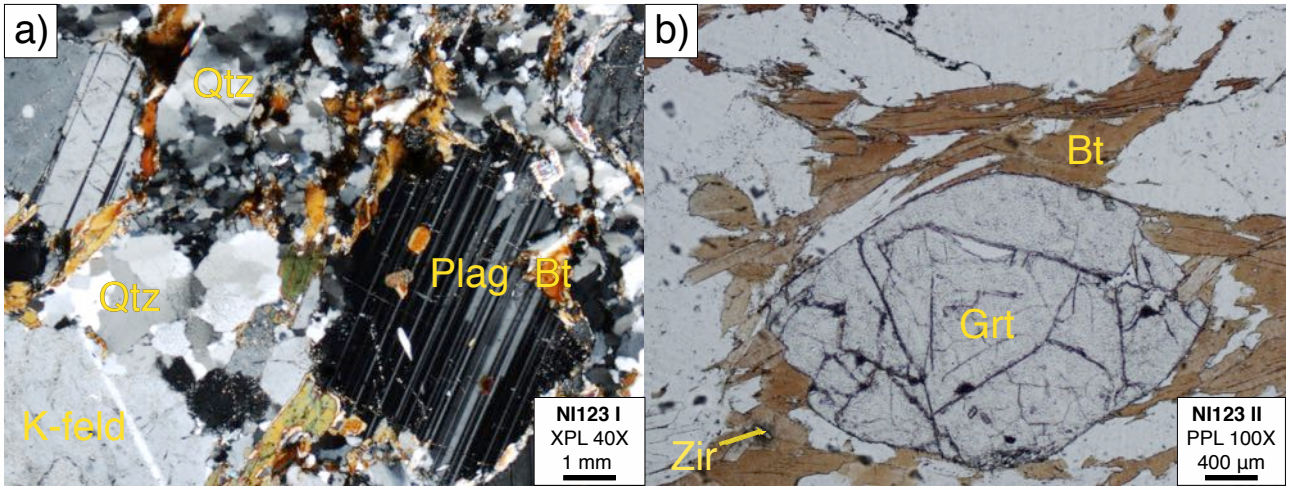

Fig. 30: Photomicrograph of high-grade metasediments from the Coastal Terrane. a) Thin section NI123 I at 40x magnification in crossed polarizers showing quartz, K-feldspar and plagioclase with inclusions of biotite. b) Thin section NI123 II at 100x magnification in plane polarized light showing a fractured garnet with aligned biotite and a zircon with a halo.

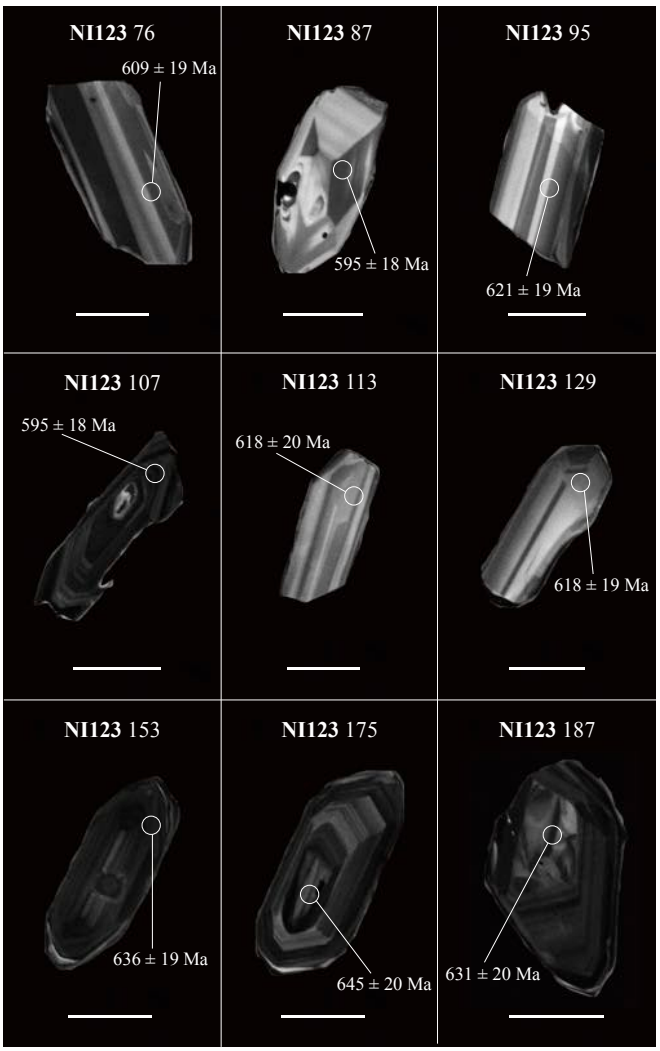

Fig. 31: Cathodoluminescence images of characteristic zircons in NI123 migmatitic gneiss. The circles show the laser ablation points on the zircons, and the scale bars show 100 *μm*.

The zircons measure 50 to 120 *μm* in width and 110 to 250 *μm* in length and the grains are elongated with a mean aspect ratio of 2.3. The majority of the zircon grains have rounded edges, while some have well preserved prismatic crystal shapes. A minor number of the grains has fractures and inclusions. The cathodoluminescence study revealed oscillatory zoned grains, sometimes with poorly defined core. Approximately 20% of the studied grains have shown only weak zoning (see grain no. 153 in Fig. 31).

Of the 98 analyzed grains in NI123, 88 were less than ± 10% discordant. The $^{206}Pb/^{238}U$ ages are distributed between 530 Ma and 680 Ma. Three grains were older than 1.0 Ga and gave $^{206}Pb/^{207}Pb$ ages of 1.2 Ga, 1.48 Ga and 2.0 Ga. Kernel density plot and histogram of the ages is presented in Fig. 32 showing a single peak at c. 620 Ma.

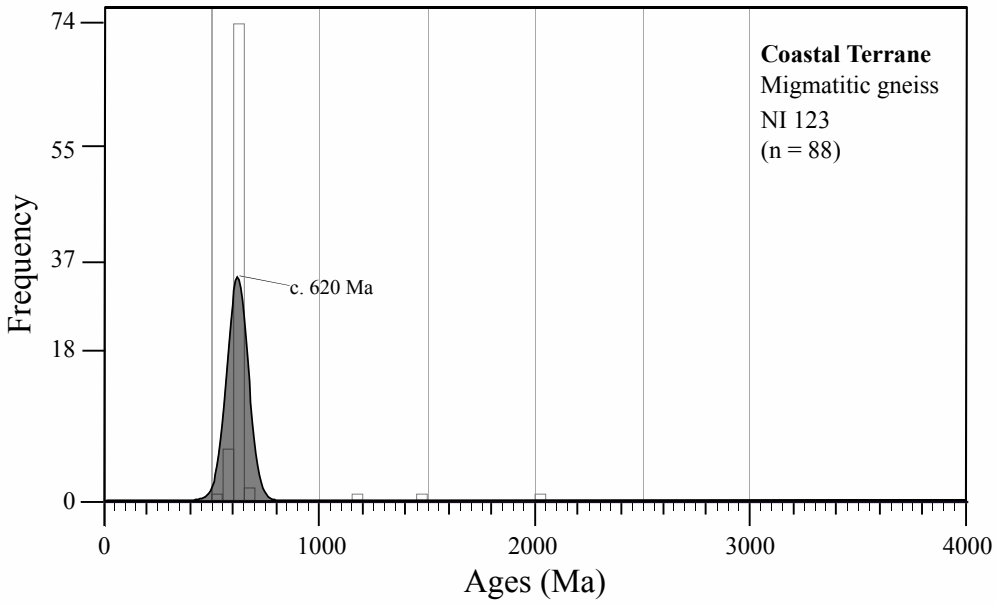

Fig 32: Kernel density plot and histogram of the zircon ages in migmatitic gneiss NI123. The data show a single peak at c. 620 Ma and three single data at c. 1.2 Ga, c. 1.45 Ga and c. 2.0 Ga.

NI130 - Migmatitic gneiss

Sample NI130 is a migmatitic gneiss similar to the sample NI123. The mineral assemblage is represented by plagioclase, K-feldspar, chlorite (Fig. 33a) and quartz together with biotite (Fig. 33b). Zircon, apatite and opaque minerals are estimated to c. 7%. When compared with NI123, this sample contains higher amount of plagioclase and quartz, while muscovite and garnet are not present. Like in the sample NI123, the macroscopic appearance and the mineral assemblage in NI130 indicate high-grade metamorphism of a clastic sedimentary protolith.

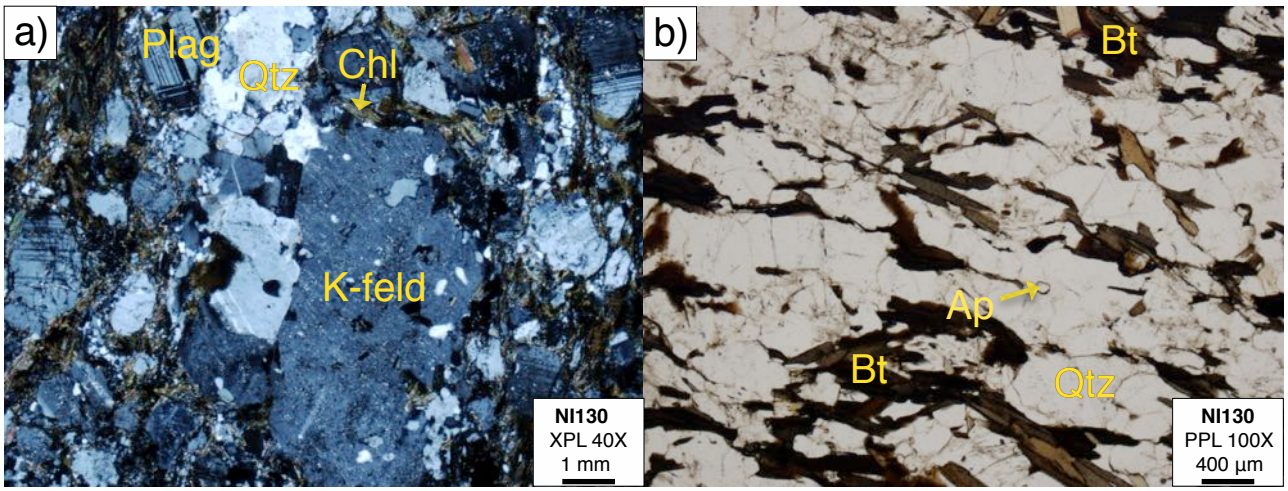

Fig. 33: Photomicrograph of high-grade metasediments from the Coastal Terrane. a) Thin section of migmatitic gneiss in NI130 at 40x magnification in crossed polarized light showing inclusions of quartz in K-Feldspar and chlorite. b) Thin section NI130 at 100x magnification in plane polarized light showing apatite and aligned biotite with quartz.

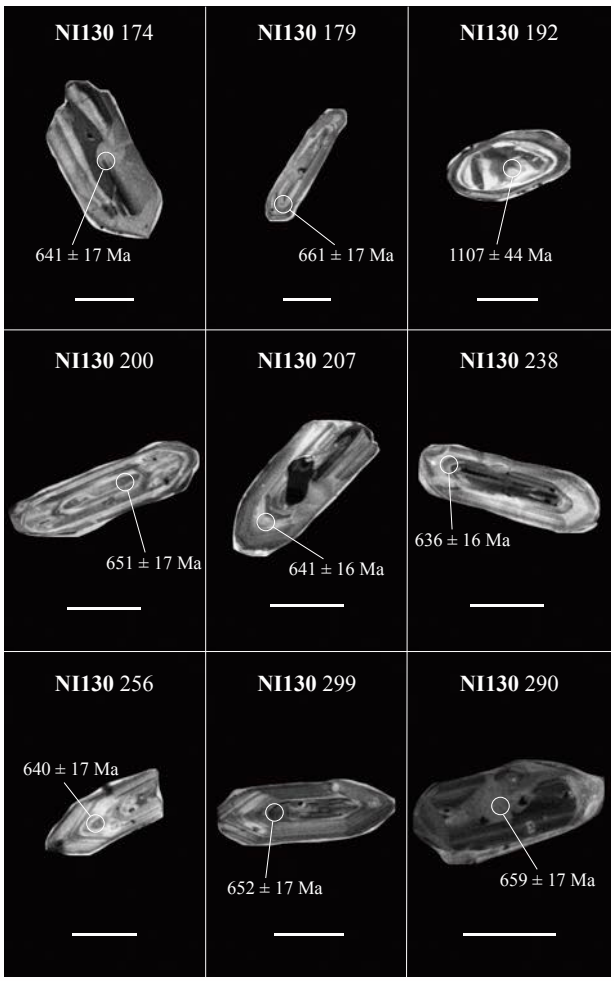

Fig. 34: Cathodoluminescence images of characteristic zircons in NI130 migmatitic gneiss. The circle indicates where the zircon grain has been ablated, the scales bars are set to 100 microns.

The zircons in NI130 measure from 30 to 100 μm in width, and 100 to 230 μm in length. The zircon grains are elongated with a mean aspect ratio of 2.5.

Most of the zircon grains are subhedral, while some are anhedral. Approximately 10% of the grains show fractures and 10% of the grains show inclusions.

The majority of the zircon grains show thin and bright rims and some degree of oscillatory zoning with no core, some show a darker core and some show very weak zoning.

Of the 98 analyzed grains in NI130, 83 were less than ± 10% discordant. The $^{206}Pb/^{238}U$ age range is between 540 Ma and 890 Ma. One single grain was older than 1.0 Ga and gave an $^{207}Pb/^{206}Pb$ age of 1.09 Ga. Kernel density plot and histogram are presented in Fig. 35 showing a single peak at c. 650 Ma.

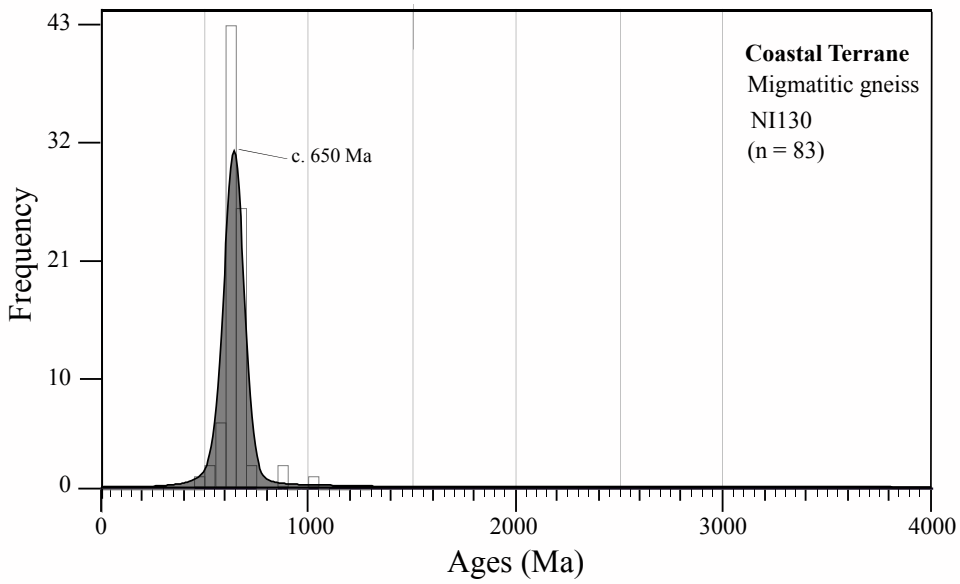

Fig 35: Kernel density plot and histogram for the zircons in migmatitic gneiss NI130. One peak at c. 650 Ma is recorded within the range of the data between c. 540Ma and 890 Ma, while one significantly older grain plot at c. 1.09 Ga.

NJ116 - Quartzite

Sample NJ116 consists mostly of quartz (Fig. 36a) with minor amounts of K-feldspar, garnet, muscovite and biotite. No plagioclase has been observed. Accessory minerals including zircon, apatite and opaque mineral are estimated to c. 6%. The quartz content in NJ116 is estimated to 90%. The mineral assemblage indicates metamorphism of a quartz rich sedimentary protolith.

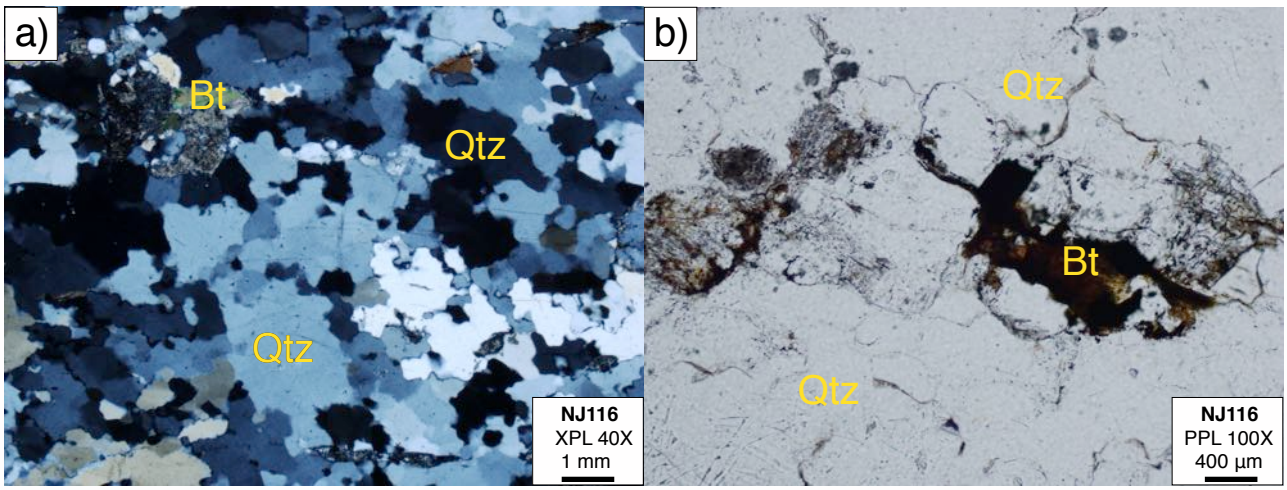

Fig. 36: Photomicrograph of NJ116 quartzite from the Coastal Terrane. a) NJ116 at 40x magnification taken with crossed polarizers showing quartz and biotite. b) NJ116 at 100x magnification in plane-polarized light showing quartz and biotite.

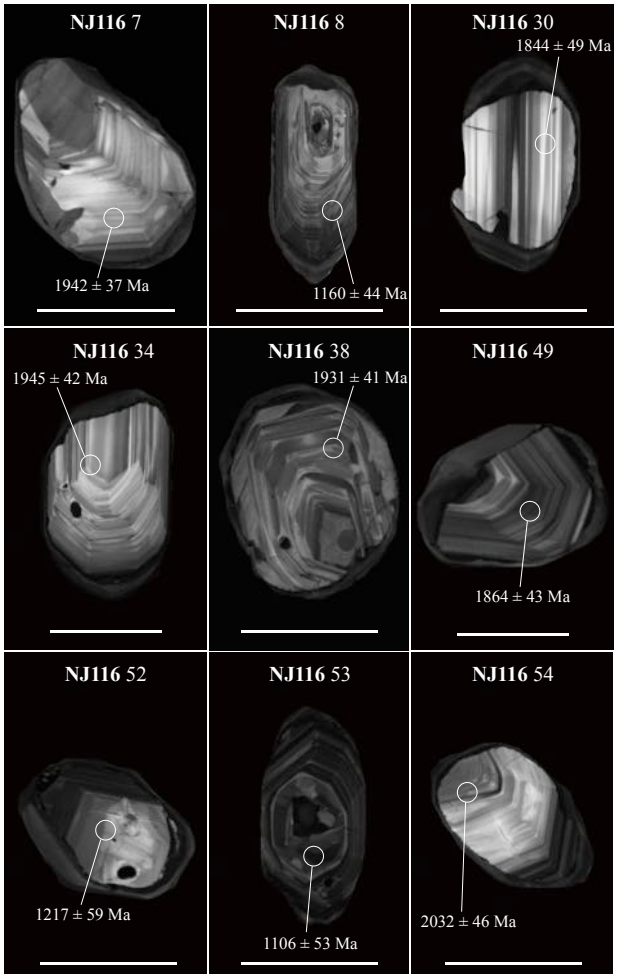

Fig. 37: Cathodoluminescence images of characteristic zircons in NJ116 quartzite. The circles indicate the zircons laser ablation points, and the scales bars represent 100 microns.

The zircons from NJ116 measure from 70 to 100 μm in width, and 100 to 210 μm in length. They are elongated with an average aspect ration ratio of 1.8. Most of the zircon grains have rounded edges, while a minor number preserved original crystal shapes. A minor amount of zircons show fractures or inclusions. Most of the zircon grains show oscillatory zoned parts overgrown by featureless rims. Some grains (See NJ116: 53 in Fig. 37) show a darker core, while a low number of zircons show only weak zoning.

In total 98 grains were analyzed in NJ116, where 75 grains were less than ± 10% discordant. The $^{206}Pb/^{238}U$ or $^{207}Pb/^{206}Pb$ ages fall mostly into a broad interval between 760 Ma and 2.05 Ga. Seven grains gave $^{207}Pb/^{206}Pb$ ages between 2.1 Ga and 2.9 Ga. Density plot and histogram of the age data from this sample are presented in Fig. 38, showing major peaks at 930 Ma, 1.32 Ga, 1.84 Ga and 1.95 Ga.

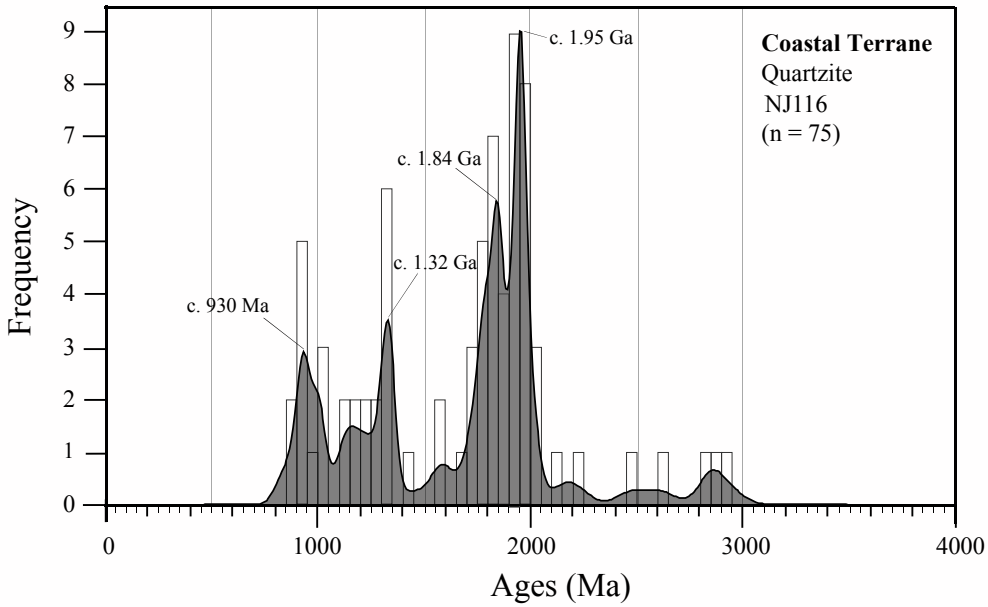

Fig 38: Kernel density plot and histogram for the detrital zircons in NJ116 quartzite. Four major peaks are recorded at 930 Ma, 1.32 Ga, 1.84 Ga and 1.95 Ga.

NK44 - Migmatitic gneiss

Migmatitic gneiss NK44 shows the mineral assemblage quartz (100-200 *μm)*, plagioclase, K-feldspar, chlorite and biotite (Fig. 39a). The accessory minerals observed are zircon, apatite and opaque mineral, all estimated to c. 5%. NK44, like the NI130, shows muscovite-free mineral assemblage and high proportion of biotite indicative of high-grade metamorphism of a rock with sedimentary protolith.

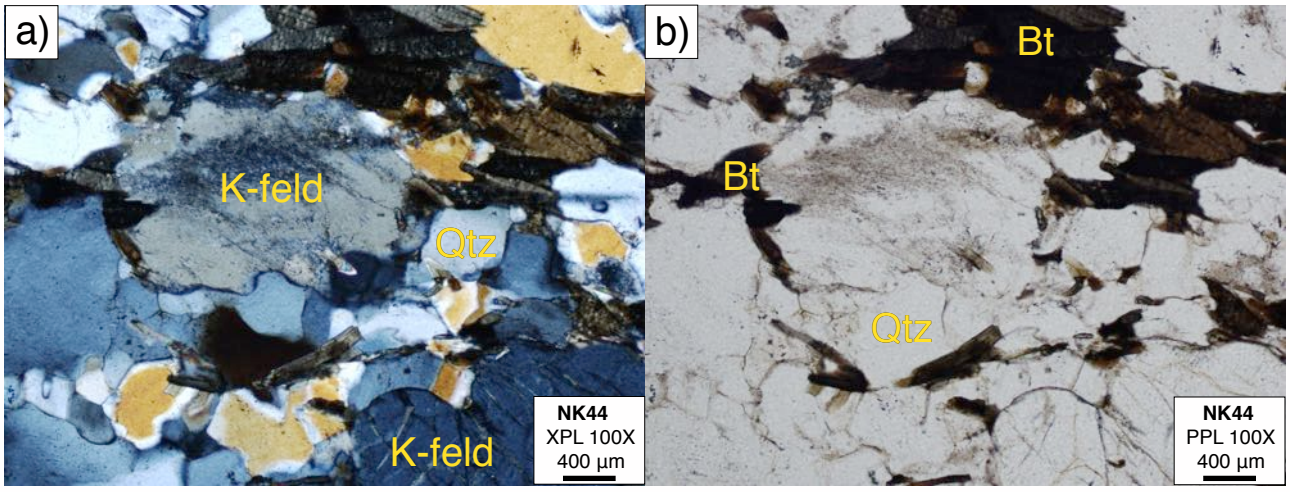

Fig. 39: Photograph of migmatitic gneiss from the Coastal Terrane. a) Thin section of migmatitic gneiss in NK44 at 100x magnification with crossed polarizers showing quartz, K-feldspar, and biotite. b) NK44 at 100x magnification in plane-polarized light showing quartz, biotite and opaque minerals.

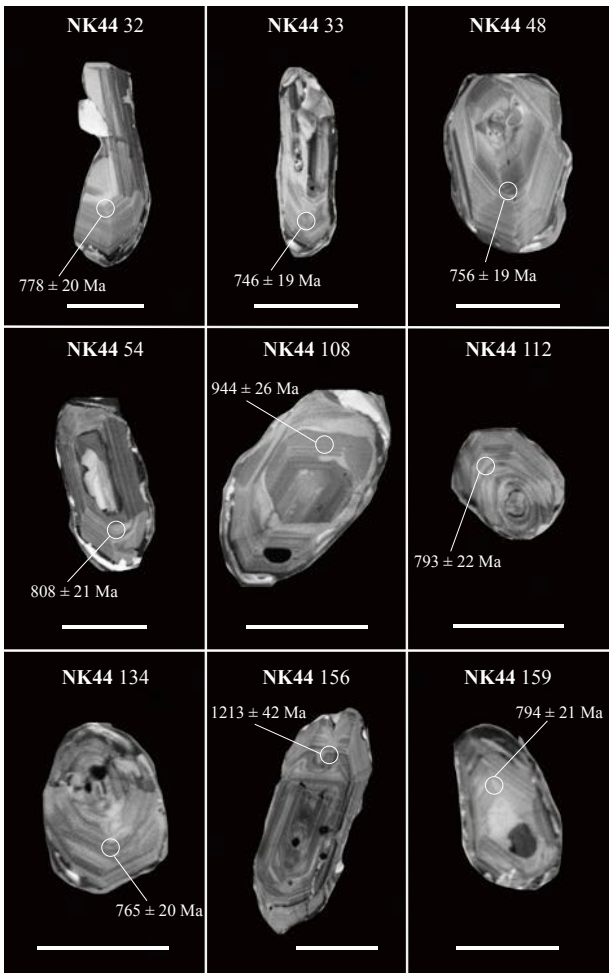

Fig. 40: Cathodoluminescence images of characteristic zircons in NK44 migmatitic gneiss. The circles show where the zircon has been ablated, and the scales are 100 *μm*.

The zircons from NK44 are about 50 to 130 *μm* in width, and from 90 to 220 *μm* in length. The zircon grains are elongated with a mean aspect ratio of 1.9.

Most of the zircons have rounded edges, while a minor number still preserves crystal faces (NK44: 32 in Fig. 40). Around 20% of the grains show minor fractures and several of the grains show inclusions. The majority of the zircon grains show oscillatory zoning with a darker, poorly defined cores, some show non-concentric oscillatory zoning and minor number shows no zoning.

Of the 112 analyzed grains in NK44, 99 were less than ± 10% discordant. The $^{206}Pb/^{238}U$ and $^{207}Pb/^{206}Pb$ data plot between 690 Ma and 1.96 Ga. Six grains gave $^{207}Pb/^{206}Pb$ ages between 2.0 and 3.05 Ga. Kernel density plot and histogram are presented in Fig. 41 showing a major peak at c. 760 Ma and a minor peak at c. 1.9 Ga.

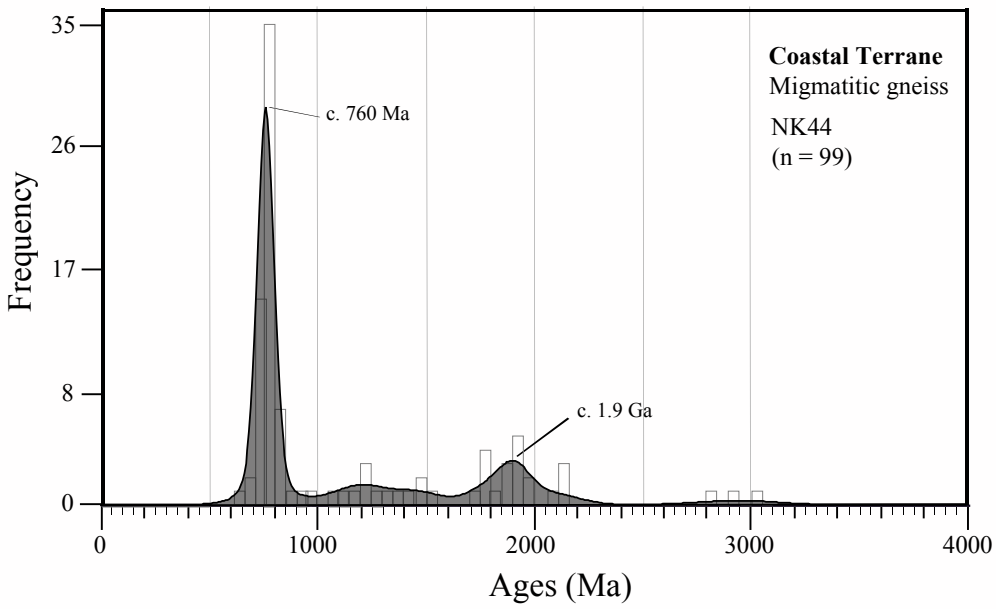

Fig 41: Kernel density plot and histogram for the ages of detrital zircons in NK44 migmatitic gneiss. The distribution of ages shows one peak at c. 760 Ma and a minor peak at c. 1.9 Ga.

6 Discussion

In the discussion the isotopic ages from the samples of this study will be compared and interpreted with regard to the protolith ages reported from the Coastal Terrane - Punta del Este, Rio de la Plata, Congo Craton (Fig. 42) and with respect to the age of the M1 Pan-African-Brasiliano metamorphic event.

6.1 Source regions

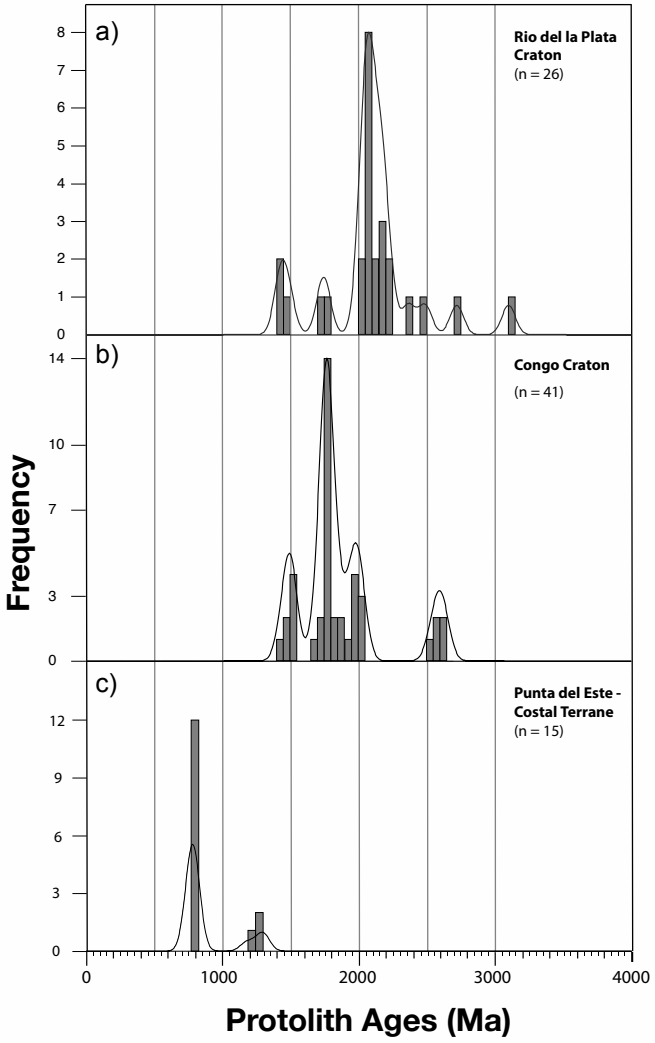

Fig. 42: A compilation of zircon protolith ages from: a) The Rio de la Plata Craton. b) The Congo Craton. c) The Punta del Este - Coastal Terrane. This is a compilation from available protolith zircon data in these units, a more detailed description can be found in Appendix A. The figure is made with DensityPlotter 4.4 as a probability density plot and the width of columns in the histograms is set to 50 Ma.

Fig. 42 summarizes the published U-Pb and Pb-Pb protolith zircon ages of magmatic rocks in tectonic units, that could have been the potential source regions of the protoliths of metasedimentary rocks analyzed in this study.

The protolith ages from the Piedra Alta and Nico Perez terranes of the Rio de la Plata Craton (Fig. 42a) give main clusters at c. 2.22 Ga (Hartman et al., 2001; Peel & Preciozzi; 2006), c. 2.06 Ga (Santos et al., 2003; Hartman et al., 2000, 2008b) and c. 1.43 Ga (Oyhantcabal et al., 2005a; Gaucher et al., 2010).

The protolith ages recognized in the Congo Craton (Fig. 42b) can be divided into three major groups at c. 1.96 Ga (Seth et al., 1998; Kröner et al., 2004; Luft et al., 2010), c. 1.75 Ga (Kröner et al., 2004, 2010; Luft et al., 2010) and c. 1.52 Ga (Seth et al., 1998; Kröner et al., 2004; Luft et al., 2010).

Potolith ages found in the Rio de la Plata and Congo Craton overlap at c. 2.05 Ga (Kröner et al., 2004; Peel and Preciozzi., 2006; Hartman et al., 2008b), at c. 1.7-1.8 Ga (Sánchez-Bettucci et al., 2004; Kroner et al. 2004, 2010; Mallmann et al. 2007; Luft et al. 2010) and at c. 1.4-1.5 Ga (B. Seth et al., 1998; Kröner et al., 2004; Oyhantcabal et al., 2005a; Gaucher et al., 2010; Luft et al., 2011), whereas the ages of c. 2.20 Ga seem to be unique for the western part of the Rio de la Plata Craton known as the Piedra Alta Terrane. Common ages in the Nico Perez Terrane of the Rio de la Plata Craton and in the western part of the Congo Craton suggest that these two basement units could have been a part of one cratonic block prior to the Neoproterozoic rifting.

For the Coastal Terrane and Punta del Este (Fig. 42c) the protolith ages from mafic granulites and felsic orthogneisses show one prominent peak at c. 780 Ma (Konopásek et al., 2008; Oyhantcabal et al., 2009a; Lenz et al., 2011) and several minor data at c. 1.28 Ga representing older cores of protolith zircons (Lenz et al., 2011).

6.2 Magmatism in the Punta del Este Terrane

Two samples (UA38 and UB2) interpreted in the field as representing the products of the Neoproterozic magmatism have been analyzed in this study. The cathodoluminescence images of zircons from sample UA38 mostly show oscillatory zoning and the data show a homogeneous group of isotopic ages (Fig. 43).

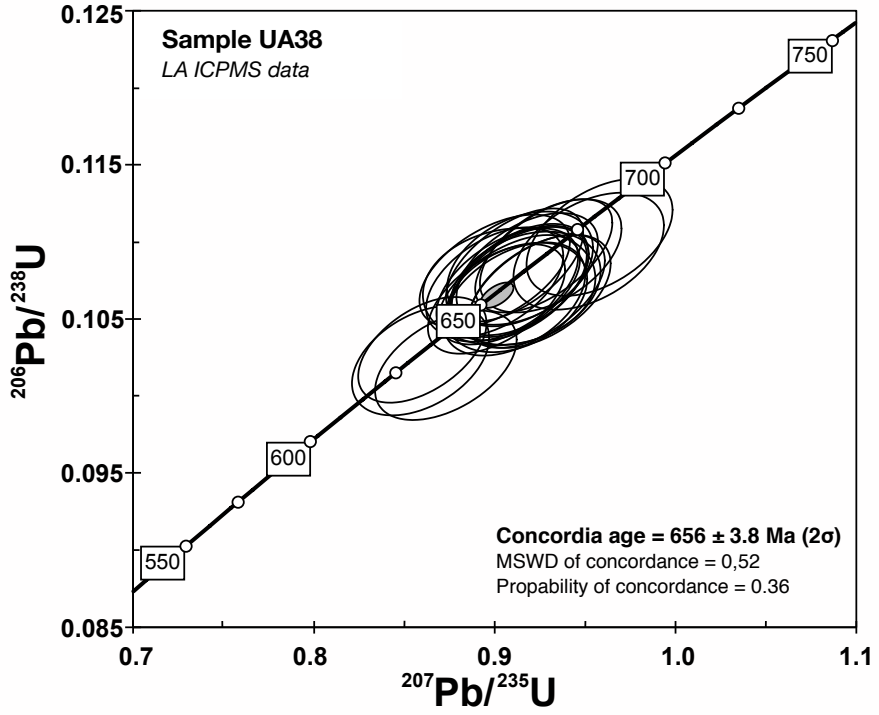

Fig. 43: U-Pb isotopic age determination for sample UA38.

Sample UA38 shows one homogeneous cluster of data in the concordia diagram (Fig. 43) and these data provided calculated concordia age of 656 ± 4 Ma (2σ). The zircons from this sample show oscillatory zoning and the calculated concordia age can be interpreted as an age of its granitoid protolith. The protolith age of 656 ± 4 Ma suggests that the emplacement took place during the peak of the metamorphic event at c. 650 Ma in the Punta del Este Terrane (Oyhantcabal et al., 2009a; Lenz et al., 2011).

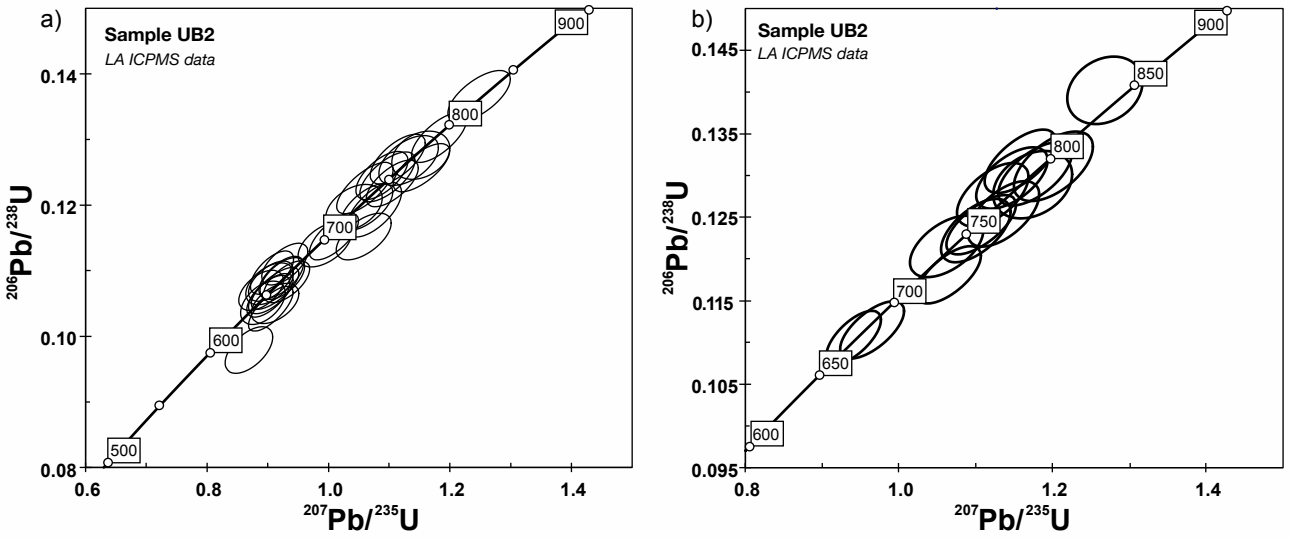

Fig. 44: a) U-Pb isotopic data from those parts in sample UB2 that show convolute zoning or no zoning patterns. b) U-Pb isotopic data from oscillatory zoned parts of the zircons in sample UB2.

The zircons in sample UB2 have been divided into two groups based on their internal structures from the cathodoluminescence pictures. The data illustrated in Fig. 44a were obtained in those parts of zircons showing convolute or no zoning patterns, while the data in Fig. 44b come from the oscillatory zoned zircons.

Zircons with convolute or no zoning (Fig 44a) show a scatter of ages between c. 600 and 820 Ma with a prominent cluster of data at c. 650 Ma. Data from oscillatory zoned parts show very similar spread of ages, but the majority of the data is concentrated between c. 750 and 800 Ma. Unfortunately, no concordia age could have been calculated for any of these groups. In accord with the interpretation of the data from similar sample dated in this region (see sample UY 10-05 of Oyhantcabal et al., 2009a), the oscillatory zoned parts are interpreted as representing the original igneous protolith zircons of the sample and their ages correspond to the timing of magmatic event reported in the Punta del Este Terrane by other authors (Oyhantcabal et al., 2009a; Lenz et al., 2011, 2013). These protolith zircons (c. 800-750 Ma old) were probably recrystallized to various extent during the subsequent granulite-facies metamorphism at c. 650 Ma, which is shown by the group of data around this age obtained from zircons with convolute or no zoning patterns (Fig. 44a).The data scattering in the sample UB2 shows some of the challenges in interpreting zircon data in high-grade metamorphic rocks, as the zircons show complex textures and underwent various degrees of recrystallization (cf. Möller et al., 2002; Lenz et al., 2011; Konopásek et al., 2014b).

6.3 Sedimentation in the Punta del Este Terrane

The zircon data from the Punta del Este Terrane metasediments are illustrated for UA37 in Fig. 45 and for UB18 in Fig. 46. To identify the potential source regions for the dated detrital zircons, the previously reported protolith ages from the potential source regions are displayed on top of the diagrams, and the Brasiliano-Pan African rifting-related magmatism (c. 800-750 Ma) and granulite-facies metamorphism in the Punta del Este-Coastal Terrane (c. 650-630 Ma) are labeled with colors.

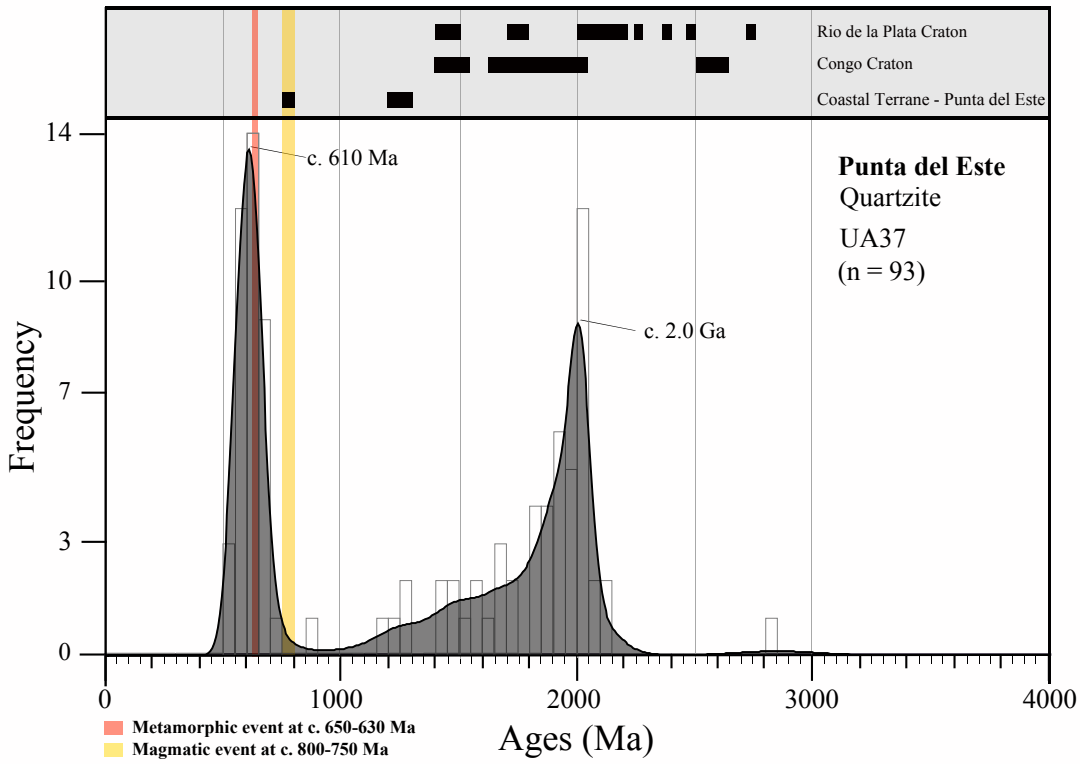

Fig. 45: Zircon ages from sample UA37, representing quartzite from the Punta del Este Terrane. The zircon data give peaks at c. 610 Ma, and c. 2.0 Ga with a subordinate number of data in between and older.

The zircons in the UA37 quartzite show oscillatory zoning in the center and overgrowths or zones of recrystallization with a different shade toward the ages, that cut across the oscillatory zoned parts of the crystals. Analyses of these outer zones provided ages that cluster around 610 Ma (Fig. 45). Although this peak does not exactly match the metamorphic event reported from the Punta del Este terrane at c. 650-630 Ma (Oyhantcabal et al., 2009a; Lenz et al., 2011), textures indicate that these data represent zircons recrystallized during the high grade metamorphic event.

The c. 2.0 Ga peak (Fig. 45) represent the maximum sedimentary age in the sample UA37, and match the reported c. 2.06 Ga protolith ages in the Rio de la Plata Craton (Santos et al., 2003; Hartman et al., 2000, 2008b).

The oldest single age (c. 2.8 Ga) in UA37 were never reported from the pre-Neoproterozoic basement of the Dom Feliciano belt.

Of the subpopulations in sample UA37 (Fig. 45), the c. 1.7-1.8 Ga ages correspond with the 1.7-1.8 Ga protolith ages (Sánchez-Bettucci et al., 2004; Mallmann et al., 2007), also the zircons dated at c. 1.45 match the 1.4-1.5 Ga protolith ages from the Rio de la Plata Craton (Oyhantcabal et al., 2005a; Gaucher et al., 2010), while the c. 1.25 Ga zircons correspond with the 1.28 Ga xenocrysts in the c. 800 Ma metaigneous rocks from the Punta del Este Terrane (Lenz et al., 2011).

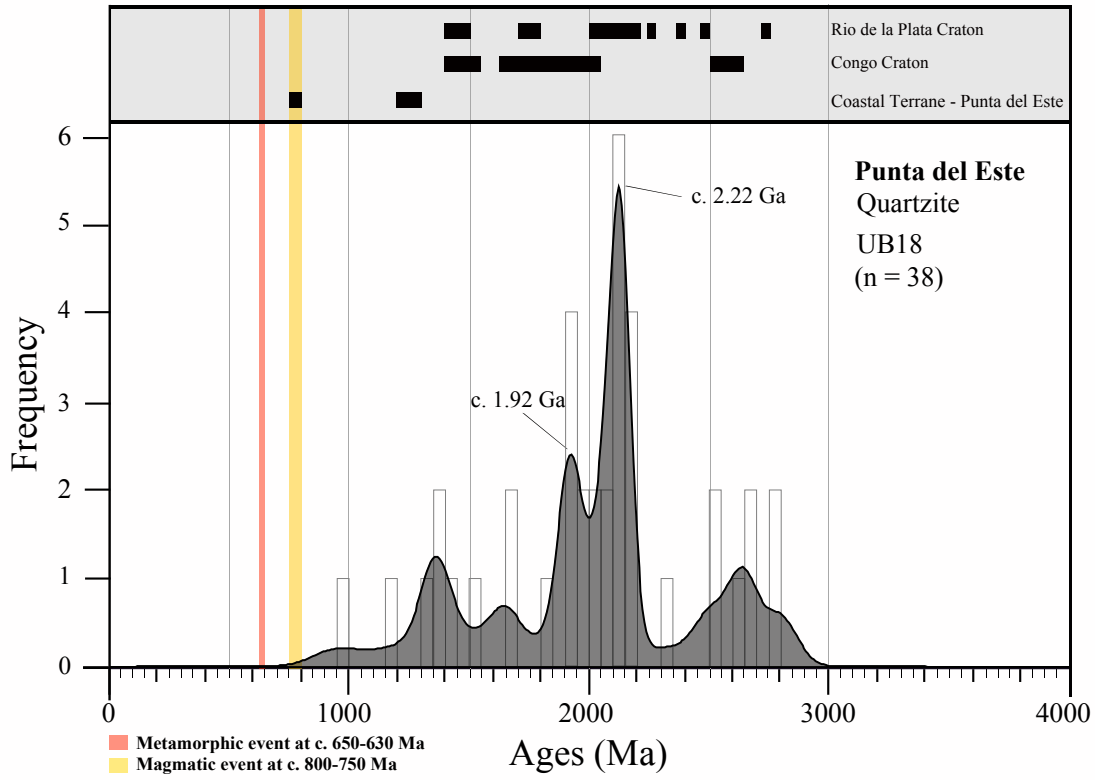

Fig. 46: Zircon data from sample UB18 quartzite from the Punta del Este Terrane. The zircon data give peaks at c. 1.92 Ga, and c. 2.22Ga, with a distribution of low frequent ages from c. 1.0 - 2.9 Ga.

The CL images of zircons from sample UB18 show presence of oscillatory zoning, sometimes with thin CL-bright rims around. Analyses of the inner parts of the zircons gave a continuous range of isotopic ages from c. 1.0 - 2.9 Ga, with the two peaks at c. 1.92 Ga and c. 2.22 Ga.

Identical ages of the c. 2.22 Ga have been reported as protolith ages of the Piedra Alta Terrane of Rio de la Plata Craton (Hartman et al., 2001; Peel & Preciozzi, 2006).

The c. 1.92 Ga peak, represent the maximum sedimentary age of sample UB18, offset by c. 140 Ma from the c. 2.06 Ga peak from the Rio de la Plata Craton (Santos et al., 2003; Hartman et al., 2000, 2008b), but corresponds well with protolith ages of c. 1.96 Ga from the Congo Craton (Seth et al., 1998; Kröner et al., 2004; Luft et al., 2010).

The subpopulation in Fig. 46 at c. 1.34 Ga peak may correspond to xenocrystic ages of c. 1.28 Ga from the Coastal Terrane - Punta del Este metaigneous rocks (Lenz et al., 2011).

The number of detrital zircons (n = 38) in sample UB18 are below the limit of statistical significance of 50 zircons in provenance studies suggested by Morton et al. (1996), and this has been take into consideration in the general interpretation part of the discussion.

6.4 Sedimentation in the Coastal Terrane

The zircon data from the metasedimentary samples in Coastal Terrane are illustrated for NI123 (Fig. 47), NI130 (Fig. 48), NK44 (Fig. 49) and NJ116 (Fig. 50).

Potential source regions are labeled on top of the diagrams, and the rifting-related Neoproterozoic (c. 800-750 Ma) magmatic event and the granulite-facies metamorphism (c. 650-630 Ma) in the Coastal Terrane - Punta del Este are marked with colors in the plots.

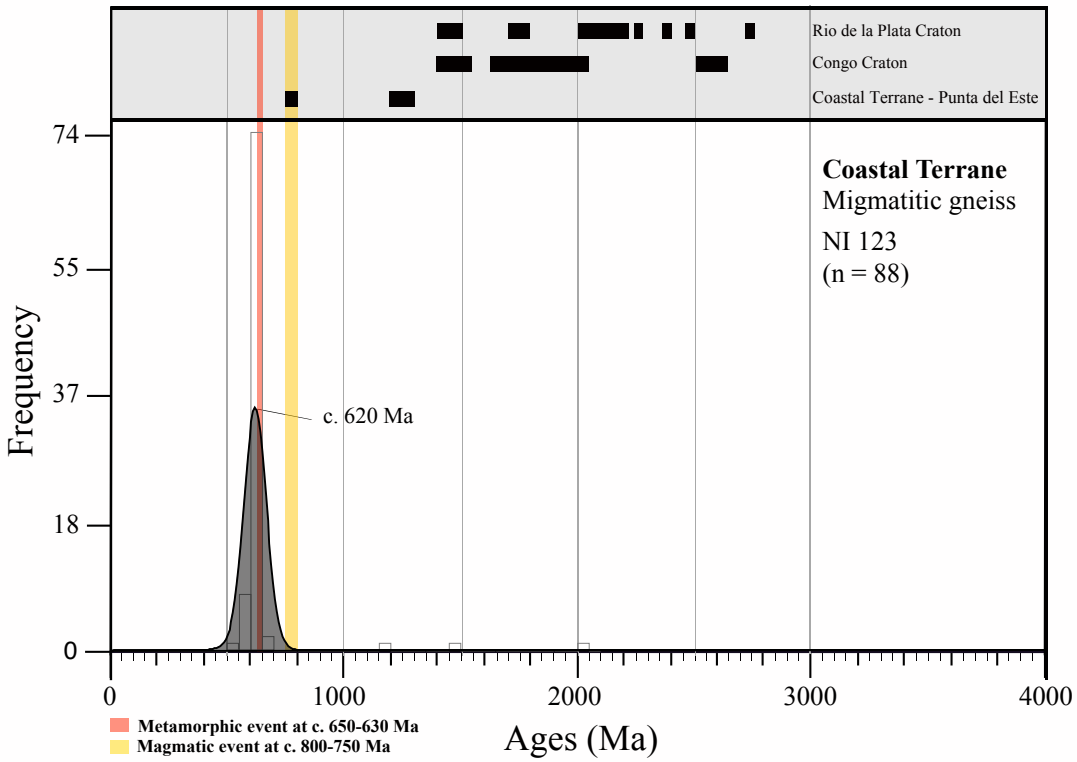

Fig. 47: Isotopic zircon ages from sample NI123 representing migmatitic gneiss from the Coastal Terrane. The data reveals one distinct peak at c. 620 Ma, and three single grains older.

The CL images of the NI123 zircons show oscillatory and non-concentric zoning. LA-ICPMS analyses of these parts of the zircons reveal a prominent age peak (Fig. 47) at c. 620 Ma. This peak corresponds by an offset of 10 Ma to the M1 metamorphism at c. 650-630 Ma determined in the Coastal Terrane (Goscombe and Gray, 2007; Konopásek et al., 2008). Due to the high grade metamorphism, most of the original detrital zircon grains probably recrystallized or dissolved in the melt during the M1 migmatitization. Recrystallized or newly crystallized zircons then give this unimodal age distribution. The three older grains, giving Meso- and Paleoproterozoic ages match the protolith ages from the Congo Craton, and are interpreted as detrital.

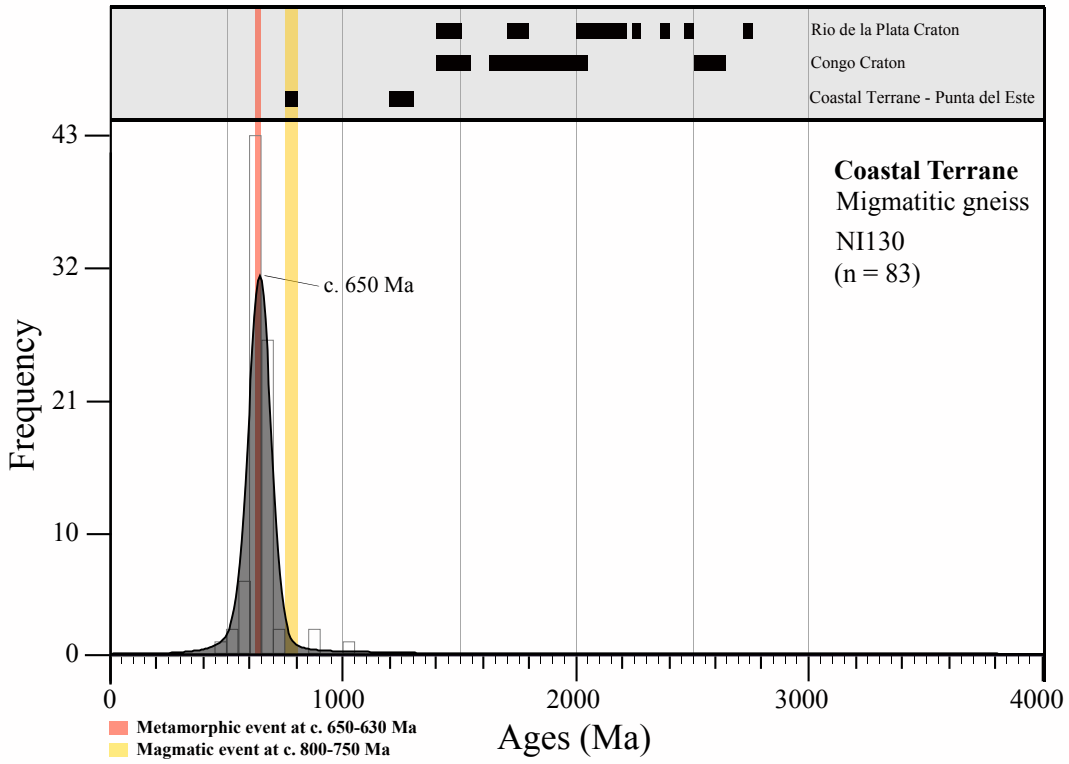

Fig. 48: Zircon ages from the migmatitic gneiss sample NI130 from the Coastal Terrane. The data show one prominent peak at c. 650 Ma and a subordinate number of zircons younger and older.

The zircons in the NI130 migmatitic gneiss show bright rims around an oscillatory zoned central parts. The analysis of the oscillatory zoned parts revealed ages from c. 580 Ma to 1.25 Ga, but nearly all the data are concentrated in a cluster at c. 650 Ma (Fig. 48).

The c. 650 Ma peak is synchronous with the 650-630 Ma high temperature / low pressure metamorphic event recorded in the Coastal Terrane (Goscombe and Gray, 2007). As in the case of the sample NI123, this distribution is interpreted as a result of nearly complete recrystallization or dissolution/neocrystallization of zircon during the c. 650-630 Ma granulite-facies metamorphism. The individual zircons dated as early Neo- and late Mesoproterozoic are interpreted as detrital.

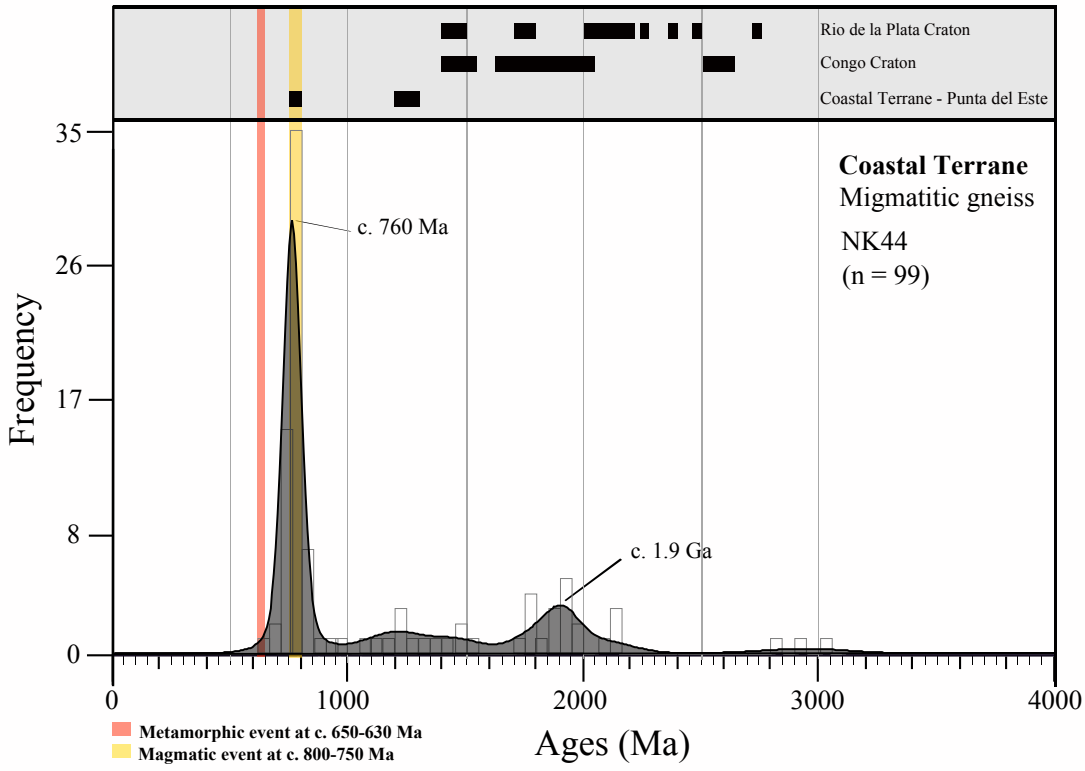

Fig. 49: Isotopic zircon ages of the migmatitic gneiss sample NK44 collected in the Coastal Terrane.
The data show peaks at c. 760 Ma and 1.92 Ga, with lower frequent peaks and single grains in between and older.

The cathodoluminescence images of the NK44 zircons show oscillatory zoned zircons, sometimes with well defined cores. The analysis revealed age peaks at c. 760 Ma and c. 1.9 Ga (Fig. 49).
The c. 760 Ma peak serves as the maximum sedimentary age from sample NK44, and falls into the time interval for the syn-rifting related magmatic event (800-760 Ma) reported from the Coastal Terrane – Punta del Este (Konopásek et al., 2008; Oyhantcabal et al., 2009a; Lenz et al., 2011). The fine oscillatory zircon textures with no overgrowths, and with corresponding ages only previously recorded in the Coastal Terrane and Punta del Este indicate a magmatic precursor as a source for the zircons. The presence of zircons of this age in the metasedimentary samples suggests, that not only the cratonic basement, but also some of the early rifting-related magmatic rocks were eroded and provided detrital material for the sedimentation in the Coastal Terrane – Punta del Este unit prior its metamorphism at 650-630 Ma.
The c. 1.9 Ga peak (Fig. 49) matches protolith ages of the Congo Craton c. 1.96 Ga (Seth et al., 1998; Kröner et al., 2004; Luft et al., 2010).

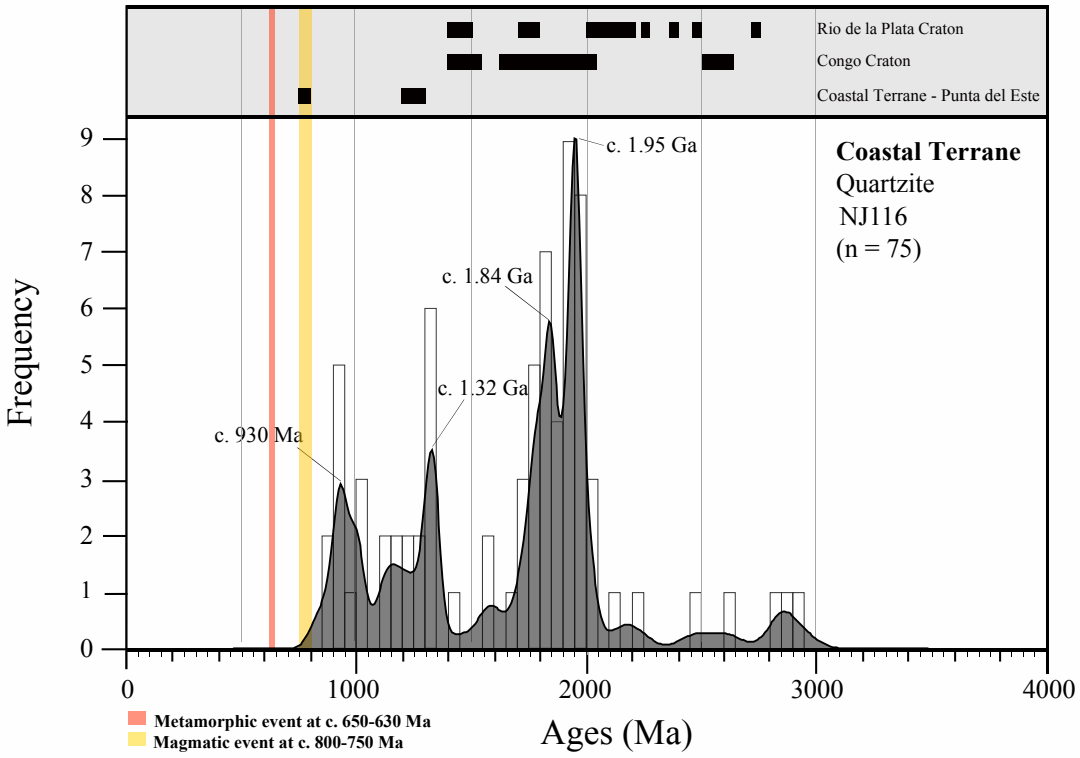

Fig. 50: Zircon ages from the quartzite sample NJ116 collected in tectonically lowermost part of the Coastal Terrane. The zircon data show peaks at c. 930 Ma, c. 1.32 Ga, c. 1.84 Ga and c. 1.95 Ga.

The zircons from NJ116 show oscillatory and concentric zoning with brighter rims cutting the oscillatory zoned parts of the crystals. LA-ICPMS analysis from the oscillatory zoned parts of the zircons has shown ages distributed from c. 830 Ma to c. 3.1 Ga, with peaks at c. 1.95 Ga, c. 1.84 Ga, c. 1.32 Ga and c. 930 Ma (Fig. 50). The c. 930 peak represent the maximum sedimentary age of sample NJ116.

The c. 1.95 Ga peak matches the protolith ages reported from the Congo Craton (c. 1.96 Ga; Seth et al., 1998; Kröner et al., 2004; Luft et al., 2010).

The c. 1.84 Ga peak can be correlated with the 1.7-1.8 Ga ages also from the Congo Craton (Kröner et al. 2004, 2010; Luft et al. 2010) and these ages are also reported from the Nico Perez Terrane of the Rio de la Plata Craton (Sánchez-Bettucci et al., 2004; Mallmann et al. 2007).

The c. 1.32 Ga ages can be linked to the ages of xenocrystic zircons at c. 1.28 Ga from the Punta del Este (Lenz et al., 2011), but rocks with these protolith ages, as well as those that could correspond to the age data at c. 930 Ma are not known from the Kaoko or the Dome Feliciano belts. The distribution of ages from the NJ116 quartzite that represents the tectonically lowermost part of the Coastal Terrane metasediments correspond well with age groups in samples collected on similar locations (Konopásek et al., 2014a).

6.5 General interpretation

Detrital zircon ages obtained from metamorphosed clastic sedimentary rocks in this study are compatible with protolith ages known either from the Congo or the Rio de la Plata Craton, except the c. 760 Ma age peak in NK44 matching the reported protolith ages of the syn-rifting metaigneous rocks in the Coastal and Punta del Este terranes. Due to the only subordinate number of zircon ages for which there is no equivalent in the basement rocks of the Congo and the Rio de la Plata Craton, there is reason to believe that the detrital material may have originated close to their respective passive cratonic margins, and that an exotic origin of the Coastal Terrane - Punta del Este (Goscombe and Gray, 2007) is not needed.

The granitoid emplacement at c. 656 Ma (Sample UA38) and the c. 610 Ma age peak interpreted as the timing of metamorphic recrystallization of the sample UA37 are more or less synchronous with the c. 620 Ma ages in NI123 and c. 650 Ma ages in NI130, both also interpreted as the timing of metamorphism. All these data fit with the previously reported ages of metamorphism and associated magmatic activity in the Coastal-Punta del Este terranes indicating the initial orogenic stage in the Dom Feliciano and Kaoko Belt, illustrated as a geodynamic model in Fig. 51.

Samples NK44 and NJ116 from the Coastal Terrane show contrasting detrital zircon age distributions. The c. 760 Ma peak in NK44 indicates that during the later stages of the rift evolution, the syn-rifting volcanics are being eroded and redeposited into the sediment of the Coastal Terrane. The source of detrital material for the sample NK44 are most likely the rifting-related volcanics of the Coastal Terrane - Punta del Este. The peak at c. 760 Ma also corresponds with similar ages of metavolcanics reported from the southern margin of the Congo Craton in the Damara Belt (Hoffman et al., 1996), revealing a synchronous timing of the initial rifting of the Congo Craton .

The quartzite sample NJ116 (for comparison see NG006 and NG009 from Konopásek et al., 2014a) represent the tectonically lowermost part of the Coastal Terrane (Fig. 51a, b), and the oldest and most frequent age peaks are compatible with the Congo Craton as a source, indicating a short transport distance for the detrital material. Its youngest peak at c. 930 Ma confirms a Neoproterozoic age of the protolith.

The Uruguayan quartzites UA38 and UB18 representing the bottom of the Punta del Este terrane (Fig. 51a, b) also show compatible ages of the Rio de la Plata Craton, indicating a short transport for the detrital material. However, the concentration of the youngest data around c. 1.2 Ga in sample UA38 and close to 1.4 Ga suggests that the dated quartzites may not represent former Neoproterozoic sediments.

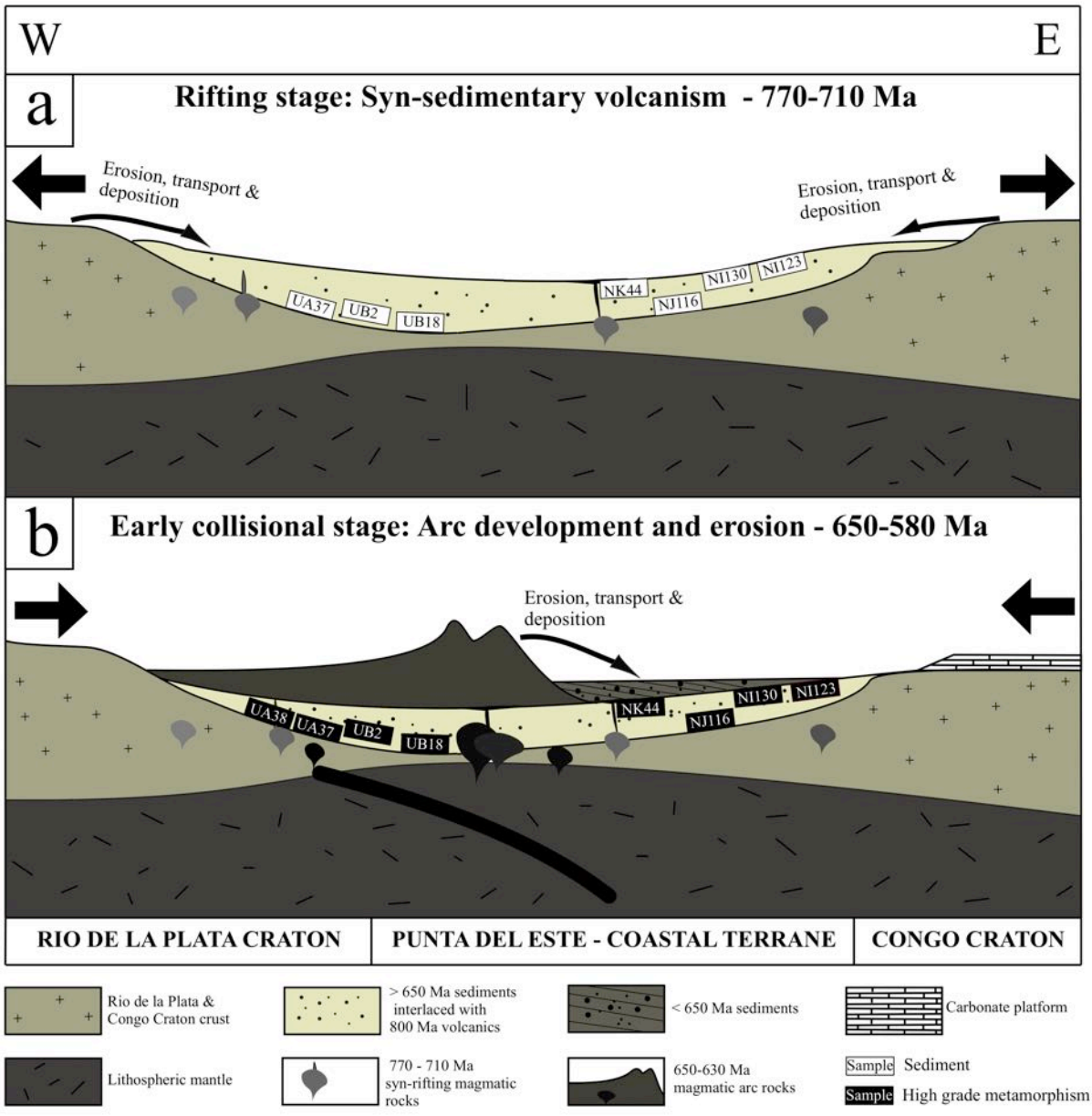

Fig. 51: Simplified geological model summarizing the interpretation in this study of the Punta del Este - Coastal Terrane. The sample are placed due to the interpreted tectonic positions in the discussion. **a)** The detrital material from the cratonic margins of Rio de la Plata and the Congo Craton gets interlaced with rifting related volcanics at c. 770-710 Ma, samples are sedimentary and marked with white background. **b)** Erosion, transportation and deposition from an c. 650-630 Ma arc into the Punta del Este - Coastal Terrane. Samples in inverse markings due to metamorphism.

7 Conclusions

The detrital and protolith ages revealed in this study provide valuable information to the geochronological studies of the Punta del Este in Uruguay and Coastal Terrane in Namibia. The conclusions of this study are:

1) The magmatic zircons from meta-igneous sample UB2 from the Punta del Este Terrane revealed protolith age of c. 770-800 Ma confirming rifting related magmatic activity in the region. Sample UB38 represents early granitoid rock emplaced at c. 656 Ma during the high grade metamorphic event in the Dom Feliciano Belt.

2) The dating of metamorphosed clastic sediments in the upper metasedimentary sequence of the Coastal Terrane revealed almost exclusively Neoproterozoic ages. Two samples (NI123 and NI130) revealed nearly uniform ages compatible with the timing of the high grade M1 metamorphic event, together with a few Paleoproterozoic ages.

3) The presence of c. 760 Ma peak from detrital zircons in the upper part of the metasedimentary sequence in the Coastal Terrane corresponds with the ages of rifting related magmatism in the Coastal Terrane – Punta del Este and also with ages known from the southern Congo Craton margin. The presence of detrital zircons of this age suggests reworking of the early syn-rifting volcanic rocks into the detrital material of the sediments.

4) The detrital zircons from quartzite samples, representing the bottom sedimentary sequence in the Coastal and Punta del Este terrane show ages comparable with the protolith ages reported from their respective craton margins. While the youngest zircons in the Coastal Terrane metasediments confirm Neoproterozoic age of the protolith, the samples from the Punta del Este Terrane may be older (Mesoproterozoic).

References

Aleinikoff, J.N., Zartman, R.E., Walter, M., Rankin, D.W., Lyttle, P.T. and Burton, W.C. (1995) U-Pb ages of metarhyolites of the Catoctin and Mount Rogers formations, Central and Southern Appalachians; evidence for two pulses of Iapetan rifting. American Journal of Science 295, 428-454.

Basei, M., Frimmel, H., Nutman, A. and Preciozzi, F. (2008a) West Gondwana amalgamation based on detrital zircon ages from Neoproterozoic Ribeira and Dom Feliciano belts of South America and comparison with coeval sequences from SW Africa. Geological Society, London, Special Publications 294, 239-256.

Basei, M., Frimmel, H., Nutman, A.P., Preciozzi, F. and Jacob, J. (2005) A connection between the Neoproterozoic Dom Feliciano (Brazil/Uruguay) and Gariep (Namibia/South Africa) orogenic belts–evidence from a reconnaissance provenance study. Precambrian Research 139, 195-221.

Basei, M.A.S. (2000) Geologia e modelagem geotectônica dos terrenos Pré-Cambrianos das regiões sul-oriental brasileira e uruguais| b possíveis correlações com províncias similares do sudoeste africano. Universidade de São Paulo.

Chew, D., Petrus, J. and Kamber, B. (2014) U–Pb LA–ICPMS dating using accessory mineral standards with variable common Pb. Chemical Geology 363, 185-199.

D'Agrella-Filho, M.S., Pacca, I.I., Trindade, R.I., Teixeira, W., Raposo, M.I.B. and Onstott, T.C. (2004) Paleomagnetism and 40Ar/39Ar ages of mafic dikes from Salvador (Brazil): new constraints on the São Francisco craton APW path between 1080 and 1010 Ma. Precambrian Research 132, 55-77.

da Silva, L.C., McNaughton, N.J., Armstrong, R., Hartmann, L.A. and Fletcher, I.R. (2005) The Neoproterozoic Mantiqueira Province and its African connections: a zircon-based U-Pb geochronologic subdivision for the Brasiliano/Pan-African systems of orogens. Precambrian Research 136, 203-240.

Davis, D.W., Krogh, T.E. and Williams, I.S. (2003) Historical development of zircon geochronology. Reviews in mineralogy and geochemistry 53, 145-181.

Ernst, R., Wingate, M., Buchan, K. and Li, Z. (2008) Global record of 1600–700Ma Large Igneous Provinces (LIPs): implications for the reconstruction of the proposed Nuna (Columbia) and Rodinia supercontinents. Precambrian Research 160, 159-178.

Fedo, C.M., Sircombe, K.N. and Rainbird, R.H. (2003) Detrital zircon analysis of the sedimentary record. Reviews in Mineralogy and Geochemistry 53, 277-303.

Fernandes, L. and Koester, E. (1999) An overview of the Neoproterozoic Dorsal de Canguçu strike-slip shear zone and its role in the tectonic evolution of the continental crust in southern Brazil. Journal of African Earth Sciences 29, 3-24.

Fitzsimons, I. (2003) Proterozoic basement provinces of southern and southwestern Australia, and their correlation with Antarctica. Geological Society, London, Special Publications 206, 93-130.
Foster, D.A., Goscombe, B.D. and Gray, D.R. (2009) Rapid exhumation of deep crust in an obliquely convergent orogen: the Kaoko Belt of the Damara Orogen. Tectonics 28.

Foster, D.A., Goscombe, B.D. and Gray, D.R. (2009) Rapid exhumation of deep crust in an obliquely convergent orogen: the Kaoko Belt of the Damara Orogen. Tectonics 28.

Franz, L., Romer, R.L. and Dingeldey, D.P. (1999) Diachronous Pan-African granulite-facies metamorphism (650 Ma and 550 Ma) in the Kaoko belt, NW Namibia. European Journal of Mineralogy 11, 167-180.

Frimmel, H.E., Basei, M. and Gaucher, C. (2011) Neoproterozoic geodynamic evolution of SW-Gondwana: a southern African perspective. Int J Earth Sci (Geol Rundsch) 100, 323-354.

Frimmel, H.E., Klötzli, U.S. and Siegfried, P.R. (1996) New Pb-Pb single zircon age constraints on the timing of Neoproterozoic glaciation and continental break-up in Namibia. The Journal of Geology, 459-469.

Frimmel, H.E., Zartman, R.E. and Späth, A. (2001) The Richtersveld Igneous Complex, South Africa: U–Pb zircon and geochemical evidence for the beginning of Neoproterozoic continental breakup. The Journal of Geology 109, 493-508.

Gaucher, C., Frei, R., Chemale Jr, F., Frei, D., Bossi, J., Martínez, G., Chiglino, L. and Cernuschi, F. (2011) Mesoproterozoic evolution of the Río de la Plata Craton in Uruguay: at the heart of Rodinia? Int J Earth Sci (Geol Rundsch) 100, 273-288.

Goscombe, B., Gray, D., Armstrong, R., Foster, D.A. and Vogl, J. (2005a) Event geochronology of the Pan-African Kaoko Belt, Namibia. Precambrian Research 140, 103. e101-103. e141.

Goscombe, B., Gray, D. and Hand, M. (2005b) Extrusional tectonics in the core of a transpressional orogen; the Kaoko Belt, Namibia. Journal of Petrology 46, 1203-1241.

Goscombe, B. and Gray, D.R. (2007) The Coastal Terrane of the Kaoko Belt, Namibia: outboard arc-terrane and tectonic significance. Precambrian Research 155, 139-158.

Goscombe, B., Hand, M., Gray, D. and Mawby, J. (2003b) The metamorphic architecture of a transpressional orogen: the Kaoko Belt, Namibia. Journal of Petrology 44, 679-711.

Goscombe, B.D. and Gray, D.R. (2008) Structure and strain variation at mid-crustal levels in a transpressional orogen: a review of Kaoko Belt structure and the character of West Gondwana amalgamation and dispersal. Gondwana Research 13, 45-85.

Gray, D., Foster, D.A., Meert, J.G., Goscombe, B.D., Armstrong, R., Trouw, R.A. and Passchier, C.W. (2008) A Damara orogen perspective on the assembly of southwestern Gondwana. Geological Society, London, Special Publications 294, 257-278.

Gray, D.R., Foster, D.A., Goscombe, B., Passchier, C.W. and Trouw, R.A. (2006) 40Ar/39Ar thermochronology of the Pan-African Damara Orogen, Namibia, with implications for tectonothermal and geodynamic evolution. Precambrian research 150, 49-72.

Greentree, M.R., Li, Z.-X., Li, X.-H. and Wu, H. (2006) Late Mesoproterozoic to earliest Neoproterozoic basin record of the Sibao orogenesis in western South China and relationship to the assembly of Rodinia. Precambrian Research 151, 79-100.

Gross, A., Droop, G., Porcher, C. and Fernandes, L. (2009) Petrology and thermobarometry of mafic granulites and migmatites from the Chafalote Metamorphic Suite: New insights into the Neoproterozoic P/T evolution of the Uruguayan—Sul-Rio-Grandense shield. Precambrian Research 170, 157-174.

Hartmann, L.A., Campal, N., Santos, J.O.S., McNaughton, N.J., Bossi, J., Schipilov, A. and Lafon, J.-M. (2001) Archean crust in the Rio de la Plata Craton, Uruguay—SHRIMP U–Pb zircon reconnaissance geochronology. Journal of South American Earth Sciences 14, 557-570.

Hartmann, L.A., Piñeyro, D., Bossi, J., Leite, J.A. and McNaughton, N.J. (2000) Zircon U-Pb SHRIMP dating of Palaeoproterozoic Isla Mala granitic magmatism in the Rio de la Plata Craton, Uruguay. Journal of South American Earth Sciences 13, 105-113.

Hartmann, L.A., Santos, J.O.S., Bossi, J., Campal, N., Schipilov, A. and McNaughton, N.J. (2002) Zircon and titanite U–Pb SHRIMP geochronology of Neoproterozoic felsic magmatism on the eastern border of the Rio de la Plata Craton, Uruguay. Journal of South American Earth Sciences 15, 229-236.

Hartmann, L.A., Santos, J.O.S., Bossi J., McNaughton, N. J. & Pineyro D., (2008b) Geocronológica SHRIMP U-Pb en circones del Gabro Rospide del Cinturón Paleoproterozoico San José, Terreno Piedra Alta, Uruguay: Ina prueba geocronológica de magmas coetáneos. Revista Sociedad Uruguaya de Geología 15, 40-53.

Hedberg, R.M. (1979) Stratigraphy of the Ovamboland Basin, South West Africa. University of Cape Town, Department of Geology.

Hoffman, P., Hawkins, D., Isachsen, C. and Bowring, S. (1996) Precise U–Pb zircon ages for early Damaran magmatism in the Summas Mountains and Welwitschia Inlier, northern Damara belt, Namibia. Communications of the geological survey of Namibia 11, 47-52.

Hoffman, P.F. (1991) Did the breakout of Laurentia turn Gondwanaland inside-out? Science 252, 1409-1412.

Jackson, S.E., Pearson, N.J., Griffin, W.L. and Belousova, E.A. (2004) The application of laser ablation-inductively coupled plasma-mass spectrometry to in situ U–Pb zircon geochronology. Chemical Geology 211, 47-69.

Janoušek, V., Konopásek, J., Ulrich, S., Erban, V., Tajčmanová, L. and Jeřábek, P. (2010) Geochemical character and petrogenesis of Pan-African Amspoort suite of the Boundary Igneous Complex in the Kaoko Belt (NW Namibia). Gondwana Research 18, 688-707.

Konopásek, J., Košler, J., Sláma, J. and Janoušek, V. (2014a) Timing and sources of pre-collisional Neoproterozoic sedimentation along the SW margin of the Congo Craton (Kaoko Belt, NW Namibia). Gondwana Research 26, 386-401.

Konopásek, J., Košler, J., Tajčmanová, L., Ulrich, S. and Kitt, S.L. (2008) Neoproterozoic igneous complex emplaced along major tectonic boundary in the Kaoko Belt (NW Namibia): ion probe and LA-ICP-MS dating of magmatic and metamorphic zircons. Journal of the Geological Society 165, 153-165.

Konopásek, J., Pilátová, E., Košler, J. and Sláma, J. (2014b) Zircon (re) crystallization during short−lived, high−P granulite facies metamorphism (Eger Complex, NW Bohemian Massif). Journal of Metamorphic Geology 32, 885-902.

Košler, J., Fonneland, H., Sylvester, P., Tubrett, M. and Pedersen, R.-B. (2002) U–Pb dating of detrital zircons for sediment provenance studies—a comparison of laser ablation ICPMS and SIMS techniques. Chemical Geology 182, 605-618.

Košler, J. and Sylvester, P.J. (2003) Present trends and the future of zircon in geochronology: laser ablation ICPMS. Reviews in Mineralogy and Geochemistry 53, 243-275.

Kröner, A., Rojas-Agramonte, Y., Hegner, E., Hoffmann, K.-H. and Wingate, M. (2010) SHRIMP zircon dating and Nd isotopic systematics of Palaeoproterozoic migmatitic orthogneisses in the Epupa Metamorphic Complex of northwestern Namibia. Precambrian Research 183, 50-69.

Kröner, S., Konopásek, J., Kröner, A., Passchier, C., Poller, U., Wingate, M. and Hofmann, K. (2004) U-Pb and Pb-Pb zircon ages for metamorphic rocks in the Kaoko Belt of Northwestern Namibia: A Palaeo-to Mesoproterozoic basement reworked during the Pan-African orogeny. South African Journal of Geology 107, 455-476.

Lenz, C., Fernandes, L., McNaughton, N., Porcher, C. and Masquelin, H. (2011) U–Pb SHRIMP ages for the Cerro Bori Orthogneisses, Dom Feliciano Belt in Uruguay: Evidences of a~ 800Ma magmatic and~ 650Ma metamorphic event. Precambrian Research 185, 149-163.

Lenz, C., Porcher, C., Fernandes, L., Masquelin, H., Koester, E. and Conceição, R. (2013) Geochemistry of the Neoproterozoic (800–767 Ma) Cerro Bori orthogneisses, Dom Feliciano Belt in Uruguay: tectonic evolution of an ancient continental arc. Mineralogy and Petrology 107, 785-806.

Li, Z., Li, X., Kinny, P. and Wang, J. (1999) The breakup of Rodinia: did it start with a mantle plume beneath South China? Earth and Planetary Science Letters 173, 171-181.

Li, Z.-X., Bogdanova, S., Collins, A.S., Davidson, A., De Waele, B., Ernst, R., Fitzsimons, I.C., Fuck, R., Gladkochub, D. and Jacobs, J. (2008) Assembly, configuration, and break-up history of Rodinia: a synthesis. Precambrian research 160, 179-210.

Li, Z.-X., Li, X., Kinny, P., Wang, J., Zhang, S. and Zhou, H. (2003b) Geochronology of Neoproterozoic syn-rift magmatism in the Yangtze Craton, South China and correlations with other continents: evidence for a mantle superplume that broke up Rodinia. Precambrian Research 122, 85-109.

Li, Z.-X., Li, W.X., Li Z.X., Wang, J., 2005. Formation of the South China Block: evidence from Sibaoan orogenic magmatism. In: Wingate, M.T.D., Pisarevsky, S.A. (Eds.), Supercontinent and Earth Evolution Symposium. Geol. Soc. Aus., Fremantle, p. 86 (Abst. 81).

Ludwig, K. (2003) Isoplot/Ex, version 3: a geochronological toolkit for Microsoft excel: Berkeley. California, Geochronology Center Berkeley.

Luft Jr, J.L., Chemale Jr, F. and Armstrong, R. (2011) Evidence of 1.7-to 1.8-Ga collisional arc in the Kaoko Belt, NW Namibia. Int J Earth Sci (Geol Rundsch) 100, 305-321.

Mallmann, G., Chemale Jr, F., Avila, J., Kawashita, K. and Armstrong, R. (2007) Isotope geochemistry and geochronology of the Nico Perez terrane, Rio de la Plata craton, Uruguay. Gondwana Research 12, 489-508.

Martin, H. (1965) The Precambrian geology of South West Africa and Namaqualand. Precambrian Research Unit, University of Cape Town.

Meert, J.G., van der Voo, R. and Ayub, S. (1995) Paleomagnetic investigation of the Neoproterozoic Gagwe lavas and Mbozi complex, Tanzania and the assembly of Gondwana. Precambrian Research 74, 225-244.

Miller, R.M. (1983) The Pan-African Damara Orogen of South West Africa/Namibia, Evolution of the Damara Orogen of South West Africa/Namibia.

Morton, A.C., Claoué-Long, J.C. and Berge, C. (1996) SHRIMP constraints on sediment provenance and transport history in the Mesozoic Statfjord Formation, North Sea. Journal of the Geological Society 153, 915-929.

Möller, A., O'brien, P., Kennedy, A. and Kröner, A. (2002) Polyphase zircon in ultrahigh−temperature granulites (Rogaland, SW Norway): constraints for Pb diffusion in zircon. Journal of Metamorphic Geology 20, 727-740.

Oyhantçabal, P. (2005a) The Sierra Ballena Shear zone: kinematics, timing and its significance for the geotectonic evolution of southeast Uruguay. Phd thesis.

Oyhantçabal, P., Siegesmund, S., Wemmer, K., Frei, R. and Layer, P. (2007) Post-collisional transition from calc-alkaline to alkaline magmatism during transcurrent deformation in the southernmost Dom Feliciano Belt (Braziliano–Pan-African, Uruguay). Lithos 98, 141-159.

Oyhantçabal, P., Siegesmund, S., Wemmer, K. and Passchier, C. (2011) The transpressional connection between Dom Feliciano and Kaoko Belts at 580–550 Ma. Int J Earth Sci (Geol Rundsch) 100, 379-390.

Oyhantçabal, P., Siegesmund, S., Wemmer, K., Presnyakov, S. and Layer, P. (2009a) Geochronological constraints on the evolution of the southern Dom Feliciano Belt (Uruguay). Journal of the Geological Society 166, 1075-1084.

Passchier, C., Trouw, R., Ribeiro, A. and Paciullo, F. (2002) Tectonic evolution of the southern Kaoko belt, Namibia. Journal of African Earth Sciences 35, 61-75.

Paton, C., Woodhead, J.D., Hellstrom, J.C., Hergt, J.M., Greig, A. and Maas, R. (2010) Improved laser ablation U−Pb zircon geochronology through robust downhole fractionation correction. Geochemistry, Geophysics, Geosystems 11.

Paulsson, O. and Andréasson, P.-G. (2002) Attempted break-up of Rodinia at 850 Ma: geochronological evidence from the Seve–Kalak Superterrane, Scandinavian Caledonides. Journal of the Geological Society 159, 751-761.

Peel, E. and Preciozzi, F. (2006) Geochronologic synthesis of the Piedra Alta Terrane, URUGUAY, V South American Symposium on Isotope Geology. Punta del Este, Uruguay, pp. 234-237.

Philipp, R.P. and Machado, R. (2005) The late Neoproterozoic granitoid magmatism of the Pelotas Batholith, southern Brazil. Journal of South American Earth Sciences 19, 461-478.

Porcher, C.C., McNaughton, N.J., Leite, J.A.D., Hartmann, L.A. & Fernandes, L.A.D (1999) dade SHRIMP em zircao: vulcanismo ácido do complexo metamórfico Porongos. Boletim de Resumos, 18 Simpósio sobre Vulcanismo e ambientes associados, Gramado, Brazil 1, 1.

Radhakrishna, T. and Mathew, J. (1996) Late Precambrian (850-800 Ma) palaeomagnetic pole for the south Indian shield from the Harohalli alkaline dykes: geotectonic implications for Gondwana reconstructions. Precambrian Research 80, 77-87.

Sánchez-Bettucci, L., Oyhantçabal, P., Loureiro, J., Ramos, V., Preciozzi, F. and Basei, M. (2004) Mineralizations of the Lavalleja Group (Uruguay), a probable Neoproterozoic volcano-sedimentary sequence. Gondwana Research 7, 745-751.

Santos, J.O.S., Hartmann, L.A., Bossi, J., Campal, N., Schipilov, A., Piñeyro, D. and McNaughton, N.J. (2003) Duration of the Trans-Amazonian Cycle and its correlation within South America based on U-Pb SHRIMP geochronology of the La Plata Craton, Uruguay. International Geology Review 45, 27-48.

Seth, B., Kröner, A., Mezger, K., Nemchin, A., Pidgeon, R. and Okrusch, M. (1998) Archaean to Neoproterozoic magmatic events in the Kaoko belt of NW Namibia and their geodynamic significance. Precambrian Research 92, 341-363.

Sláma, J., Košler, J., Condon, D.J., Crowley, J.L., Gerdes, A., Hanchar, J.M., Horstwood, M.S., Morris, G.A., Nasdala, L. and Norberg, N. (2008) Plešovice zircon—a new natural reference material for U–Pb and Hf isotopic microanalysis. Chemical Geology 249, 1-35.

Su, Q., Goldberg, S.A. and Fullagar, P.D. (1994) Precise U/Pb zircon ages of Neoproterozoic plutons in the southern Appalachian Blue Ridge and their implications for the initial rifting of Laurentia. Precambrian Research 68, 81-95.

Vermeesch, P. (2012) On the visualisation of detrital age distributions. Chemical Geology 312, 190-194.

Weil, A.B., Van der Voo, R., Mac Niocaill, C. and Meert, J.G. (1998) The Proterozoic supercontinent Rodinia: paleomagnetically derived reconstructions for 1100 to 800 Ma. Earth and Planetary Science Letters 154, 13-24.

Wiedenbeck, M., Alle, P., Corfu, F., Griffin, W., Meier, M., Oberli, F., Quadt, A.v., Roddick, J. and Spiegel, W. (1995) Three natural zircon standards for U−Th−Pb, Lu−Hf, trace element and REE analyses. Geostandards newsletter 19, 1-23.

Wingate, M.T., Campbell, I.H., Compston, W. and Gibson, G.M. (1998) Ion microprobe U–Pb ages for Neoproterozoic basaltic magmatism in south-central Australia and implications for the breakup of Rodinia. Precambrian Research 87, 135-159.

Zuffa, G.G. (1985) Optical analyses of arenites: influence of methodology on compositional results, Provenance of arenites. Springer, pp. 165-189.

Appendix A

Source	Age (Ma)	Location	Lithology
A Kröner et al., (2004)	760	Central Kaoko Zone	Migmatitic granite-gneiss
Lenz et al. (2011)	767	Cerro Bori/Cerro Aspero	Felsic mylonite
Lenz et al. (2011)	771	Chafalote	Felsic gneiss
Lenz et al. (2011)	772	Cerro Bori	Felsic migmatite
Lenz et al. (2011)	780	Cerro Bori	Felsic gneiss
Lenz et al. (2011)	786	Cerro Bori	Felsic gneiss
Lenz et al. (2011)	788	Cerro Aspero	Mafic gneiss
Lenz et al. (2011)	793	Chafalote	Mafic granulite
Lenz et al. (2011)	794	Cerri Bori	Mafic granulite
Lenz et al. (2011)	794	Chafalote	Mafic granulite
Lenz et al. (2011)	795	Cerro Bori	Mafic granulite
Lenz et al. (2011)	796	Cerro Bori	Mafic granulite
Lenz et al. (2011)	797	Cerro Bori	Mafic granulite
A Kröner et al. (2004)	894	Central Kaoko Zone	Migmatitic granite-gneiss
A Kröner et al. (2004)	925	Central Kaoko Zone	Migmatitic granite-gneiss
A Kröner et al. (2004)	930	Western Kaoko Zone	Granitic gneiss
A Kröner et al. (2004)	942	Western Kaoko Zone	Granitic gneiss
A Kröner et al. (2004)	991	Central Kaoko Zone	Migmatitic granite-gneiss
A Kröner et al. (2004)	1057	Western Kaoko Zone	Granitic gneiss
A Kröner et al. (2004)	1083	Central Kaoko Zone	Migmatitic granite-gneiss
A Kröner et al. (2004)	1091	Central Kaoko Zone	Migmatitic granite-gneiss
A Kröner et al. (2004)	1097	Central Kaoko Zone	Migmatitic granite-gneiss
A Kröner et al. (2004)	1105	Western Kaoko Zone	Granitic gneiss
A Kröner et al. (2004)	1131	Western Kaoko Zone	Granitic gneiss
A Kröner et al. (2004)	1165	Central Kaoko Zone	Migmatitic granite-gneiss
A Kröner et al. (2004)	1176	Western Kaoko Zone	Granitic gneiss
A Kröner et al. (2004)	1189	Western Kaoko Zone	Granitic gneiss
A Kröner et al. (2004)	1203	Western Kaoko Zone	Granitic gneiss
A Kröner et al. (2004)	1207	Western Kaoko Zone	Granitic gneiss
A Kröner et al. (2004)	1208	Central Kaoko Zone	Migmatitic granite-gneiss
A Kröner et al. (2004)	1216	Western Kaoko Zone	Granitic gneiss
A Kröner et al. (2004)	1234	Central Kaoko Zone	Migmatitic granite-gneiss
A Kröner et al. (2004)	1238	Western Kaoko Zone	Granitic gneiss
A Kröner et al. (2004)	1253	Western Kaoko Zone	Granitic gneiss
A Kröner et al. (2004)	1263	Western Kaoko Zone	Granitic gneiss
A Kröner et al. (2004)	1270	Western Kaoko Zone	Granitic gneiss
A Kröner et al. (2004)	1275	Western Kaoko Zone	Granitic gneiss
A Kröner et al. (2004)	1287	Western Kaoko Zone	Granitic gneiss
Luft et al. (2010)	1293	Mudorib Compl, Purros Shear	Granodioritic gneiss
Luft et al. (2010)	1301	Mudorib Compl, Purros Shear	Tonalite gneiss
A Kröner et al. (2004)	1328	Central Kaoko Zone	Migmatitic granite-gneiss
Luft et al. (2010)	1338	Hoanib valley, Purros Shear	Ultramyonolitic orthogneiss
A Kröner et al. (2004)	1349	Western Kaoko Zone	Granitic gneiss
A Kröner et al. (2004)	1352	Western Kaoko Zone	Granitic gneiss
A Kröner et al. (2004)	1358	Western Kaoko Zone	Granitic gneiss
A Kröner et al. (2004)	1375	Central Kaoko Zone	Migmatitic granite-gneiss
A Kröner et al. (2004)	1386	Western Kaoko Zone	Granitic gneiss
A Kröner et al. (2004)	1421	Western Kaoko Zone	Granitic gneiss
Oyhantcabal et al. (2005)	1429	Nico Pérez Terrane	Volcaniclastic rocks
Gaucher et al. (2010)	1433	Nico Pérez Terrane	Volcaniclastic rocks
A Kröner et al. (2004)	1435	Western Kaoko Zone	Granitic gneiss
A Kröner et al. (2004)	1465	Central Kaoko Zone	Migmatitic granite-gneiss
Oyhantcabal et al. (2005)	1492	Nico Pérez Terrane	Metagabbro
A Kröner et al. (2004)	1492	Central Kaoko Zone	Migmatitic granite-gneiss
Luft et al. (2010)	1503	Mudorib Compl, Purros Shear	Leucogranitic orthogneiss
Luft et al. (2010)	1506	Hoanib valley, Purros Shear	Ultramyonolitic orthogneiss
B. Seth et al. (1998)	1507	Damara	Granitoid orthogneiss
A Kröner et al. (2004)	1522	Central Kaoko Zone	Migmatitic granite-gneiss
A Kröner et al. (2010)	1672	Hartmann Mts., Kaokoland	Granodioritic gneiss
A Kröner et al. (2004)	1730	Central Kaoko Zone	Migmatitic granite-gneiss
Luft et al. (2010)	1731	Mudorib Compl, Purros Shear	Granodioritic gneiss
Sanchez Bettucci et al. (2004)	1735	Nico Pérez Terrane, Campanero	Orthogneiss
Mallmann et al. (2007)	1754	Nico Pérez Terrane, Campanero	Orthogneiss
A Kröner et al. (2010)	1757	Epupa Compex, Otjitanda	Porphyritic granite-gneiss
A Kröner et al. (2010)	1758	Epupa Complex SE of Okongwati	Granitic augen-gneiss
A Kröner et al. (2004)	1758	Central Kaoko Zone	Migmatitic granite-gneiss
A Kröner et al. (2010)	1759	Epupa Compex, S of Etanga	Migmatitic palaeosome
Luft et al. (2010)	1762	Mudorib Compl, Purros Shear	Tonalite gneiss
A Kröner et al. (2010)	1763	Epupa Compex, E of Otjitanda	Migmatic gneiss
A Kröner et al. (2010)	1764	Epupa Complex, Kuene	Red granite-gneiss
A Kröner et al. (2010)	1766	Epupa Complex NE of Ondova	Granodioritic gneiss
A Kröner et al. (2010)	1769	Epupa Complex	Porphyritic granite-gneiss
A Kröner et al. (2010)	1771	Kaokoland	Mylonitized augen-gneiss
A Kröner et al. (2010)	1774	Epupa Compex, SW of Etengwa	Agmatitic migmatite
A Kröner et al. (2010)	1780	Epupa Complex	Porphyritic granite-gneiss
A Kröner et al. (2010)	1785	Epupa Complex, Ovireva	Migmatitic granite-gneiss
A Kröner et al. (2010)	1790	Epupa Complex, Okongwati	Migmatitic granite-gneiss
A Kröner et al. (2010)	1802	Epupa Complex,	Migmatitic granite-gneiss
Luft et al. (2010)	1810	Mudorib Compl, Ugab riv mouth	Pyroclastic orthogneiss
A Kröner et al. (2010)	1861	Epupa Compex, E of Etanga	Hornblende biotite-gneiss
A Kröner et al. (2004)	1873	Central Kaoko Zone	Migmatitic granite-gneiss
A Kröner et al. (2004)	1919	Central Kaoko Zone	Migmatitic granite-gneiss
B. Seth et al. (1998)	1961	Damara Sequence, Kaokoveld	Granitic augen-gneiss
B. Seth et al. (1998)	1971	Damara Sequence; Kaokoveld	Granitic orthogneiss
Luft et al. (2010)	1971	Pruwes Compl, Hoanib River Valley	Granodioritic gneiss
B. Seth et al. (1998)	1985	Damara	Dioritic orthogneiss
A Kröner et al. (2004)	2005	Central Kaoko Zone	Migmatitic granite-gneiss
Hartmann et al. (2008b)	2006	Nico Pérez Terrane, Chico	Granulite
A Kröner et al. (2004)	2016	Central Kaoko Zone	Migmatitic granite-gneiss
Hartmann et al. (2008b)	2035	Nico Pérez Terrane, Chico	Granodioric gneiss
A Kröner et al. (2004)	2036	Central Kaoko Zone	Migmatitic granite-gneiss
Peel an Preciozzi, (2006)	2053	Piedra Alta Terrane	Amphibolic gneiss
Santos et al. (2003)	2056	Piedra Alta Terrane	Soca
Santos et al. (2003)	2058	Nico Pérez Terrane, Valentines	Granulite
Hartmann et al. (2000)	2065	Piedra Alta Terrane	Granulite
Hartmann et al. (2000)	2074	Piedra Alta Terrane	Granulite
Hartmann et al. (2008a)	2076	Piedra Alta Terrane	Rospide Gabbro
Santos et al. (2003)	2077	Nico Pérez Terrane, RGC	Trondhjemitic gneiss
Hartmann et al. (2008a)	2086	Piedra Alta Terrane, Transamazonian	Rospide Gabbro
Santos et al. (2003)	2140	Nico Pérez Terrane, RGC	Trondhjemitic gneiss
Santos et al. (2003)	2146	Piedra Alta Terrane, Paso Severino	Metadacite
Peel an Preciozzi, (2006)	2158	Piedra Alta Terrane, Montevideo	Porphyritic granite
Santos et al. (2003)	2165	Piedra Alta Terrane, Montevideo	Gneiss
Santos et al. (2003)	2168	Nico Pérez Terrane, Valentines	Granulite
Peel an Preciozzi, (2006)	2202	Piedra Alta Terrane, San José	Amphibolic gneiss
Hartmann et al. (2001)	2224	Nico Pérez Terrane, Valentines	Granulite
Hartmann et al. (2001)	2366	Nico Pérez Terrane, Santa Maria Chico	Granodioritic gneiss
Hartmann et al. (2001)	2489	Nico Pérez Terrane, Santa Maria Chico	Granulite
A Kröner et al. (2004)	2537	Western Kaoko Zone	Granitic gneiss
B. Seth et al. (1998)	2584	Damara Sequence	Granitic augen-gneiss
B. Seth et al. (1998)	2585	Damara Sequence, Kaokoveld	Granitic augen-gneiss
B. Seth et al. (1998)	2616	Damara Sequence	Orthogneiss
B. Seth et al. (1998)	2645	Damara Sequence, Kaokoveld	Orthogneiss
Hartmann et al. (2001)	2721	Nico Pérez Terrane, La China	Metatonalite inheritance
Hartmann et al. (2001)	3101	Nico Pérez Terrane, La China	Metatonalite inheritance

Appendix B

Sample UA37 - Quartzite (Punta del Este)														
	ISOTOPIC RATIOS							CALCULATED AGES (Ma)						
Analysis	$^{207}Pb/^{235}U$	± 2σ	$^{206}Pb/^{238}U$	±2σ	Rho	$^{207}Pb/^{206}Pb$	±2σ	$^{207}Pb/^{235}U$	±2σ	$^{206}Pb/^{238}U$	±2σ	$^{207}Pb/^{206}Pb$	±2σ	Discordance
UA37-01-010	5,2000	0,1600	0,3090	0,0110	0,7092	0,1221	0,0025	1848	26	1731	52	1985	37	7
UA37-01-017	2,8030	0,0930	0,2218	0,0078	0,5864	0,0917	0,0022	1348	25	1290	41	1431	48	4
UA37-01-025	6,4000	0,2200	0,3590	0,0120	0,2906	0,1293	0,0030	2014	27	1974	58	2050	40	2
UA37-01-027	6,5900	0,2000	0,3830	0,0130	0,5028	0,1248	0,0028	2062	27	2087	61	2034	40	−1
UA37-01-028	3,4300	0,1000	0,2638	0,0090	0,6299	0,0943	0,0020	1513	23	1509	46	1518	41	0
UA37-01-031	0,8820	0,0380	0,1032	0,0036	0,4055	0,0620	0,0021	640	20	633	21	618	69	1
UA37-01-044	3,1300	0,1000	0,2434	0,0085	0,6910	0,0933	0,0021	1438	25	1405	44	1480	42	2
UA37-01-054	2,1700	0,1300	0,1750	0,0084	0,8840	0,0899	0,0029	1129	44	1037	46	1286	69	9
UA37-01-058	3,5600	0,1100	0,2493	0,0087	0,6113	0,1036	0,0024	1542	24	1436	44	1683	42	7
UA37-01-059	5,2800	0,2000	0,3090	0,0110	0,5924	0,1239	0,0032	1860	32	1737	52	2023	46	7
UA37-01-063	5,6300	0,2200	0,3100	0,0110	0,5382	0,1317	0,0034	1898	34	1732	56	2097	45	10
UA37-01-065	3,3900	0,1100	0,2407	0,0086	0,6699	0,1021	0,0023	1502	25	1389	44	1667	42	8
UA37-01-066	6,9300	0,4900	0,4230	0,0260	0,4911	0,1188	0,0064	2082	58	2210	100	2012	87	−6
UA37-01-068	3,7600	0,1300	0,2636	0,0094	0,5908	0,1035	0,0025	1581	27	1507	47	1699	45	5
UA37-01-070	4,3900	0,2400	0,2930	0,0160	0,7014	0,1087	0,0037	1663	38	1615	71	1807	58	3
UA37-01-072	4,0700	0,2100	0,2690	0,0110	0,5590	0,1097	0,0035	1650	37	1524	53	1831	65	8
UA37-01-073	2,2240	0,0730	0,2015	0,0070	0,5909	0,0800	0,0019	1183	23	1181	37	1177	48	0
UA37-01-075	1,0970	0,0910	0,1166	0,0062	0,4493	0,0682	0,0034	676	34	696	32	927	72	−3
UA37-01-076	7,0200	0,5200	0,4400	0,0360	0,6808	0,1157	0,0048	1769	56	1940	130	1909	74	−9
UA37-02-002	5,1300	0,1100	0,2963	0,0087	0,5322	0,1256	0,0121	1839	19	1672	43	2010	180	10
UA37-02-004	5,6600	0,1300	0,3330	0,0100	0,4918	0,1233	0,0120	1931	19	1856	47	2010	170	4
UA37-02-006	5,7400	0,1200	0,3317	0,0098	0,4792	0,1255	0,0122	1935	18	1844	47	2000	180	5
UA37-02-008	5,3600	0,1200	0,3096	0,0090	0,4590	0,1256	0,0122	1878	19	1739	44	2020	180	8
UA37-02-009	5,6200	0,1300	0,3325	0,0099	0,5769	0,1226	0,0121	1920	20	1849	47	1990	180	4
UA37-02-010	4,8500	0,1200	0,2983	0,0094	0,5706	0,1179	0,0121	1792	22	1678	46	1910	180	7
UA37-02-012	4,9100	0,1100	0,3148	0,0092	0,6457	0,1131	0,0110	1808	18	1763	45	1850	180	3
UA37-02-017	4,8400	0,1100	0,3165	0,0094	0,5688	0,1109	0,0110	1791	19	1770	46	1810	180	1
UA37-02-023	5,7200	0,1600	0,3290	0,0110	0,5887	0,1261	0,0131	1926	24	1835	51	2030	180	5
UA37-02-025	12,9900	0,2900	0,4610	0,0140	0,6719	0,2044	0,0201	2676	21	2445	61	2850	160	9
UA37-02-026	5,8500	0,1600	0,3180	0,0100	0,5198	0,1334	0,0129	1953	24	1784	49	2140	170	9
UA37-03-007	0,9980	0,0780	0,1110	0,0040	0,3369	0,0652	0,0030	702	36	678	23	705	94	4
UA37-03-008	0,8860	0,0850	0,1039	0,0040	0,1885	0,0618	0,0044	636	44	637	23	550	150	0
UA37-03-009	0,9070	0,0640	0,1042	0,0036	0,5107	0,0631	0,0022	654	32	639	21	674	74	2
UA37-03-015	0,9070	0,0690	0,0992	0,0037	0,2600	0,0663	0,0031	652	36	609	21	737	97	7
UA37-03-016	3,0500	0,2100	0,2363	0,0086	0,5379	0,0936	0,0026	1412	51	1367	45	1486	49	3
UA37-03-018	5,9000	0,3700	0,3460	0,0110	0,2274	0,1237	0,0025	1955	53	1914	54	2020	35	2
UA37-03-019	0,9090	0,0570	0,1062	0,0035	0,2025	0,0621	0,0014	654	30	650	20	680	46	1
UA37-03-020	4,9200	0,3100	0,3130	0,0100	0,2204	0,1140	0,0022	1803	53	1755	49	1870	35	3
UA37-03-021	1,5600	0,1300	0,1442	0,0066	0,8348	0,0785	0,0026	938	50	868	37	1112	72	8
UA37-03-022	5,1300	0,3200	0,3015	0,0099	0,4216	0,1234	0,0023	1831	53	1699	49	2001	33	8
UA37-03-024	0,8290	0,0590	0,0976	0,0033	0,1304	0,0616	0,0026	613	32	600	19	632	76	2
UA37-03-027	0,8520	0,0620	0,0984	0,0035	0,3299	0,0628	0,0028	620	33	605	21	657	89	2
UA37-03-030	0,9000	0,0580	0,1025	0,0037	0,2744	0,0637	0,0017	654	31	629	22	736	56	4
UA37-03-033	0,8820	0,0700	0,1009	0,0044	0,0349	0,0634	0,0037	642	35	619	26	720	110	4
UA37-03-036	5,5200	0,3800	0,3190	0,0130	0,8335	0,1255	0,0025	1911	58	1780	62	2016	35	7
UA37-03-038	0,7770	0,0500	0,0911	0,0031	0,3855	0,0619	0,0015	580	29	562	19	648	54	3
UA37-03-039	0,8830	0,0710	0,0985	0,0036	0,2132	0,0650	0,0037	644	40	606	21	700	120	6
UA37-03-042	1,1610	0,0890	0,1199	0,0048	0,5950	0,0702	0,0026	774	42	729	27	894	76	6
UA37-03-046	4,5800	0,2800	0,2793	0,0093	0,4168	0,1189	0,0022	1744	51	1587	47	1904	33	10
UA37-03-050	5,1000	0,3100	0,3170	0,0100	0,1608	0,1167	0,0021	1834	52	1773	51	1894	33	3
UA37-03-053	0,9210	0,0640	0,0980	0,0035	0,3441	0,0682	0,0025	662	34	603	20	764	76	10
UA37-03-055	5,0200	0,3400	0,2930	0,0110	0,6944	0,1243	0,0027	1813	57	1654	56	1989	39	10
UA37-03-059	2,9500	0,2000	0,2291	0,0082	0,3832	0,0934	0,0025	1384	51	1328	43	1434	52	4
UA37-03-060	0,9090	0,0610	0,0972	0,0033	0,3716	0,0678	0,0020	653	32	598	19	825	61	9
UA37-03-062	0,8360	0,0550	0,0973	0,0032	0,0962	0,0623	0,0019	611	30	598	19	616	63	2
UA37-03-063	5,4000	0,3400	0,3230	0,0110	0,2750	0,1213	0,0025	1876	54	1805	51	1943	38	4
UA37-03-066	0,9170	0,0650	0,1034	0,0036	0,1279	0,0643	0,0026	654	34	634	21	683	88	3
UA37-03-068	0,9010	0,0570	0,1085	0,0036	0,1082	0,0602	0,0014	653	30	664	21	610	49	−2
UA37-03-069	0,8030	0,0540	0,0944	0,0032	0,1719	0,0617	0,0021	596	31	582	19	591	69	2
UA37-03-070	5,5600	0,3500	0,3210	0,0110	0,3647	0,1256	0,0025	1904	54	1794	52	2026	36	6
UA37-03-071	4,2300	0,2800	0,2776	0,0098	0,4117	0,1105	0,0031	1673	55	1580	49	1817	51	6
UA37-03-072	0,8090	0,0570	0,0976	0,0034	0,1812	0,0601	0,0023	602	31	600	20	556	78	0
UA37-03-073	3,2200	0,2000	0,2314	0,0081	0,4584	0,1009	0,0020	1459	49	1345	42	1638	38	8
UA37-03-074	4,9200	0,3100	0,3020	0,0100	0,3309	0,1182	0,0024	1801	53	1705	52	1934	37	6
UA37-03-075	3,0800	0,2200	0,2297	0,0088	0,7255	0,0972	0,0026	1433	53	1331	46	1579	51	8
UA37-03-076	0,7970	0,0510	0,0927	0,0031	0,3237	0,0624	0,0014	594	28	572	19	689	50	4
UA37-03-078	4,1800	0,2600	0,2869	0,0098	0,3732	0,1057	0,0021	1664	52	1625	49	1730	37	2
UA37-03-082	0,8340	0,0550	0,0995	0,0034	0,0682	0,0608	0,0018	616	30	611	20	611	60	1
UA37-03-083	0,7330	0,0520	0,0910	0,0034	0,4696	0,0584	0,0021	560	30	561	20	579	76	0
UA37-03-085	0,8780	0,0570	0,1070	0,0036	0,2078	0,0595	0,0017	640	31	655	21	565	58	−2
UA37-03-086	5,3000	0,3300	0,3130	0,0110	0,3475	0,1228	0,0023	1866	54	1751	53	1999	33	7
UA37-03-087	3,0100	0,1900	0,2242	0,0079	0,4278	0,0974	0,0022	1408	49	1308	42	1584	43	8
UA37-03-088	0,9170	0,0590	0,1066	0,0037	0,2012	0,0624	0,0016	662	31	653	21	668	56	1
UA37-03-090	0,9640	0,0650	0,1075	0,0039	0,5038	0,0650	0,0018	682	33	658	23	722	58	4
UA37-03-091	5,1000	0,3200	0,3130	0,0110	0,3812	0,1182	0,0022	1832	52	1752	53	1939	32	5
UA37-03-092	0,8400	0,0650	0,0931	0,0036	0,0859	0,0654	0,0034	615	36	573	21	670	110	7
UA37-03-097	0,8780	0,0550	0,1069	0,0041	0,1360	0,0596	0,0017	645	30	656	24	583	59	−2
UA37-03-101	2,2800	0,1400	0,1991	0,0067	0,1072	0,0831	0,0017	1207	43	1170	36	1245	41	3
UA37-03-107	0,7580	0,0480	0,0894	0,0035	0,2736	0,0615	0,0018	571	28	552	21	579	61	3
UA37-03-110	4,6900	0,2900	0,2880	0,0110	0,3765	0,1181	0,0024	1761	52	1630	55	1892	37	8
UA37-03-111	0,8880	0,0570	0,1037	0,0038	0,2128	0,0621	0,0017	643	31	636	22	622	59	1
UA37-03-112	3,8600	0,2400	0,2590	0,0100	0,3280	0,1081	0,0026	1603	51	1486	52	1742	47	8
UA37-03-113	6,4200	0,4000	0,3530	0,0140	0,3350	0,1319	0,0031	2037	55	1941	65	2108	40	5
UA37-03-114	1,0200	0,1400	0,1073	0,0072	0,3177	0,0689	0,0081	692	69	656	42	780	240	5
UA37-03-115	0,8130	0,0600	0,0903	0,0040	0,0901	0,0653	0,0035	595	34	559	23	660	100	6
UA37-03-116	0,7540	0,0610	0,0887	0,0039	0,1228	0,0617	0,0037	576	34	547	23	570	110	5
UA37-03-117	0,7680	0,0500	0,0886	0,0035	0,2355	0,0629	0,0020	577	29	547	21	652	66	5
UA37-03-121	0,7610	0,0520	0,0890	0,0035	0,3407	0,0620	0,0021	573	29	549	21	647	72	4
UA37-03-124	4,9400	0,3100	0,2940	0,0100	0,2416	0,1219	0,0027	1809	54	1660	52	1966	40	9
UA37-03-126	0,7860	0,0540	0,0897	0,0035	0,2699	0,0636	0,0025	590	31	553	21	635	78	7
UA37-03-127	0,8010	0,0650	0,0897	0,0038	0,0186	0,0648	0,0037	588	36	553	23	660	120	6
UA37-03-129	0,7920	0,0510	0,0921	0,0033	0,1199	0,0624	0,0017	593	29	568	19	607	60	4
UA37-03-131	2,2800	0,1500	0,1898	0,0069	0,3910	0,0871	0,0024	1203	47	1122	37	1256	54	7

Sample UB2 - Quartz-feldspatic gneiss (Punta del Este)													
	ISOTOPIC RATIOS							CALCULATED AGES (Ma)					
Analysis	$^{207}Pb/^{235}U$	± 2σ	$^{206}Pb/^{238}U$	±2σ	Rho	$^{207}Pb/^{206}Pb$	±2σ	$^{207}Pb/^{235}U$	±2σ	$^{206}Pb/^{238}U$	±2σ	$^{207}Pb/^{206}Pb$	±2σ	Discordance
UB2-01	4,8300	0,1700	0,3168	0,0077	0,5993	0,1106	0,0028	1788	29	1775	37	1817	46	1
UB2-02	1,1070	0,0370	0,1241	0,0029	0,6732	0,0647	0,0015	757	18	755	17	773	49	0
UB2-05	1,0970	0,0370	0,1243	0,0031	0,6662	0,0640	0,0016	754	18	754	18	742	51	0
UB2-06	1,0740	0,0390	0,1220	0,0030	0,4835	0,0638	0,0019	739	19	743	17	739	61	−1
UB2-07	1,0580	0,0370	0,1152	0,0029	0,5815	0,0666	0,0017	730	18	702	17	771	55	4
UB2-08	0,9310	0,0310	0,1083	0,0026	0,6181	0,0623	0,0015	665	16	662	15	660	49	0
UB2-09	0,9120	0,0320	0,1050	0,0025	0,4930	0,0630	0,0017	655	17	645	15	685	58	2
UB2-10	1,1050	0,0350	0,1233	0,0029	0,6649	0,0650	0,0014	756	17	750	17	753	47	1
UB2-12	1,1530	0,0380	0,1257	0,0030	0,6970	0,0665	0,0015	776	18	762	17	839	47	2
UB2-13	1,1140	0,0360	0,1237	0,0031	0,7094	0,0653	0,0014	756	17	751	17	788	46	1
UB2-14	0,9010	0,0290	0,1061	0,0026	0,6426	0,0616	0,0014	651	16	650	15	648	49	0
UB2-15	0,9650	0,0340	0,1115	0,0028	0,6616	0,0628	0,0015	681	18	680	16	711	53	0
UB2-16	1,1520	0,0390	0,1276	0,0030	0,2920	0,0655	0,0016	772	18	773	17	765	49	0
UB2-17	0,9280	0,0310	0,1110	0,0026	0,6080	0,0606	0,0015	664	16	678	15	634	51	−2
UB2-18	1,0630	0,0350	0,1197	0,0029	0,6406	0,0644	0,0015	731	17	730	17	761	47	0
UB2-19	1,0090	0,0330	0,1152	0,0029	0,6839	0,0635	0,0014	706	17	703	17	719	47	0
UB2-20	1,0650	0,0340	0,1181	0,0028	0,6644	0,0654	0,0015	735	17	719	16	757	48	2
UB2-21	0,9410	0,0290	0,1106	0,0026	0,6659	0,0617	0,0013	673	15	675	15	655	46	0
UB2-22	1,1470	0,0380	0,1297	0,0030	0,5836	0,0641	0,0015	774	18	785	17	744	50	1
UB2-24	1,2680	0,0400	0,1402	0,0033	0,2384	0,0656	0,0015	829	18	844	19	794	48	−2
UB2-25	0,9220	0,0300	0,1090	0,0026	0,6372	0,0613	0,0014	663	16	666	15	656	48	0
UB2-26	5,1200	0,1800	0,3149	0,0086	0,8560	0,1179	0,0023	1837	29	1761	42	1933	36	4
UB2-28	1,0880	0,0350	0,1245	0,0030	0,6256	0,0634	0,0014	745	17	756	17	747	48	−1
UB2-29	1,1140	0,0370	0,1270	0,0031	0,6561	0,0636	0,0015	758	18	769	18	715	50	−1
UB2-32	0,9240	0,0300	0,1088	0,0026	0,5802	0,0616	0,0014	664	16	665	15	651	51	0
UB2-33	0,8890	0,0300	0,1070	0,0025	0,5076	0,0603	0,0015	642	16	655	15	584	54	−2
UB2-34	1,1820	0,0370	0,1303	0,0031	0,7019	0,0658	0,0014	789	17	789	18	806	44	0
UB2-36	0,9050	0,0300	0,1065	0,0025	0,6631	0,0616	0,0014	658	16	653	15	642	49	1
UB2-37	1,0420	0,0380	0,1196	0,0029	0,4136	0,0632	0,0018	720	18	728	17	683	56	−1
UB2-38	1,2480	0,0420	0,1366	0,0032	0,6601	0,0663	0,0015	819	19	825	18	802	49	−1
UB2-39	1,7790	0,0750	0,1661	0,0050	0,8575	0,0777	0,0018	1029	28	990	28	1107	47	4
UB2-40	1,1220	0,0380	0,1277	0,0031	0,5702	0,0637	0,0016	767	18	774	18	745	55	−1
UB2-41	0,9030	0,0320	0,1080	0,0026	0,4871	0,0606	0,0017	649	17	661	15	608	57	−2
UB2-43	0,9050	0,0300	0,1084	0,0025	0,5729	0,0606	0,0014	653	16	665	15	616	51	−2
UB2-45	1,0620	0,0390	0,1215	0,0030	0,5245	0,0634	0,0018	733	19	739	17	697	59	−1
UB2-46	0,8690	0,0320	0,0979	0,0029	0,5552	0,0644	0,0018	631	17	602	17	766	53	−5
UB2-48	1,0600	0,0380	0,1226	0,0032	0,7172	0,0627	0,0015	731	18	745	18	717	50	−2
UB2-49	1,1770	0,0390	0,1302	0,0031	0,6191	0,0656	0,0015	786	18	788	18	780	49	0
UB2-50	1,1580	0,0380	0,1317	0,0031	0,6368	0,0638	0,0015	779	18	798	18	748	47	2
UB2-53	0,9050	0,0300	0,1042	0,0028	0,7332	0,0630	0,0014	656	16	638	16	732	47	3
UB2-54	0,9120	0,0320	0,1073	0,0026	0,7267	0,0616	0,0014	656	17	657	15	650	49	0
UB2-57	0,9940	0,0360	0,1140	0,0028	0,5095	0,0632	0,0017	695	18	696	16	683	57	0
UB2-59	1,0750	0,0370	0,1193	0,0034	0,6396	0,0654	0,0015	742	18	724	20	813	46	2
UB2-60	1,1740	0,0420	0,1289	0,0033	0,3043	0,0661	0,0018	781	18	783	18	772	50	0
UB2-61	0,8920	0,0300	0,1051	0,0027	0,4712	0,0616	0,0015	643	15	643	15	659	47	0
UB2-62	1,1000	0,0370	0,1234	0,0031	0,5925	0,0647	0,0016	755	18	749	18	782	51	1
UB2-64	0,9070	0,0290	0,1097	0,0027	0,6308	0,0600	0,0014	653	16	671	15	600	49	3
UB2-65	1,2010	0,0420	0,1311	0,0034	0,5636	0,0664	0,0018	795	19	793	19	813	54	0
UB2-66	1,1360	0,0380	0,1254	0,0032	0,5925	0,0657	0,0017	766	18	760	18	759	54	1
UB2-67	1,1320	0,0400	0,1268	0,0031	0,5180	0,0647	0,0016	761	19	769	18	734	52	−1

Sample UA38 - Orthogneiss (Punta del Este)													
	ISOTOPIC RATIOS							CALCULATED AGES (Ma)					
Analysis	$^{207}Pb/^{235}U$	± 2σ	$^{206}Pb/^{238}U$	±2σ	Rho	$^{207}Pb/^{206}Pb$	±2σ	$^{207}Pb/^{235}U$	±2σ	$^{206}Pb/^{238}U$	±2σ	$^{207}Pb/^{206}Pb$	±2σ	Discordance
UA38-01	0,9	0,034	0,1081	0,003	0,5222	0,0614	0,0017	651	18	663	17	627	59	−2
UA38-02	0,908	0,039	0,1071	0,0031	0,14048	0,0614	0,0023	658	21	655,8	18	599	74	0
UA38-03	0,958	0,033	0,1103	0,0031	0,46661	0,0623	0,0015	679,1	17	674,2	18	677	54	1
UA38-04	0,9	0,031	0,1074	0,0029	0,48218	0,0611	0,0015	652,7	16	657	17	627	53	−1
UA38-05	0,86	0,029	0,103	0,0028	0,50327	0,06103	0,0014	630	15	631,8	16	633	48	0
UA38-06	0,914	0,031	0,1075	0,0029	0,47153	0,0621	0,0015	658	16	658,4	17	681	51	0
UA38-07	0,952	0,034	0,1094	0,0031	0,43764	0,063	0,0017	675	18	669	18	691	58	1
UA38-08	0,908	0,032	0,1069	0,0029	0,54808	0,0616	0,0015	657	17	654,4	17	645	52	0
UA38-09	0,923	0,031	0,1068	0,003	0,54066	0,0629	0,0015	659	16	653	17	685	51	1
UA38-10	0,914	0,033	0,1083	0,003	0,36279	0,0616	0,0016	658	17	662,2	17	633	57	−1
UA38-11	0,873	0,032	0,102	0,0029	0,46685	0,0621	0,0017	641	17	626,5	17	683	59	2
UA38-12	0,912	0,032	0,1064	0,0029	0,33666	0,0617	0,0016	657	17	651,5	17	638	58	1
UA38-13	0,917	0,034	0,107	0,003	0,29503	0,0621	0,0018	658	18	656,1	17	649	60	0
UA38-14	0,918	0,032	0,1082	0,003	0,4858	0,0617	0,0015	660,3	17	662,2	17	651	53	0
UA38-15	0,911	0,032	0,1063	0,003	0,44075	0,0624	0,0016	656	17	651,4	17	686	56	1
UA38-16	0,914	0,031	0,1075	0,003	0,47919	0,0613	0,0015	659,6	16	659	17	638	53	0
UA38-17	0,911	0,031	0,1085	0,003	0,56734	0,0609	0,0014	655,6	16	664,1	17	627	50	−1
UA38-18	0,931	0,032	0,1091	0,003	0,48341	0,0622	0,0016	667	17	667,6	18	651	55	0
UA38-19	0,927	0,031	0,1091	0,003	0,58537	0,06164	0,0014	663,8	16	667,4	18	655	48	−1
UA38-20	0,913	0,031	0,1073	0,003	0,49697	0,0617	0,0015	656,4	16	659,4	17	644	52	0
UA38-21	0,907	0,032	0,1072	0,003	0,49915	0,0618	0,0016	659	17	656,1	18	659	55	0
UA38-22	0,925	0,032	0,1068	0,003	0,49021	0,0625	0,0015	663,4	16	654,3	17	693	51	1
UA38-23	0,859	0,031	0,1023	0,0029	0,41647	0,061	0,0017	628	17	627,3	17	621	58	0
UA38-24	0,901	0,031	0,1063	0,0029	0,53421	0,0615	0,0015	649	17	651	17	631	53	0

Sample UB18 - Quartzite (Punta del Este)														
	ISOTOPIC RATIOS							CALCULATED AGES (Ma)						
Analysis	$^{207}Pb/^{235}U$	± 2σ	$^{206}Pb/^{238}U$	±2σ	Rho	$^{207}Pb/^{206}Pb$	±2σ	$^{207}Pb/^{235}U$	±2σ	$^{206}Pb/^{238}U$	±2σ	$^{207}Pb/^{206}Pb$	±2σ	Discordance
UB18-01-43	0,4110	0,0150	0,0547	0,0017	0,6107	0,0545	0,0012	349	11	343	10	345	49	2
UB18-01-44	0,4030	0,0150	0,0553	0,0018	0,3684	0,0529	0,0013	343	11	347	11	314	50	−1
UB18-01-45	0,4050	0,0150	0,0553	0,0017	0,6002	0,0531	0,0012	345	10	347	11	329	50	−1
UB18-01-46	0,4140	0,0150	0,0566	0,0018	0,5922	0,0530	0,0012	352	11	355	11	338	50	−1
UB18-01-47	0,4250	0,0150	0,0567	0,0018	0,5588	0,0544	0,0012	358	11	356	11	318	48	1
UB18-01-48	0,4140	0,0150	0,0559	0,0017	0,6330	0,0537	0,0012	351	11	350	11	327	48	0
UB18-01-49	0,4090	0,0150	0,0557	0,0017	0,5970	0,0533	0,0012	347	11	350	11	316	48	−1
UB18-01-50	0,4190	0,0160	0,0565	0,0018	0,6306	0,0538	0,0012	355	11	355	11	337	48	0
UB18-01-51	0,4060	0,0150	0,0554	0,0018	0,6276	0,0532	0,0012	345	11	348	11	371	49	−1
UB18-01-52	0,4130	0,0150	0,0550	0,0017	0,4971	0,0545	0,0013	351	11	346	10	416	52	1
UB18-02-01	6,2500	0,1600	0,3500	0,0110	0,5799	0,1295	0,0131	2019	22	1932	52	2070	180	5
UB18-02-02	13,0100	0,3000	0,4770	0,0150	0,6677	0,1978	0,0202	2676	23	2517	64	2790	160	6
UB18-02-05	5,0100	0,1200	0,3204	0,0099	0,5322	0,1134	0,0111	1817	21	1789	48	1830	180	2
UB18-02-06	10,5600	0,2400	0,4610	0,0140	0,5483	0,1661	0,0162	2480	20	2443	61	2500	160	2
UB18-02-07	7,8300	0,3000	0,3740	0,0140	0,8532	0,1518	0,0155	2213	37	2041	67	2310	180	8
UB18-02-12	10,6500	0,2400	0,4230	0,0130	0,6386	0,1826	0,0183	2491	21	2277	57	2650	160	9
UB18-02-15	6,5200	0,1600	0,3660	0,0110	0,7136	0,1292	0,0130	2047	21	2008	54	2080	180	2
UB18-02-16	5,9500	0,1500	0,3280	0,0100	0,6291	0,1316	0,0129	1967	23	1835	50	2130	170	7
UB18-02-18	11,0100	0,2700	0,4490	0,0140	0,6808	0,1778	0,0178	2521	23	2391	61	2650	170	5
UB18-02-19	6,5200	0,1600	0,3640	0,0110	0,5301	0,1299	0,0128	2043	21	2000	53	2110	180	2
UB18-02-23	9,5500	0,2100	0,4270	0,0130	0,5972	0,1622	0,0167	2390	20	2289	57	2510	170	4
UB18-02-24	5,4300	0,1500	0,3320	0,0100	0,6909	0,1186	0,0120	1883	23	1849	50	1930	190	2
UB18-02-25	6,6900	0,1600	0,3650	0,0110	0,6255	0,1329	0,0129	2074	21	2004	53	2160	170	3
UB18-02-26	7,3900	0,1900	0,3950	0,0120	0,5920	0,1357	0,0139	2151	23	2143	56	2180	170	0
UB18-02-28	5,3300	0,1400	0,3189	0,0098	0,5814	0,1212	0,0120	1877	22	1790	48	1960	180	5
UB18-02-29	6,8700	0,1600	0,3750	0,0110	0,5968	0,1329	0,0131	2096	21	2057	54	2130	170	2
UB18-02-30	6,1700	0,1500	0,3530	0,0110	0,5383	0,1268	0,0131	1999	21	1947	52	2040	170	3
UB18-02-33	11,2400	0,2700	0,4590	0,0140	0,7361	0,1776	0,0181	2542	22	2431	63	2620	160	5
UB18-02-40	6,8200	0,1600	0,3680	0,0110	0,6027	0,1344	0,0130	2086	21	2021	52	2150	180	3
UB18-02-49	6,9400	0,1700	0,3820	0,0120	0,5564	0,1318	0,0128	2101	22	2083	55	2150	170	1
UB18-02-69	6,4800	0,1600	0,3580	0,0110	0,6389	0,1313	0,0130	2044	22	1975	52	2100	180	3
UB18-03-03	2,7100	0,1600	0,2214	0,0078	0,1710	0,0888	0,0017	1327	45	1289	41	1361	39	3
UB18-03-04	3,8700	0,2900	0,3010	0,0180	0,6781	0,0932	0,0025	1567	48	1661	78	1539	53	−6
UB18-03-06	3,1100	0,1900	0,2446	0,0086	0,1324	0,0922	0,0018	1433	47	1410	45	1425	39	2
UB18-03-07	6,3300	0,3800	0,3620	0,0120	0,0152	0,1268	0,0018	2022	52	1987	58	2037	25	2
UB18-03-10	2,6300	0,1800	0,2128	0,0087	0,8285	0,0896	0,0015	1295	53	1244	47	1365	34	4
UB18-03-11	5,5300	0,3400	0,3390	0,0110	0,0352	0,1183	0,0021	1904	53	1881	56	1907	33	1
UB18-03-14	4,5900	0,4200	0,3290	0,0230	0,6180	0,1012	0,0041	1689	63	1775	99	1657	77	−5
UB18-03-16	5,5800	0,3600	0,3310	0,0120	0,6320	0,1223	0,0026	1913	56	1842	59	1972	38	4
UB18-03-17	4,7800	0,4000	0,2950	0,0200	0,7972	0,1175	0,0033	1690	45	1612	81	1902	53	5
UB18-03-18	1,9400	0,1400	0,1732	0,0074	0,4152	0,0812	0,0026	1088	46	1025	41	1196	65	6
UB18-03-20	2,2700	0,2400	0,1940	0,0180	0,8415	0,0849	0,0025	1100	52	1090	86	1324	58	1
UB18-03-23	7,2700	0,4500	0,3900	0,0140	0,3356	0,1352	0,0025	2140	56	2120	63	2133	34	1
UB18-03-25	6,3300	0,4000	0,3450	0,0120	0,2555	0,1331	0,0032	2016	56	1906	59	2105	42	6
UB18-03-27	1,9200	0,1300	0,1918	0,0074	0,1935	0,0726	0,0028	1086	47	1131	40	953	79	−4
UB18-03-28	5,0000	0,3100	0,3060	0,0110	0,2269	0,1185	0,0028	1819	53	1721	56	1903	41	6
UB18-03-29	16,6000	1,0000	0,6010	0,0240	0,5249	0,2003	0,0041	2913	59	3018	94	2800	34	−3
UB18-03–22	3,1300	0,2700	0,2250	0,0130	0,6971	0,1009	0,0032	1383	65	1288	69	1652	61	7

Sample NI123 - Migmatitic gneiss (Coastal Terrane)														
	ISOTOPIC RATIOS							CALCULATED AGES (Ma)						
Analysis	$^{207}Pb/^{235}U$	± 2σ	$^{206}Pb/^{238}U$	±2σ	Rho	$^{207}Pb/^{206}Pb$	±2σ	$^{207}Pb/^{235}U$	±2σ	$^{206}Pb/^{238}U$	±2σ	$^{207}Pb/^{206}Pb$	±2σ	Discordance
NI123-01	0,7970	0,0330	0,0964	0,0031	0,4388	0,0600	0,0018	593	19	593	19	554	64	0
NI123-02	2,2520	0,0870	0,1958	0,0063	0,2890	0,0834	0,0022	1179	26	1151	34	1197	50	2
NI123-03	0,8830	0,0330	0,1033	0,0033	0,6234	0,0620	0,0014	641	17	634	19	638	49	1
NI123-04	5,4700	0,2100	0,3200	0,0100	0,7906	0,1240	0,0024	1892	33	1787	51	2004	34	6
NI123-05	0,8620	0,0310	0,1005	0,0033	0,6845	0,0622	0,0014	630	17	618	19	650	49	2
NI123-06	0,8400	0,0310	0,1017	0,0032	0,6634	0,0599	0,0013	618	17	625	19	576	48	−1
NI123-07	0,8410	0,0390	0,0978	0,0031	0,1245	0,0624	0,0022	609	18	601	18	570	62	1
NI123-08	0,7870	0,0290	0,0916	0,0030	0,5750	0,0623	0,0015	584	16	565	17	654	54	3
NI123-09	0,8470	0,0310	0,1016	0,0033	0,6397	0,0605	0,0014	624	17	623	19	626	49	0
NI123-10	0,8480	0,0320	0,0991	0,0032	0,4047	0,0621	0,0019	617	18	609	19	629	64	1
NI123-12	0,8290	0,0280	0,0992	0,0032	0,6286	0,0606	0,0014	613	16	609	19	615	50	1
NI123-13	0,8210	0,0350	0,0989	0,0033	0,3735	0,0602	0,0021	603	19	607	19	567	69	−1
NI123-14	0,8470	0,0360	0,1003	0,0034	0,4841	0,0612	0,0020	616	20	616	20	634	70	0
NI123-15	0,8290	0,0360	0,0965	0,0032	0,4752	0,0623	0,0020	609	20	595	19	642	69	2
NI123-16	0,8210	0,0310	0,0969	0,0032	0,4651	0,0614	0,0018	609	17	596	19	627	60	2
NI123-18	0,8920	0,0320	0,1024	0,0033	0,6168	0,0632	0,0015	645	17	628	19	744	48	3
NI123-19	0,8730	0,0310	0,1046	0,0033	0,6390	0,0605	0,0014	636	17	641	19	629	47	−1
NI123-20	0,8860	0,0340	0,0948	0,0031	0,4343	0,0678	0,0018	642	18	584	18	900	53	10
NI123-21	0,8520	0,0340	0,1017	0,0033	0,3992	0,0608	0,0019	623	18	624	19	632	64	0
NI123-22	0,9380	0,0330	0,1047	0,0034	0,6679	0,0650	0,0014	671	17	642	20	796	46	5
NI123-23	0,8250	0,0340	0,1012	0,0033	0,4639	0,0591	0,0017	607	18	621	19	553	60	−2
NI123-24	0,8250	0,0300	0,0984	0,0033	0,6368	0,0608	0,0015	611	17	605	19	632	52	1
NI123-25	0,8210	0,0310	0,0992	0,0032	0,5463	0,0600	0,0016	607	17	609	19	625	57	0
NI123-26	0,8730	0,0350	0,1022	0,0033	0,4957	0,0620	0,0018	630	19	626	19	645	62	1
NI123-27	0,8160	0,0370	0,0980	0,0032	0,4787	0,0604	0,0022	600	20	602	19	603	73	0
NI123-28	0,8150	0,0350	0,1007	0,0034	0,4735	0,0587	0,0020	604	20	618	20	539	72	−2
NI123-29	0,8340	0,0300	0,0968	0,0031	0,5549	0,0625	0,0016	615	17	595	18	673	53	3
NI123-31	0,8280	0,0310	0,0988	0,0032	0,6080	0,0608	0,0016	608	17	607	19	604	54	0
NI123-35	0,8420	0,0370	0,1008	0,0034	0,4614	0,0606	0,0021	613	20	618	20	587	72	−1
NI123-36	0,8370	0,0310	0,0982	0,0033	0,5862	0,0618	0,0015	614	17	604	19	617	53	2
NI123-37	0,8590	0,0330	0,1011	0,0033	0,4242	0,0616	0,0018	630	18	620	19	630	62	2
NI123-38	0,8760	0,0400	0,1009	0,0033	0,1966	0,0630	0,0023	627	21	620	20	596	72	1
NI123-39	0,8650	0,0460	0,0998	0,0035	0,1439	0,0629	0,0027	615	22	612	20	589	77	0
NI123-41	0,8420	0,0320	0,0993	0,0032	0,5408	0,0615	0,0015	622	18	611	19	618	55	2
NI123-42	0,8840	0,0370	0,1061	0,0036	0,5103	0,0604	0,0019	638	20	650	21	599	65	−2
NI123-43	0,8650	0,0360	0,1018	0,0033	0,5002	0,0616	0,0019	635	19	624	19	608	66	2
NI123-44	0,8630	0,0350	0,1046	0,0034	0,5997	0,0598	0,0015	630	19	641	20	567	56	−2
NI123-45	0,8550	0,0340	0,1008	0,0033	0,4438	0,0615	0,0018	622	19	618	19	623	61	1
NI123-46	0,7400	0,0280	0,0921	0,0031	0,5978	0,0583	0,0016	559	16	568	18	521	59	−2
NI123-47	0,8860	0,0320	0,1045	0,0033	0,5747	0,0615	0,0014	645	17	640	19	616	49	1
NI123-48	0,8300	0,0340	0,0991	0,0032	0,4667	0,0607	0,0017	613	18	609	19	598	59	1
NI123-49	0,8710	0,0320	0,1039	0,0033	0,6202	0,0608	0,0015	636	17	637	19	613	52	0
NI123-50	0,8330	0,0320	0,1000	0,0032	0,5794	0,0604	0,0016	614	17	614	19	604	55	0
NI123-51	0,8450	0,0320	0,1023	0,0034	0,5721	0,0599	0,0016	625	18	627	20	589	56	0
NI123-52	0,8480	0,0320	0,0991	0,0032	0,6135	0,0621	0,0015	621	17	609	19	623	54	2
NI123-53	0,9520	0,0430	0,1009	0,0033	0,3310	0,0684	0,0024	678	22	619	19	817	71	10
NI123-54	0,8250	0,0330	0,1000	0,0032	0,3616	0,0598	0,0019	609	18	614	19	590	63	−1
NI123-55	0,8790	0,0400	0,1028	0,0034	0,0235	0,0620	0,0022	626	20	630	20	599	65	−1
NI123-56	0,8500	0,0310	0,1002	0,0032	0,4842	0,0615	0,0016	622	17	615	19	623	56	1
NI123-57	0,8620	0,0350	0,1036	0,0035	0,1698	0,0603	0,0018	625	19	633	20	618	62	−1
NI123-58	0,8600	0,0300	0,1028	0,0033	0,7282	0,0607	0,0013	629	16	630	19	629	47	0
NI123-59	0,7920	0,0290	0,0950	0,0031	0,5692	0,0605	0,0015	590	16	585	18	600	54	1
NI123-60	0,8620	0,0340	0,0990	0,0033	0,5033	0,0631	0,0018	630	18	608	19	678	61	4
NI123-61	0,8640	0,0300	0,1015	0,0033	0,5287	0,0617	0,0015	632	17	622	19	624	53	2
NI123-62	0,8200	0,0330	0,0980	0,0033	0,5090	0,0607	0,0017	608	18	602	19	632	60	1
NI123-63	0,8670	0,0320	0,1038	0,0033	0,6355	0,0606	0,0014	632	17	636	19	598	50	−1
NI123-64	0,8640	0,0320	0,1019	0,0033	0,6581	0,0615	0,0014	630	17	625	19	637	50	1
NI123-65	0,8820	0,0330	0,1036	0,0034	0,6165	0,0617	0,0014	638	18	635	20	629	50	0
NI123-66	0,8750	0,0340	0,1045	0,0035	0,1714	0,0607	0,0016	637	18	640	20	630	54	0
NI123-67	0,9460	0,0370	0,1107	0,0036	0,6016	0,0620	0,0016	673	19	676	21	634	55	0
NI123-69	0,8400	0,0310	0,1020	0,0034	0,2915	0,0597	0,0015	619	17	625	20	608	53	−1
NI123-70	0,8920	0,0340	0,1030	0,0033	0,5248	0,0628	0,0016	647	18	631	19	651	55	3
NI123-71	0,8740	0,0330	0,1029	0,0033	0,5416	0,0616	0,0016	636	18	632	19	628	56	1
NI123-73	0,8770	0,0340	0,1042	0,0033	0,5507	0,0610	0,0015	636	18	640	19	615	53	−1
NI123-74	0,9200	0,0340	0,1004	0,0033	0,5518	0,0665	0,0016	663	18	616	19	795	51	8
NI123-75	0,8640	0,0350	0,1031	0,0033	0,4719	0,0608	0,0017	629	19	633	20	578	58	−1
NI123-76	0,8840	0,0320	0,1043	0,0034	0,3177	0,0615	0,0015	643	17	639	20	632	54	1
NI123-77	0,6760	0,0270	0,0857	0,0028	0,4950	0,0572	0,0016	524	16	529	17	476	57	−1
NI123-78	0,8810	0,0330	0,1041	0,0034	0,5859	0,0614	0,0015	639	17	639	20	637	53	0
NI123-79	0,8960	0,0350	0,1053	0,0034	0,5037	0,0617	0,0017	648	18	645	20	625	57	0
NI123-80	0,8560	0,0340	0,0992	0,0032	0,5006	0,0626	0,0017	623	18	609	19	635	60	2
NI123-81	0,8400	0,0310	0,0997	0,0032	0,5341	0,0611	0,0015	617	17	612	19	596	52	1
NI123-82	0,8640	0,0340	0,1030	0,0033	0,5023	0,0608	0,0017	633	18	632	19	590	61	0
NI123-83	0,8540	0,0330	0,1020	0,0033	0,4851	0,0607	0,0016	626	18	625	19	587	57	0
NI123-84	0,8860	0,0310	0,1030	0,0033	0,6576	0,0624	0,0014	645	17	631	19	638	49	2
NI123-85	0,8770	0,0350	0,1028	0,0034	0,4701	0,0619	0,0018	639	18	631	20	625	62	1
NI123-86	0,8600	0,0330	0,1012	0,0033	0,5492	0,0616	0,0016	627	18	621	20	621	56	1
NI123-87	0,8680	0,0320	0,1010	0,0033	0,5488	0,0623	0,0015	630	17	620	19	641	53	2
NI123-88	0,8530	0,0310	0,1006	0,0032	0,5821	0,0615	0,0015	625	17	617	19	644	51	1
NI123-89	0,8280	0,0370	0,1015	0,0035	0,2787	0,0592	0,0021	608	20	622	20	565	70	−2
NI123-90	0,8180	0,0310	0,0978	0,0032	0,5787	0,0607	0,0015	607	17	602	18	599	53	1
NI123-91	0,9220	0,0460	0,1041	0,0035	0,3210	0,0642	0,0027	656	24	639	21	664	83	3
NI123-93	0,8270	0,0330	0,1007	0,0033	0,4797	0,0596	0,0019	610	18	618	20	559	65	−1
NI123-94	2,8900	0,1000	0,2251	0,0072	0,7053	0,0931	0,0019	1375	26	1306	38	1477	38	5
NI123-95	0,8330	0,0310	0,0997	0,0032	0,5017	0,0606	0,0016	615	17	613	19	621	56	0
NI123-96	0,8110	0,0310	0,0985	0,0032	0,5118	0,0597	0,0017	603	18	606	19	571	61	0
NI123-97	0,7920	0,0330	0,0978	0,0032	0,5451	0,0587	0,0018	589	18	601	19	560	65	−2
NI123-98	0,8000	0,0410	0,0994	0,0034	0,3390	0,0584	0,0026	592	23	610	20	530	86	−3

Sample NI130 - Migmatitic gneiss (Coastal Terrane)														
	ISOTOPIC RATIOS							CALCULATED AGES (Ma)						
Analysis	$^{207}Pb/^{235}U$	± 2σ	$^{206}Pb/^{238}U$	±2σ	Rho	$^{207}Pb/^{206}Pb$	±2σ	$^{207}Pb/^{235}U$	±2σ	$^{206}Pb/^{238}U$	±2σ	$^{207}Pb/^{206}Pb$	±2σ	Discordance
NI130-01	0,8940	0,0300	0,1033	0,0028	0,5751	0,0628	0,0014	646	16	633	16	694	49	2
NI130-02	0,9100	0,0350	0,1087	0,0030	0,0342	0,0607	0,0018	644	17	664	18	629	58	0
NI130-03	0,9000	0,0320	0,1028	0,0029	0,5653	0,0635	0,0015	649	16	630	17	667	49	3
NI130-04	0,8900	0,0300	0,1048	0,0029	0,5869	0,0616	0,0014	648	16	642	17	609	45	1
NI130-05	0,8830	0,0300	0,1045	0,0029	0,3798	0,0613	0,0015	640	16	639	16	629	48	0
NI130-06	0,8910	0,0300	0,1062	0,0028	0,5894	0,0608	0,0014	646	16	651	16	623	45	−1
NI130-07	0,9070	0,0300	0,1033	0,0030	0,6047	0,0637	0,0013	652	16	633	18	639	59	3
NI130-08	0,8950	0,0280	0,1047	0,0029	0,4290	0,0620	0,0012	649	15	641	17	675	42	1
NI130-09	2,0200	0,2200	0,1540	0,0110	0,8143	0,0951	0,0040	944	48	890	56	1087	78	6
NI130-10	1,0580	0,0530	0,1144	0,0047	0,7879	0,0671	0,0018	709	22	690	25	620	52	3
NI130-11	0,9380	0,0320	0,1073	0,0029	0,5597	0,0634	0,0014	668	16	656	17	663	43	2
NI130-13	0,9090	0,0300	0,1078	0,0029	0,6228	0,0612	0,0013	652	16	661	17	622	46	−1
NI130-14	0,9550	0,0410	0,1087	0,0029	0,1069	0,0637	0,0020	661	16	664	17	627	53	0
NI130-15	0,9780	0,0480	0,1093	0,0039	0,7044	0,0649	0,0019	682	21	666	22	701	46	2
NI130-16	0,8880	0,0290	0,1073	0,0030	0,3063	0,0600	0,0013	644	16	656	17	632	73	2
NI130-17	1,3180	0,0950	0,1456	0,0081	0,7643	0,0657	0,0021	794	31	860	43	728	50	8
NI130-19	0,9100	0,0310	0,1105	0,0030	0,4749	0,0597	0,0013	657	17	675	18	671	58	−3
NI130-20	1,8900	0,0660	0,1763	0,0050	0,6848	0,0778	0,0017	1080	23	1046	27	756	58	3
NI130-23	0,8830	0,0290	0,1015	0,0028	0,5798	0,0631	0,0014	641	16	622	16	673	54	3
NI130-24	0,9130	0,0340	0,1060	0,0029	0,6035	0,0625	0,0015	655	18	649	17	630	58	1
NI130-25	0,8750	0,0300	0,1027	0,0030	0,7288	0,0618	0,0012	634	16	629	17	642	56	1
NI130-26	1,1900	0,1000	0,1196	0,0042	0,0884	0,0722	0,0029	708	25	725	24	530	54	−2
NI130-27	0,8970	0,0300	0,1070	0,0028	0,5308	0,0608	0,0014	647	16	656	17	578	46	−1
NI130-28	0,9600	0,0340	0,1063	0,0029	0,5587	0,0655	0,0015	677	17	651	17	652	49	4
NI130-29	0,8790	0,0300	0,1048	0,0028	0,6660	0,0608	0,0013	637	16	641	16	593	54	−1
NI130-30	0,8840	0,0300	0,1067	0,0028	0,5553	0,0601	0,0014	642	16	653	16	621	49	−2
NI130-31	0,8750	0,0330	0,1019	0,0034	0,6056	0,0623	0,0016	628	17	623	19	645	55	1
NI130-33	0,8760	0,0290	0,1024	0,0030	0,7614	0,0620	0,0013	638	16	628	18	642	53	2
NI130-34	0,8400	0,0290	0,0954	0,0029	0,5775	0,0639	0,0016	618	16	588	17	719	55	5
NI130-37	0,7870	0,0260	0,0929	0,0025	0,5711	0,0614	0,0014	587	15	573	15	662	58	2
NI130-38	0,8510	0,0310	0,0995	0,0026	0,4234	0,0620	0,0018	622	17	610	16	654	52	2
NI130-39	0,7930	0,0260	0,0960	0,0026	0,6243	0,0599	0,0013	593	14	591	15	623	54	0
NI130-40	0,8580	0,0300	0,1010	0,0027	0,4800	0,0616	0,0015	628	16	621	15	626	53	1
NI130-42	1,2200	0,1100	0,1087	0,0055	0,7075	0,0814	0,0027	705	28	659	31	924	67	7
NI130-43	0,8580	0,0290	0,1003	0,0028	0,5382	0,0620	0,0015	627	16	616	16	606	51	2
NI130-44	0,7260	0,0280	0,0874	0,0027	0,6244	0,0602	0,0017	550	17	539	16	677	49	2
NI130-45	0,8430	0,0300	0,1023	0,0026	0,4302	0,0598	0,0016	621	16	628	15	588	65	−1
NI130-46	0,8940	0,0770	0,0924	0,0038	0,1272	0,0702	0,0114	563	32	576	20	589	44	−2
NI130-47	0,8270	0,0280	0,0983	0,0026	0,5470	0,0610	0,0015	611	16	605	15	624	55	1
NI130-48	0,9190	0,0350	0,1013	0,0027	0,2363	0,0658	0,0022	653	18	623	16	775	53	5
NI130-50	0,7810	0,0290	0,0892	0,0029	0,5845	0,0635	0,0017	583	17	550	17	710	55	6
NI130-51	0,8790	0,0340	0,1056	0,0028	0,3602	0,0604	0,0019	636	18	647	17	700	140	−2
NI130-52	0,8370	0,0300	0,0997	0,0027	0,4847	0,0609	0,0016	615	17	612	16	638	51	0
NI130-53	0,8900	0,0340	0,1043	0,0027	0,2106	0,0619	0,0017	634	17	639	16	602	49	−1
NI130-54	0,8400	0,0300	0,1036	0,0027	0,4993	0,0588	0,0015	618	16	636	16	627	63	−3
NI130-55	0,8190	0,0300	0,1004	0,0027	0,4424	0,0592	0,0016	605	17	617	16	596	51	−2
NI130-56	0,9450	0,0410	0,1125	0,0032	0,3279	0,0609	0,0021	665	18	686	19	921	70	−3
NI130-57	0,8190	0,0280	0,0962	0,0026	0,5216	0,0617	0,0015	603	16	591	15	690	43	2
NI130-59	0,8690	0,0310	0,1034	0,0027	0,3778	0,0610	0,0017	637	17	635	16	639	48	0
NI130-61	0,8640	0,0290	0,1043	0,0027	0,4077	0,0601	0,0014	627	15	639	16	551	55	−2
NI130-62	0,8620	0,0300	0,1003	0,0027	0,4424	0,0623	0,0016	630	16	616	16	672	59	2
NI130-63	0,8960	0,0280	0,1082	0,0028	0,5525	0,0601	0,0012	646	15	664	16	779	60	−3
NI130-65	0,8530	0,0310	0,1037	0,0028	0,3831	0,0597	0,0016	620	16	635	16	565	55	−2
NI130-66	0,8670	0,0310	0,1042	0,0028	0,5024	0,0603	0,0015	635	17	640	17	619	44	−1
NI130-67	0,8680	0,0280	0,1068	0,0029	0,4708	0,0589	0,0013	632	16	653	17	784	89	−3
NI130-68	0,8890	0,0300	0,1056	0,0028	0,3830	0,0611	0,0014	640	15	647	16	588	50	−1
NI130-69	0,9090	0,0330	0,1060	0,0028	0,4660	0,0622	0,0016	651	17	649	16	656	50	0
NI130-70	0,8600	0,0280	0,1031	0,0027	0,6475	0,0605	0,0012	628	15	632	16	629	46	−1
NI130-71	0,8850	0,0290	0,1066	0,0029	0,6130	0,0602	0,0013	642	16	653	17	613	48	−2
NI130-72	1,0510	0,0630	0,1247	0,0057	0,6991	0,0611	0,0017	706	23	749	31	744	64	−6
NI130-73	0,9100	0,0290	0,1079	0,0028	0,5785	0,0612	0,0013	657	16	662	16	608	50	−1
NI130-74	0,9110	0,0310	0,1059	0,0028	0,5583	0,0624	0,0014	659	16	648	16	639	47	2
NI130-75	0,9270	0,0320	0,1086	0,0029	0,5936	0,0619	0,0014	665	17	664	17	603	44	0
NI130-76	0,8800	0,0290	0,1053	0,0028	0,5321	0,0606	0,0014	638	16	644	16	634	47	−1
NI130-77	0,8980	0,0310	0,1090	0,0028	0,4980	0,0598	0,0015	651	17	667	16	613	57	−2
NI130-78	0,8850	0,0320	0,1036	0,0027	0,5689	0,0620	0,0015	645	17	635	16	700	52	2
NI130-79	0,8860	0,0310	0,1056	0,0028	0,6225	0,0609	0,0015	642	16	647	16	587	57	−1
NI130-80	0,7070	0,0260	0,0802	0,0027	0,6549	0,0639	0,0015	539	15	496	16	780	51	9
NI130-81	0,8340	0,0300	0,0980	0,0028	0,4590	0,0617	0,0017	613	17	602	16	643	53	2
NI130-82	0,8950	0,0320	0,1049	0,0028	0,4960	0,0619	0,0016	644	17	643	16	606	52	0
NI130-83	0,8650	0,0310	0,1019	0,0028	0,5395	0,0616	0,0015	630	17	626	16	621	45	1
NI130-85	0,8680	0,0280	0,1032	0,0027	0,6073	0,0610	0,0013	633	15	632	16	640	50	0
NI130-86	0,9480	0,0300	0,1124	0,0029	0,6663	0,0612	0,0012	675	16	686	17	560	57	−2
NI130-87	0,8750	0,0290	0,1036	0,0028	0,6773	0,0613	0,0012	636	16	636	16	643	45	0
NI130-88	0,9080	0,0300	0,1077	0,0029	0,6273	0,0611	0,0013	653	16	659	17	643	42	−1
NI130-89	0,8780	0,0300	0,1039	0,0027	0,5899	0,0613	0,0013	636	16	637	16	622	51	0
NI130-90	0,8660	0,0290	0,1057	0,0027	0,5900	0,0594	0,0013	630	16	647	16	595	49	−3
NI130-91	0,7040	0,0240	0,0807	0,0021	0,6444	0,0633	0,0013	539	14	500	13	696	45	8
NI130-92	0,8990	0,0300	0,1054	0,0028	0,6186	0,0619	0,0013	648	16	647	16	612	48	0
NI130-93	0,9100	0,0310	0,1086	0,0028	0,6194	0,0608	0,0013	652	17	665	17	614	46	−2
NI130-95	0,8810	0,0290	0,1063	0,0028	0,5355	0,0601	0,0014	638	16	651	16	591	47	−2
NI130-96	0,9070	0,0310	0,1068	0,0029	0,4521	0,0616	0,0014	652	17	653	17	598	49	0
NI130-97	0,9120	0,0320	0,1065	0,0029	0,4387	0,0621	0,0017	654	17	652	17	659	43	0

Appendix B

Sample NK44 - Migmatitic gneiss (The Coastal Terrane)														
	ISOTOPIC RATIOS							CALCULATED AGES (Ma)						
Analysis	$^{207}Pb/^{235}U$	± 2σ	$^{206}Pb/^{238}U$	±2σ	Rho	$^{207}Pb/^{206}Pb$	±2σ	$^{207}Pb/^{235}U$	±2σ	$^{206}Pb/^{238}U$	±2σ	$^{207}Pb/^{206}Pb$	±2σ	Discordance
NK44-001	5,6700	0,1800	0,3444	0,0092	0,7529	0,1194	0,0021	1918	26	1904	44	1955	32	1
NK44-002	1,1050	0,0370	0,1208	0,0033	0,6114	0,0663	0,0015	756	18	736	19	860	46	3
NK44-003	5,3000	0,1800	0,3356	0,0097	0,7907	0,1145	0,0022	1859	30	1859	47	1891	33	0
NK44-004	16,0600	0,5000	0,5240	0,0140	0,7441	0,2223	0,0040	2874	30	2707	59	3016	29	6
NK44-005	1,1560	0,0440	0,1263	0,0034	0,0397	0,0664	0,0020	770	21	765	19	779	59	1
NK44-006	1,0530	0,0390	0,1086	0,0031	0,5574	0,0703	0,0019	726	19	664	18	939	57	9
NK44-007	1,0910	0,0390	0,1253	0,0036	0,2485	0,0631	0,0017	752	19	759	21	732	55	−1
NK44-008	3,3700	0,1100	0,2620	0,0072	0,7238	0,0933	0,0018	1494	24	1500	36	1500	36	0
NK44-009	2,5830	0,0850	0,2201	0,0059	0,6175	0,0851	0,0019	1287	24	1280	31	1339	43	1
NK44-010	1,1430	0,0410	0,1293	0,0036	0,5102	0,0641	0,0016	772	19	783	21	740	54	−1
NK44-100	4,5500	0,1600	0,2976	0,0090	0,8641	0,1109	0,0020	1734	30	1677	45	1811	33	3
NK44-101	2,9310	0,0980	0,2376	0,0067	0,7812	0,0895	0,0016	1381	25	1373	35	1380	36	1
NK44-104	1,2220	0,0460	0,1354	0,0037	0,5047	0,0655	0,0018	806	21	818	21	739	59	−1
NK44-105	1,2380	0,0420	0,1369	0,0038	0,6365	0,0656	0,0014	818	19	826	21	749	46	−1
NK44-106	1,2080	0,0420	0,1314	0,0036	0,5798	0,0667	0,0015	804	19	794	21	794	49	1
NK44-107	1,1580	0,0410	0,1237	0,0035	0,5496	0,0679	0,0017	780	20	752	20	829	55	4
NK44-108	2,3490	0,0960	0,2073	0,0068	0,8528	0,0822	0,0017	1217	29	1209	36	1213	42	1
NK44-011	1,1770	0,0450	0,1320	0,0037	0,5533	0,0647	0,0018	788	20	801	21	744	58	−2
NK44-012	1,1420	0,0440	0,1280	0,0036	0,5035	0,0647	0,0019	767	20	775	21	748	61	−1
NK44-014	1,1660	0,0400	0,1246	0,0034	0,4904	0,0679	0,0017	779	19	756	19	832	52	3
NK44-016	15,480	0,5100	0,5200	0,0150	0,7835	0,2159	0,0040	2842	32	2701	63	2949	30	5
NK44-017	1,1670	0,0420	0,1280	0,0035	0,4134	0,0661	0,0019	782	20	775	20	776	60	1
NK44-018	1,1490	0,0430	0,1263	0,0035	0,5423	0,0660	0,0018	775	20	765	20	786	55	1
NK44-019	1,1640	0,0410	0,1267	0,0034	0,5376	0,0666	0,0016	781	19	769	19	798	51	2
NK44-020	1,1690	0,0430	0,1285	0,0035	0,3998	0,0660	0,0019	782	21	778	20	801	60	1
NK44-021	1,0900	0,0400	0,1225	0,0033	0,4380	0,0645	0,0018	746	20	746	19	723	59	0
NK44-022	1,1000	0,0390	0,1218	0,0033	0,5278	0,0655	0,0016	753	19	742	19	759	53	1
NK44-023	2,3140	0,0740	0,2032	0,0056	0,6758	0,0826	0,0016	1214	23	1190	30	1254	40	2
NK44-024	1,1380	0,0430	0,1227	0,0033	0,5074	0,0673	0,0019	768	21	746	19	801	60	3
NK44-025	5,3400	0,1700	0,3275	0,0091	0,7510	0,1183	0,0021	1870	27	1826	44	1931	32	2
NK44-026	4,9900	0,1900	0,3130	0,0092	0,7552	0,1156	0,0026	1819	32	1757	45	1893	43	4
NK44-027	5,1200	0,1800	0,3131	0,0089	0,6227	0,1186	0,0028	1835	31	1756	44	1914	43	4
NK44-028	4,8200	0,1600	0,2997	0,0089	0,7246	0,1166	0,0024	1784	28	1688	44	1915	37	6
NK44-029	2,7740	0,0900	0,2207	0,0060	0,7340	0,0912	0,0018	1348	24	1284	31	1450	37	5
NK44-030	1,1100	0,0390	0,1246	0,0033	0,5716	0,0646	0,0016	758	19	756	19	743	52	0
NK44-031	1,0980	0,0440	0,1200	0,0032	0,4165	0,0664	0,0021	745	21	730	19	764	63	2
NK44-032	1,1090	0,0400	0,1206	0,0033	0,4929	0,0667	0,0018	755	19	734	19	801	57	3
NK44-033	1,1420	0,0440	0,1271	0,0035	0,4102	0,0652	0,0021	768	21	770	20	748	63	0
NK44-034	2,1190	0,0870	0,1906	0,0058	0,6817	0,0806	0,0021	1150	28	1125	31	1153	56	2
NK44-035	5,1500	0,1700	0,3137	0,0087	0,7000	0,1191	0,0025	1838	29	1753	43	1941	38	5
NK44-036	1,2760	0,0470	0,1337	0,0037	0,5402	0,0692	0,0019	830	21	808	21	883	56	3
NK44-038	5,9000	0,1900	0,3445	0,0094	0,6917	0,1242	0,0025	1956	28	1916	46	1994	36	2
NK44-040	2,2090	0,0750	0,1976	0,0054	0,6228	0,0811	0,0018	1178	24	1159	29	1210	44	2
NK44-042	1,1410	0,0460	0,1284	0,0037	0,5390	0,0644	0,0019	765	21	777	21	713	62	−2
NK44-043	1,1510	0,0470	0,1156	0,0034	0,6165	0,0722	0,0021	764	21	704	19	925	57	9
NK44-045	4,1800	0,1800	0,2724	0,0093	0,8567	0,1113	0,0023	1680	35	1561	47	1789	40	8
NK44-046	1,0930	0,0390	0,1244	0,0033	0,4881	0,0637	0,0017	750	19	755	19	710	55	−1
NK44-047	1,5540	0,0500	0,1460	0,0040	0,6983	0,0772	0,0015	954	20	878	22	1114	40	9
NK44-048	6,7500	0,2800	0,3660	0,0100	0,5225	0,1338	0,0042	2065	37	2003	48	2107	55	3
NK44-049	1,7310	0,0750	0,1675	0,0054	0,7818	0,0750	0,0019	1007	28	995	30	1044	51	1
NK44-050	2,2710	0,0970	0,2047	0,0058	0,4496	0,0805	0,0027	1202	30	1202	31	1145	68	0
NK44-051	5,0800	0,1700	0,3155	0,0087	0,6720	0,1168	0,0023	1824	28	1765	42	1896	37	3
NK44-052	1,1890	0,0470	0,1281	0,0037	0,5540	0,0673	0,0020	791	22	777	21	824	63	2
NK44-053	0,9490	0,0340	0,1013	0,0028	0,5811	0,0679	0,0016	674	18	623	16	835	52	8
NK44-054	1,1550	0,0410	0,1253	0,0035	0,6514	0,0669	0,0015	780	19	760	20	808	47	3
NK44-055	1,0950	0,0400	0,1216	0,0033	0,5481	0,0653	0,0017	746	19	739	19	750	56	1
NK44-057	5,9900	0,2000	0,3421	0,0095	0,6820	0,1270	0,0027	1973	29	1895	46	2073	37	4
NK44-058	14,250	0,4500	0,5030	0,0140	0,7551	0,2055	0,0038	2761	30	2625	59	2846	29	5
NK44-059	1,1010	0,0410	0,1228	0,0033	0,5896	0,0650	0,0017	752	19	745	19	738	54	1
NK44-060	6,4900	0,2200	0,3520	0,0100	0,7250	0,1337	0,0026	2040	30	1934	48	2121	35	5
NK44-061	5,1800	0,1700	0,3180	0,0086	0,6936	0,1181	0,0022	1849	28	1779	42	1902	35	4
NK44-062	3,7200	0,1400	0,2566	0,0077	0,7750	0,1051	0,0023	1576	30	1475	40	1700	40	7
NK44-063	0,9630	0,0370	0,1125	0,0032	0,4846	0,0621	0,0018	682	19	686	18	652	60	−1
NK44-064	1,1440	0,0390	0,1233	0,0035	0,6042	0,0673	0,0015	769	18	750	20	819	48	3
NK44-065	1,1410	0,0430	0,1213	0,0033	0,4565	0,0682	0,0020	770	21	738	19	826	61	4
NK44-066	1,1580	0,0460	0,1206	0,0035	0,5729	0,0696	0,0020	777	21	732	20	885	62	6
NK44-067	1,1630	0,0440	0,1261	0,0036	0,5851	0,0669	0,0017	777	20	764	20	800	55	2
NK44-068	1,1350	0,0400	0,1240	0,0035	0,6473	0,0664	0,0015	768	19	754	20	792	50	2
NK44-069	1,4100	0,0780	0,1346	0,0048	0,8461	0,0760	0,0025	879	32	814	27	1015	67	8
NK44-070	4,8100	0,1700	0,3136	0,0089	0,6317	0,1112	0,0027	1771	31	1757	44	1782	45	1
NK44-071	1,4550	0,0600	0,1408	0,0045	0,5585	0,0749	0,0023	908	24	849	25	1012	60	7
NK44-072	1,5350	0,0580	0,1577	0,0047	0,6135	0,0706	0,0019	951	24	944	26	939	55	1
NK44-073	1,1380	0,0470	0,1278	0,0035	0,3888	0,0646	0,0022	772	23	774	20	715	70	0
NK44-074	2,9300	0,0980	0,2337	0,0065	0,6147	0,0909	0,0020	1386	25	1353	34	1448	42	2
NK44-075	1,1140	0,0440	0,1269	0,0035	0,4538	0,0637	0,0019	762	21	770	20	707	63	−1
NK44-076	1,5900	0,1300	0,1312	0,0038	0,5838	0,0879	0,0048	864	30	793	22	1003	77	9
NK44-077	1,0950	0,0380	0,1163	0,0033	0,5970	0,0683	0,0017	751	19	708	19	877	53	6
NK44-078	1,1980	0,0430	0,1337	0,0037	0,5769	0,0650	0,0016	801	20	808	21	765	54	−1
NK44-079	1,1600	0,0430	0,1245	0,0035	0,5925	0,0676	0,0017	781	20	755	20	819	54	3
NK44-080	1,1460	0,0430	0,1281	0,0035	0,5396	0,0649	0,0018	775	21	778	20	757	58	0
NK44-081	1,1730	0,0460	0,1302	0,0035	0,5573	0,0653	0,0018	783	21	788	20	732	58	−1
NK44-082	1,1420	0,0660	0,1201	0,0045	0,4072	0,0690	0,0031	781	25	726	26	943	71	8
NK44-083	1,1770	0,0450	0,1287	0,0036	0,4603	0,0663	0,0019	784	21	779	20	727	59	1
NK44-084	3,2800	0,1100	0,2545	0,0067	0,5358	0,0935	0,0022	1477	27	1458	34	1486	44	1
NK44-085	4,4900	0,1500	0,2983	0,0082	0,7722	0,1092	0,0019	1723	27	1682	41	1771	33	2
NK44-086	7,1200	0,2500	0,3780	0,0110	0,6159	0,1366	0,0033	2117	32	2065	49	2145	43	3
NK44-087	1,0840	0,0370	0,1195	0,0033	0,6969	0,0658	0,0014	742	18	726	19	760	45	2
NK44-088	1,7970	0,0730	0,1724	0,0055	0,7256	0,0756	0,0019	1043	27	1024	30	1095	52	2
NK44-089	1,2070	0,0470	0,1307	0,0035	0,5463	0,0670	0,0019	799	22	791	20	765	59	1
NK44-092	1,1500	0,0420	0,1260	0,0036	0,5209	0,0662	0,0018	775	20	765	20	749	57	1
NK44-093	1,1600	0,0410	0,1282	0,0034	0,4524	0,0656	0,0018	784	20	779	20	763	58	1
NK44-094	1,2110	0,0410	0,1240	0,0034	0,6055	0,0708	0,0016	804	19	752	19	919	45	7
NK44-095	2,3640	0,0750	0,2080	0,0056	0,7724	0,0824	0,0014	1230	22	1215	30	1237	36	1
NK44-096	1,1840	0,0410	0,1304	0,0035	0,5170	0,0659	0,0016	793	19	789	20	797	52	1
NK44-097	1,2040	0,0410	0,1301	0,0034	0,4875	0,0671	0,0017	798	19	789	19	805	53	1
NK44-098	4,7100	0,1500	0,3086	0,0086	0,7536	0,1107	0,0020	1764	27	1729	43	1794	33	2
NK44-110	1,0620	0,0410	0,1207	0,0035	0,6688	0,0638	0,0016	736	20	734	20	704	52	0
NK44-111	1,2040	0,0470	0,1314	0,0036	0,5196	0,0665	0,0019	795	22	794	21	745	61	0
NK44-112	1,2120	0,0420	0,1272	0,0034	0,6619	0,0691	0,0015	802	19	771	20	865	46	4

Sample NJ116 - Quartzite (Coastal Terrane)														
	ISOTOPIC RATIOS							CALCULATED AGES (Ma)						
Analysis	$^{207}Pb/^{235}U$	± 2σ	$^{206}Pb/^{238}U$	±2σ	Rho	$^{207}Pb/^{206}Pb$	±2σ	$^{207}Pb/^{235}U$	±2σ	$^{206}Pb/^{238}U$	±2σ	$^{207}Pb/^{206}Pb$	±2σ	Discordance
NJ116-01-01	5,3000	0,1600	0,3207	0,0069	0,7317	0,1192	0,0024	1014	20	1025	21	1007	45	4
NJ116-01-02	2,1490	0,0680	0,1986	0,0045	0,6260	0,0785	0,0017	1331	24	1328	26	1341	49	−1
NJ116-01-03	12,960	0,3800	0,4710	0,0100	0,4912	0,2008	0,0040	990	21	975	22	1002	45	8
NJ116-01-04	2,7320	0,0900	0,2294	0,0051	0,6969	0,0870	0,0022	1722	24	1687	31	1768	39	0
NJ116-01-05	2,9500	0,1100	0,2197	0,0062	0,7245	0,0977	0,0020	1906	29	1852	40	1975	39	8
NJ116-01-06	8,5500	0,2500	0,3846	0,0082	0,6759	0,1617	0,0031	1842	26	1770	36	1931	41	9
NJ116-01-07	1,5380	0,0460	0,1568	0,0034	0,5194	0,0713	0,0015	1247	28	1193	27	1328	66	0
NJ116-01-08	2,4530	0,0720	0,2079	0,0042	0,7206	0,0863	0,0017	1906	27	1823	36	2016	39	3
NJ116-01-09	5,2500	0,1500	0,3376	0,0071	0,6781	0,1126	0,0023	1729	26	1650	35	1835	38	−1
NJ116-01-10	1,6030	0,0500	0,1593	0,0035	0,7062	0,0731	0,0016	1157	22	1167	24	1160	44	1
NJ116-01-11	6,1300	0,1800	0,3348	0,0073	0,7196	0,1335	0,0026	1858	25	1869	34	1847	37	7
NJ116-01-12	5,2700	0,2000	0,3181	0,0085	0,8208	0,1206	0,0032	859	26	817	25	965	55	5
NJ116-01-13	5,6900	0,2000	0,3467	0,0082	0,4867	0,1199	0,0035	991	23	995	23	995	56	0
NJ116-01-14	2,6640	0,0830	0,2261	0,0054	0,6532	0,0845	0,0018	1843	29	1742	38	1956	42	0
NJ116-01-15	5,5700	0,1700	0,3268	0,0073	0,6556	0,1250	0,0027	1949	28	1952	37	1945	42	5
NJ116-01-16	4,9600	0,1600	0,3003	0,0072	0,5776	0,1220	0,0025	1568	30	1478	30	1665	51	7
NJ116-01-17	4,5100	0,1400	0,2908	0,0070	0,5598	0,1126	0,0024	1712	28	1612	35	1809	51	5
NJ116-01-18	5,0100	0,1700	0,3249	0,0079	0,5046	0,1129	0,0030	1916	31	1918	40	1934	54	0
NJ116-01-19	3,9800	0,1700	0,2702	0,0084	0,6497	0,1059	0,0024	1237	22	1163	24	1348	45	5
NJ116-01-20	3,5800	0,1400	0,2617	0,0064	0,6822	0,0993	0,0029	1319	23	1316	28	1306	41	2
NJ116-01-21	1,6700	0,0570	0,1632	0,0039	0,5210	0,0736	0,0017	1161	24	1087	23	1297	56	2
NJ116-01-22	5,8200	0,1900	0,3546	0,0079	0,5891	0,1200	0,0029	1815	30	1810	39	1844	49	0
NJ116-01-23	3,9100	0,1200	0,2582	0,0059	0,7417	0,1101	0,0023	942	18	939	19	961	42	9
NJ116-01-24	4,7100	0,1600	0,3052	0,0067	0,6199	0,1124	0,0028	1719	29	1706	37	1749	45	2
NJ116-01-25	5,1800	0,1500	0,3203	0,0066	0,5541	0,1170	0,0026	932	21	923	20	914	58	3
NJ116-01-26	5,1800	0,1600	0,3175	0,0073	0,7214	0,1187	0,0027	967	20	955	20	1010	44	4
NJ116-01-27	1,5070	0,0540	0,1508	0,0038	0,6070	0,0718	0,0019	1751	28	1629	35	1923	43	3
NJ116-01-28	1,4690	0,0510	0,1467	0,0033	0,5809	0,0726	0,0021	1847	28	1822	39	1883	41	4
NJ116-01-29	3,6900	0,1200	0,2559	0,0059	0,6278	0,1054	0,0026	1201	23	1184	26	1226	44	7
NJ116-01-31	4,9800	0,1600	0,3167	0,0071	0,4234	0,1148	0,0027	935	31	920	22	874	90	2
NJ116-01-32	6,8500	0,2200	0,3541	0,0086	0,5946	0,1395	0,0028	1121	23	1102	24	1161	46	7
NJ116-01-33	5,2600	0,1900	0,3111	0,0076	0,7495	0,1215	0,0029	2674	28	2486	44	2831	33	6
NJ116-01-34	2,2040	0,0810	0,1951	0,0045	0,6287	0,0812	0,0024	1414	27	1390	31	1445	48	2
NJ116-01-35	1,6020	0,0610	0,1462	0,0036	0,5521	0,0781	0,0022	1967	30	1932	42	2007	46	8
NJ116-01-36	6,0000	0,1900	0,3459	0,0073	0,6137	0,1257	0,0033	1731	29	1699	38	1796	47	3
NJ116-01-37	13,570	0,4200	0,4830	0,0110	0,6928	0,2056	0,0046	1920	29	1884	39	1959	39	8
NJ116-01-38	2,4350	0,0970	0,2035	0,0051	0,5332	0,0859	0,0029	1171	25	1148	24	1217	59	5
NJ116-01-39	4,6400	0,2100	0,3015	0,0074	0,6919	0,1121	0,0048	1919	28	1881	39	1969	37	2
NJ116-01-40	1,7180	0,0590	0,1611	0,0039	0,7589	0,0771	0,0019	1607	24	1479	30	1797	38	5
NJ116-01-41	4,4100	0,1500	0,2841	0,0072	0,8026	0,1121	0,0023	2281	26	2097	39	2476	32	6
NJ116-01-42	1,5140	0,0520	0,1544	0,0035	0,3431	0,0706	0,0020	1735	36	1697	37	1779	76	1
NJ116-01-43	4,9700	0,1700	0,3129	0,0074	0,7065	0,1140	0,0032	1950	28	1905	40	1974	38	3
NJ116-01-44	2,0670	0,0700	0,1776	0,0042	0,6782	0,0830	0,0021	1761	28	1720	33	1827	45	7
NJ116-01-45	4,3900	0,1500	0,2856	0,0071	0,6319	0,1121	0,0031	1537	31	1501	32	1590	56	6
NJ116-01-46	4,5600	0,1500	0,2852	0,0068	0,6367	0,1157	0,0029	1813	26	1770	34	1864	43	8
NJ116-01-47	3,6900	0,1300	0,2581	0,0059	0,6006	0,1036	0,0029	929	22	906	21	970	52	6
NJ116-01-48	2,1590	0,0740	0,1842	0,0043	0,7471	0,0848	0,0024	1250	21	1216	22	1337	39	7
NJ116-01-50	5,0900	0,1600	0,3017	0,0069	0,5554	0,1217	0,0028	1972	28	1916	34	2032	46	8
NJ116-01-51	2,3920	0,0760	0,1979	0,0046	0,5164	0,0871	0,0020	1843	25	1789	32	1903	40	6
NJ116-01-52	1,5230	0,0740	0,1535	0,0040	0,6338	0,0716	0,0031	851	19	826	19	901	45	2
NJ116-01-53	14,510	0,5000	0,4810	0,0110	0,5704	0,2161	0,0062	1809	30	1753	36	1845	53	10
NJ116-01-54	4,4500	0,1300	0,2983	0,0063	0,5519	0,1077	0,0023	914	21	881	18	977	59	2
NJ116-01-56	1,7220	0,0530	0,1728	0,0039	0,7201	0,0734	0,0016	1864	25	1793	33	1942	37	−1
NJ116-02-01	4,4500	0,1500	0,3032	0,0075	0,4758	0,1072	0,0026	1852	32	1766	41	1963	50	1
NJ116-02-02	5,6600	0,1800	0,3384	0,0081	0,2437	0,1214	0,0026	1232	36	1157	28	1332	93	2
NJ116-02-03	1,3120	0,0430	0,1368	0,0033	0,6893	0,0695	0,0016	2726	29	2535	49	2868	38	3
NJ116-02-04	5,6400	0,1900	0,3407	0,0083	0,3520	0,1206	0,0026	951	22	877	20	1106	53	2
NJ116-02-05	2,0180	0,0660	0,1867	0,0044	0,6768	0,0786	0,0018	1775	28	1621	34	1945	40	2
NJ116-02-07	4,5900	0,1500	0,2843	0,0068	0,7185	0,1173	0,0024	1591	26	1449	32	1777	38	8
NJ116-02-08	4,7500	0,1600	0,2865	0,0068	0,4959	0,1197	0,0027	2779	33	2528	48	2940	45	10
NJ116-02-09	4,6600	0,1600	0,2875	0,0069	0,8153	0,1179	0,0028	1658	31	1508	36	1866	41	7
NJ116-02-10	5,1900	0,1700	0,3279	0,0081	0,6342	0,1152	0,0025	1012	22	965	22	1121	50	1
NJ116-02-11	2,3800	0,1200	0,1964	0,0052	0,8707	0,0880	0,0041	1616	35	1538	43	1727	43	6
NJ116-02-13	10,550	0,3600	0,4340	0,0110	0,5470	0,1763	0,0036	1828	32	1734	37	1942	50	7
NJ116-02-15	3,0300	0,1100	0,2412	0,0060	0,7617	0,0913	0,0022	1705	28	1610	36	1838	37	2
NJ116-02-20	4,1700	0,1600	0,2631	0,0071	0,6686	0,1141	0,0026	1566	26	1470	30	1716	45	10
NJ116-02-22	2,2750	0,0730	0,2013	0,0048	0,7903	0,0818	0,0018	2084	28	1951	40	2215	35	1
NJ116-02-23	1,3480	0,0600	0,1355	0,0044	0,7148	0,0715	0,0019	1810	26	1693	35	1975	37	5
NJ116-02-24	3,8000	0,1200	0,2519	0,0062	0,7816	0,1088	0,0023	1990	26	1858	35	2146	34	10
NJ116-02-26	5,9400	0,2100	0,3490	0,0087	0,7866	0,1237	0,0032	2483	31	2316	50	2614	33	2
NJ116-02-29	4,5300	0,1600	0,3018	0,0077	0,6260	0,1103	0,0027	1133	23	1054	23	1258	49	2
NJ116-02-31	1,6640	0,0600	0,1670	0,0041	0,6280	0,0727	0,0020	1738	27	1616	34	1890	45	0
NJ116-02-36	5,8500	0,1900	0,3451	0,0084	0,7146	0,1217	0,0025	1826	27	1693	34	1988	41	2
NJ116-02-37	5,5900	0,1900	0,3331	0,0083	0,7275	0,1215	0,0026	1746	27	1613	34	1907	37	3
NJ116-02-39	5,1200	0,1900	0,3091	0,0075	0,8907	0,1194	0,0033	1383	29	1277	32	1571	38	5